Contribution to characterization of last-generation photodetectors and improvement of their efficiency using micro and nanostructures.

by

Eduardo López Fraguas

A dissertation submitted by in partial fulfillment of the requirements for the degree of Doctor of Philosophy in

Electrical Engineering, Electronics and Automation

Universidad Carlos III de Madrid

Advisor(s):
Ricardo Vergaz Benito
José Manuel Sánchez Pena

Tutor:
Ricardo Vergaz Benito

June 2021

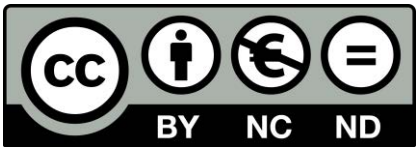

To my friends and family,
that supported me and gave me the courage
to take this path.

To my advisors,
Ricardo & Jose Manuel,
for share your expertise in everything,
from lab work to dealing with bureaucracy.

To every person that collaborated
in one way or another to this work,
giving me guidance and wisdom,
from Italy to Germany,
passing through Mexico and Spain.

To my soulmate,
who has accompanied me laughing, crying,
and both at the same time.

To every student
interested in research around this world,
you can make incredible things.

To the ones that are not here,
but hopefully are looking
from the sky and stars.

To you.
And, why not, to me.

"Why do you want to know why…?" – René Lavand.

ACKNOWLEDGEMENTS

The present work has been funded from the following projects:

- Comunidad de Madrid through SINFOTON-CM Research Program (S2013/MIT-2790) and SINFOTON2-CM (S2018/NMT-4326)
- Ministerio de Economia, Agencia Estatal de Investigación and European Union's FEDER through TEC2016-77242-C3-(1-R, 2-R and 3-R) AEI/FEDER, UE Projects.
- European Research Council (ERC) via Consolidator Grant (724424-No-LIMIT)
- Generalitat Valenciana via Prometeo Grant Q-Devices (Prometeo/2018/098)
- European Commission via FET Open grant (862656 – DROP-IT)

Also, this project could not be possible with the financial support of the Ministerio de Educación y Formación Profesional through the following grants that I have received:

- Doctoral Grant FPU research fellowship (FPU17/00612).
- Research Stay Grant (EST18/00399) supporting my research stay at Jaume I University (Castellón, Spain)
- Research Stay Grant (EST19/00073) supporting my research stay at Helmholtz Zentrum Berlin and Zuse Institute Berlin (Berlin, Germany).

PUBLISHED AND SUBMITTED CONTENT

The publications generated during the duration of this thesis are listed below. All of them have been published in international journals belonging to Q1 or Q2 on their own sector according to the JCR Index, and all of them have been mentioned and/or partially included in the contents of this document.

1. B. Arredondo, G. del Pozo, E. Hernández-Balaguera, D. Martín-Martín, M.C. López González, B. Romero, **E. López-Fraguas**, R. Vergaz, X. Quintana, J. Lamminaho, E. Destouesse, M. Ahmadpour, V. Turkovic, M. Madsen, "Identification of Degradation Mechanisms in Slot-Die-Coated Nonfullerene ITO-Free Organic Solar Cells Using Different Illumination Spectra," *ACS Appl. Energy Mater.*, vol. 3, no. 7, pp. 6476–6485, Jul. 2020, doi: 10.1021/acsaem.0c00711.
   - Q2: 85 out of 314 in Material Science, Multidisciplinary topic.
   - Partly included in the thesis, mentioned in Chapter 3. Whenever material from this source is included in this thesis, it is singled out with typographic means and an explicit reference.
2. M.H. Elshorbagy, **E. López-Fraguas**, J. M. Sánchez-Pena, B. García-Cámara, and R. Vergaz, "Boosting ultrathin aSi-H solar cells absorption through a nanoparticle cross-packed metasurface," *Solar Energy*, vol. 202, pp. 10–16, May 2020, doi: 10.1016/j.solener.2020.03.075.
   - Q2: 35 out of 112 in Energy & Fuels topic.
   - Partly included in the thesis, mentioned in Chapter 4. Whenever material from this source is included in this thesis, it is singled out with typographic means and an explicit reference.
3. M.H. Elshorbagy, **E. López-Fraguas**, F. A. Chaudhry, J. M. Sánchez-Pena, R. Vergaz, and B. García-Cámara, "A monolithic nanostructured-perovskite/silicon tandem solar cell: feasibility of light management through geometry and materials selection," *Scientific Reports*, vol. 10, no. 1, Art. no. 1, Feb. 2020, doi: 10.1038/s41598-020-58978-5.
   - Q1: 17 out of 71 in Multidisciplinary Sciences.
   - Partly included in the thesis, mentioned in Chapter 4. Whenever material from this source is included in this thesis, it is singled out with typographic means and an explicit reference.
4. **E. López-Fraguas**, S. Masi, and I. Mora-Seró, "Optical Characterization of Lead-Free Cs2SnI6 Double Perovskite Fabricated from Degraded and Reconstructed CsSnI3 Films," *ACS Appl. Energy Mater.*, vol. 2, no. 12, pp. 8381–8387, Dec. 2019, doi: 10.1021/acsaem.9b01827.
   - Q2: 85 out of 314 in Material Science, Multidisciplinary topic.
   - Partly included in the thesis, mentioned in Chapter 2. Whenever material from this source is included in this thesis, it is singled out with typographic means and an explicit reference.
5. **E. López-Fraguas**, B. Arredondo, C. Vega-Colado, G- del Pozo, M. Najafi, D. Martín-Martín, Y. Galagan, J.M. Sánchez-Pena, R. Vergaz, B. Romero, "Visible Light Communication system using an organic emitter and a perovskite photodetector," *Organic Electronics*, vol. 73, pp. 292–298, Oct. 2019, doi: 10.1016/j.orgel.2019.06.028.
   - Q2: 41 out of 155 in Applied Physics topic.

- Partly included in the thesis, mentioned in Chapter 2. Whenever material from this source is included in this thesis, it is singled out with typographic means and an explicit reference.

6. M.H. Elshorbagy, B. García-Cámara, **E. López-Fraguas**, R. Vergaz, "Efficient Light Management in a Monolithic Tandem Perovskite/Silicon Solar Cell by Using a Hybrid Metasurface," *Nanomaterials*, vol. 9, no. 5, Art. no. 5, May 2019, doi: 10.3390/nano9050791.
   - Q2: 89 out of 314 in Material Science, Multidisciplinary topic.
   - Partly included in the thesis, mentioned in Chapter 4. Whenever material from this source is included in this thesis, it is singled out with typographic means and an explicit reference.
7. **E. López-Fraguas**, J.M. Sánchez-Pena, R. Vergaz, "A Low-Cost LED-Based Solar Simulator," *IEEE Transactions on Instrumentation and Measurement*, vol. 68, no. 12, pp. 4913–4923, Dec. 2019, doi: 10.1109/TIM.2019.2899513.
   - Q1: 9 out of 64 in Instruments & Instrumentation topic.
   - Partly included in the thesis, mentioned in Chapter 3. Whenever material from this source is included in this thesis, it is singled out with typographic means and an explicit reference.
8. C. Vega-Colado, B. Arredondo, J.C. Torres, **E. López-Fraguas**, R. Vergaz, D. Martín-Martín, G. del Pozo, B. Romero, P. Apilo, X. Quintana, M.A. Geday, C. de Dios, J.M. Sánchez-Pena, "An All-Organic Flexible Visible Light Communication System," *Sensors*, vol. 18, no. 9, Art. no. 9, Sep. 2018, doi: 10.3390/s18093045.
   - Q1: 15 out of 61 in Instrument & Instrumentation topic.
   - Partly included in the thesis, mentioned in Chapters 2 and 3. Whenever material from this source is included in this thesis, it is singled out with typographic means and an explicit reference.

OTHER RESEARCH MERITS

CONGRESS CONTRIBUTIONS:

The following contributions belong to communications to national and international congress, in poster format or oral communications.

1. **E. López-Fraguas**, J.M. Sánchez-Pena, R.Vergaz, "A Low-Cost LED-Based Solar Simulator" IEEE International Instrumentation and Measurement Technology Conference I2MTC (2021). International, poster/oral communication (online).
2. B. García-Cámara, **E. López-Fraguas**, R. Vergaz, M.H. Elshorbagy, J.M. Sánchez-Pena, "Improving the optical response of solar cell using dielectric metastructures" 9th International Conference on Photonics, Optics and Laser Technology, Photoptics (2021). International, co-author (online)
3. **E. López-Fraguas**, J.M. Sánchez-Pena, R. Vergaz, "Concentrando diversos métodos de caracterización en un mismo dispositivo: SUNBOX" Winter meeting SINFOTON2 (2021). National, poster format (online).
4. S. Masi, **E. López-Fraguas**, I. Mora-Seró, "Optical Characterization of Lead-Free Cs2SnI6 Double Perovskite Fabricated from Degraded and Reconstructed CsSnI3 Films," Beyond lead halide perovskites: syntheses and applications of metal halide semiconductors (2020). International, poster format (online)
5. **E. López-Fraguas**, B. García-Cámara, R. Vergaz, "Diffraction nano-grating as absorption improver in perovskite solar cell," Autumn meeting SINFOTON2 (2019). National, poster format (Alcalá de Henares, Madrid, Spain)
6. F. A. Chaudhry, R. Vergaz, **E. López-Fraguas**, B. García-Cámara, "Optical enhancement in solar cells using nanoparticles," Autumn meeting SINFOTON2 (2019). National, poster format (Alcalá de Henares, Madrid, Spain)
7. **E. López-Fraguas**, B. García-Cámara, R. Vergaz, "Total internal reflection using nano-gratings for enhancing the optical response of perovskite soar cells," 10th International Conference on Metamaterials, Photonic Crystals and Plasmonics META2019 (2019). International, oral communication (Lisbon, Portugal)
8. **E. López-Fraguas**, J.M. Sánchez-Pena, R. Vergaz, "Characterizing photo-devices with SUNBOX: A Low-Cost AAA Class Solar Simulator" 11th Optoelectronic Spanish Meeting OPTOEL'19 (2019). National, poster format (Zaragoza, Aragón, Spain)
9. **E. López-Fraguas**, "Can perovskites go comercial? My research on tin-halide perovskites" Research Network: Perovskites for solar energy conversion and optoelectronics (2019). National, oral communication (Castellón, Comunidad Valenciana, Spain)
10. B. García-Cámara, R. Vergaz, J.F. Algorri, **E. López-Fraguas**, M.H. Elshorbagy, A. Cuadrado, J.M. Sánchez-Pena, "The Quest of Directional Light Scattering" 40th PIERS (2018). International, co-author (Toyama, Japan)
11. **E. López-Fraguas**, "Pi-research: Tu investigación en 3 minutos y 14 segundos" III RNOJ (2018). National, oral communication (Castellón, Comunidad Valenciana, Spain)
12. **E. López-Fraguas**, R. Vergaz, "SUNBOX: Irradiador Solar Sintonizable y de Bajo Coste para la Caracterización de Dispositivos Fotónicos" XII National Optics Meeting RNO2018 (2018). National, oral communication (Castellón, Comunidad Valenciana, Spain)

KNOWLEDGE TRANSFER:

In this section, all the contributions related to knowledge transfer are shown:

- Registered intellectual property as Utility Model: Simulador solar para la caracterización de fotodetectores y células solares by **E. López-Fraguas**, R. Vergaz and J.M. Sánchez-Pena. Nº U201931948 (Spain)
- Registered intellectual property as Software Registry: SUNBOX by E. López-Fraguas, R. Vergaz and J.M. Sánchez-Pena. Nº M-005247/2019 (Spain)
- Building, delivery, and maintenance of 3 SUNBOX. Contract with La Tenda de Modesto S.L.U. through Artículo 83 LOU.

PRIZES:

- 1st price on LightTok contest, organized by the Young Spanish Optics Society in partnership with OSA (The Optical Society), for my informative talk, explaining the contents of my thesis in less than 1 minute. (Talk available on YouTube: https://www.youtube.com/watch?v=FSLLLjhulyI)
- Finalist on THESIS TALK 2019 contest, organized by Carlos III University of Madrid. The contest consisted of explaining my thesis content to a non-specialist audience in less than 3 minutes. (Talk available on https://media.uc3m.es/video/5d2ed2698f420878a08b4567)

OTHER PUBLICATIONS NOT DIRECTLY RELATED WITH THE THESIS:

- S. Masi, C. Echeverría-Arrondo, K.M. Muhammed Salim, T. Tuyen Ngo, P.F. Mendez, **E. López-Fraguas**, D.F. Macias-Pinilla, J. Planelles, J.I. Climente, I. Mora-Sero, "Chemi-Structural Stabilization of Formamidinium Lead Iodide Perovskite by Using Embedded Quantum Dots," *ACS Energy Lett.,* vol. 5, no. 2, pp. 418—427, Jan 2020, doi: 10.1021/acsenergylett.9b02450
    - Q1: 6/112 in Energy & Fuels topic.

Abstract

"Once an idea has taken hold of the brain, it's almost impossible to eradicate" – Cobb, Inception.

The world is going through constant technological changes, and what it seems to be a great improvement to the life in Earth at one moment, can lead to disastrous effects in the future. This has happened several times during the human being history, and one clear example is the climate change, global warming, and greenhouse effect.

Since the industrial revolution, the humanity went through several technological changes: some of them allowed us to progress as a civilization, but others will lead us to self-destruction. A recent example is the release of chlorofluorocarbon (CFC) gases that destroyed a huge part of the ozone layer at the Earth's poles.

Nowadays, one of the big problems that we are facing is the massive amount of carbon dioxide that we are throwing into atmosphere, mainly due to the energy generation activities. That is why this thesis is focused on increase the efficiency of devices that produce energy in a cleaner way, using solar energy. Doing so, in a near future we will be able to replace the actual contaminating energy sources for cleaner, non-emitting, renewable energy sources. Of course, this topic is too general, so this work is split in three big sections, intending to give full coverage to the topic.

The first section is based onto the building blocks of solar harvesting, i.e., the solar cells. The more mature technology, commercially available is the silicon-based solar cell, but in the last years, a lot of technologies were also developed such as organic photovoltaics or perovskites. Each of these technologies have their own fabrication procedure, being the silicon very expensive and high energy demanding, while in the case of organic or perovskite the fabrication procedures are usually solvent-based and cheaper in terms of energy and material costs.

After a brief explanation of the most used thin-film deposition techniques (used on organics and perovskites) the building process of a methylammonium lead iodide perovskite is explained step by step. This fabrication gave a resulting solar cell with a power conversion efficiency of 16.9%. Due to the environmental issues that this novel material can cause (mainly because it has lead in its composition), a lead-free perovskite was also studied (cesium tin iodide). The conclusion extracted from this study is that this lead-free perovskite could have very interesting applications, for example in smart windows, but their electrical conductivity problems should be solved first. Ending with this section, a proof of concept including organic and perovskite photodetectors into a visible light communication system was carried out, resulting in both technologies being able to perform good enough to be part of an audio link (with a bandwith higher than 40 kHz).

Once we have a device to work with, in order to stablish their properties, it should be characterized. That is what the second section is about. This characterization must be done in a standardized way, under certain conditions and circumstances. One of these conditions is to have a stable, well-defined illumination source, that can recreate the standard AM1.5G spectrum (which is the spectrum of light that arrives at the Earth's surface, coming from the Sun). All this restrictions and parameters that

dictates whether a light source is valid for this process or not are defined by the International Electrotechnical Commission under the standard IEC 60904-9. During this thesis, due to the necessity of this light to characterize devices, we decided to create one. This gave birth to SUNBOX, our proprietary solar simulator.

SUNBOX belongs to a AAA-Class according to the IEC standard, which represents the highest quality possible in solar simulators. It is fully based on light emitting diodes and also customizable, with a tunable spectrum that can go from 0.2 to 1.2 suns and has 14 different wavelengths that can be intensity-tuned freely. It is also clearly distinguishable from the commercial ones because its structure is 3D-printed, so it is lightweight and has a low cost. Due to the intellectual property protection as a utility model, only a brief part regarding the electronic design is explained in this document, together with the calibration procedure that was carried out in terms of spectral match, homogeneity, and temporal instability that qualifies SUNBOX as an AAA-Class solar simulator. At the end of this section, some characterizations made with SUNBOX are shown, using different functionalities, to obtain key parameters in different types of solar cells. The characterization methods that were used, such as I-V curves or spectroscopy impedance are also explained along the document.

Finally, in the third section, other approaches to improve the efficiency of the devices were studied, based on the optical treatment of light (light management). This management lies on the ability that some materials have to interact with the incident light, mainly in the form of nanoparticles, nanorods, or small gratings. Using a Finite Element Method simulation software (COMSOL® and JCMSuite®), several results were obtained remarking the importance of the inclusion of a nanostructure inside a device, increasing the amount of photogenerated current by 40% in a hydrogenated amorphous silicon-based device and by 20.5% in a perovskite/silicon tandem solar cell. Furthermore, preliminary results were obtained applying a nanostructure into a deep ultraviolet light emitting diode, that went from a light extraction efficiency value of 4.57% to around 15%, thus, multiplying by three the amount of extracted light with the same electrical power consumption.

In summary, the main conclusion of this work is that it is possible to increase the efficiency of actual devices by and important factor and that there is a lot of room for future improvements. A boost in efficiency can be applied not only using novel materials with better electrical and optical properties, but also optimizing the devices that exist nowadays using light management techniques through the inclusion of nanostructures inside these devices. This has been demonstrated during this work using both approaches: the material science, creating a novel material with a cutting-edge fabrication method, unraveling the properties and applications for this material; and the photonics science, simulating the response of the device with the inclusion of a nanostructure in it, showing an outstanding improvement in all three study cases.

Resumen

"La perfección no se alcanza cuando no hay nada más que añadir, si no cuando no hay nada más que quitar" – Antoine de Saint-Exupéry.

El mundo actual está constantemente sometido a cambios tecnológicos, y lo que en un momento pudo ser un gran avance para la vida en la Tierra, puede ocasionar efectos desastrosos en el futuro. Esto ha ocurrido en varias ocasiones en la historia de la humanidad y claros ejemplos de ello son el cambio climático, el calentamiento global y el incremento del efecto invernadero.

Desde la Revolución Industrial se han producido diversos cambios y avances tecnológicos muy importantes para la sociedad: algunos de ellos nos permitieron avanzar como civilización, pero otros nos dirigen hacia nuestra propia autodestrucción. Un ejemplo reciente podría ser la emisión de los llamados clorofluorocarbonos a la atmósfera, unos gases que destruyeron la mayor parte de la capa de ozono en los polos de la Tierra, ocasionando que una gran parte de radiación solar incidiera en los glaciares polares, incrementando la fusión de ellos y con ello contribuyendo al peligroso deshielo polar.

Hoy en día, uno de los grandes problemas a los que nos enfrentamos es la gran cantidad de dióxido de carbono que estamos vertiendo a la atmósfera, principalmente debido a las actividades de generación de energía. Por ello, el objetivo de esta tesis está centrado en incrementar la eficiencia de los dispositivos capaces de producir energía de una forma más limpia, usando la energía solar. De esta forma, en el futuro cercano seremos capaces de sustituir las fuentes de energía contaminantes que usamos actualmente por otras fuentes de energía mas limpia, renovables y que no emitan gases. Cierto es que este tema puede parecer prácticamente inabarcable, y por ello se ha dividido este trabajo en tres secciones principales que se estudian en detalle, para dar cobertura completa a todo el tema.

La primera sección está basada en el estudio de las unidades básicas de la recolección de energía solar, las celdas solares. La tecnología más madura comercialmente disponible es la celda solar basada en silicio (tanto monocristalino como policristalino), pero durante los últimos años se han desarrollado otras tecnologías tales como las celdas orgánicas o de perovskita. Cada una de estas tecnologías tiene su propio procedimiento de fabricación, siendo las basadas en silicio las más caras de hacer debido a su procesamiento y a la gran cantidad de energía necesaria para su refinado. Sin embargo, en el caso de las celdas orgánicas y de perovskita los métodos de fabricación están basados en solventes y deposiciones de líquido en capas delgadas, lo que las hace mucho más económicas en términos de materiales y de consumo energético.

Después de una breve explicación de las técnicas de deposición de lámina delgada más usadas (aplicables tanto en orgánicas como en perovskitas), se explica el proceso de fabricación paso a paso de una celda solar de yoduro de metilamonio plomo. Esta fabricación dio como resultado una celda solar con un valor de eficiencia del 16.9%. Debido a los problemas ambientales que puede causar este material (ya que contiene plomo, altamente tóxico), durante este trabajo se estudió también una perovskita libre

de plomo (yoduro de estaño cesio). La conclusión principal extraída de este estudio es que esta perovskita libre de plomo puede tener aplicaciones muy interesantes, tales como ventanas inteligentes debido a su transparencia, pero sus problemas de conductividad eléctrica deben de ser resueltos en primer lugar, para conseguir un dispositivo eficiente. Para finalizar esta sección, se llevó a cabo una prueba de concepto que consistió en introducir fotodetectores orgánicos y de perovskita en un sistema de comunicación por luz visible (VLC), comprobando que ambas tecnologías respondían de forma correcta para formar parte de un sistema de transmisión de audio (su ancho de banda era superior a 40 kHz en ambos casos).

Una vez se dispone de un dispositivo funcional, para poder determinar sus propiedades internas, se debe caracterizar. En esto consiste la segunda sección. Estas caracterizaciones deben hacerse siguiendo los estándares correspondientes, bajo ciertas condiciones y en unas circunstancias determinadas. Una de estas condiciones es tener una fuente de luz estable y bien definida, que pueda recrear el espectro AM1.5G (que es el espectro de luz que llega a la superficie de la Tierra emitido por el Sol) para excitar las muestras que se encuentren bajo análisis. Todas las restricciones y parámetros que determinan si una fuente de luz es adecuada o no para este proceso están definidos por la Comisión Electrotécnica Internacional bajo el estándar IEC 60904-9. Durante el desarrollo de esta tesis, debido a la necesidad de caracterizar dispositivos, se optó por crear una de estas fuentes de luz. Así nació SUNBOX, nuestro simulador solar.

SUNBOX pertenece a la clase AAA según el estándar IEC, lo que significa que posee la mayor calidad posible como simulador solar. Está completamente basado en diodos emisores de luz y también es personalizable, con un espectro ajustable que puede cubrir desde 0.2 hasta 1.2 soles. Dispone de 14 longitudes de onda de emisión diferentes que también pueden ser ajustadas libremente, de forma que se pueden realizar análisis en longitudes de onda concretas, tales como azul, ultravioleta o infrarrojo. Es fácilmente distinguible de sus contrapartes comerciales disponibles en el mercado, ya que su chasis está realizado por impresión 3D, así que es muy ligero y de bajo coste. Debido a la protección de la propiedad intelectual bajo un modelo de utilidad y un registro software, solo una parte del diseño electrónico se explica en este documento, junto con todo el procedimiento de calibración que se llevó a cabo en términos de coincidencia espectral, homogeneidad y estabilidad temporal, que clasifican a SUNBOX como un simulador solar de clase AAA. Al final de esta sección, se muestran algunas de las caracterizaciones de dispositivos llevadas a cabo con SUNBOX, usando sus diferentes funcionalidades para obtener parámetros clave de distintos tipos de celdas solares. Los métodos de caracterización llevados a cabo, tales como el trazado de curvas tensión corriente o la espectroscopía de impedancias también se explican en el documento.

Por último, en la tercera sección, se estudian otras técnicas para mejorar la eficiencia de los dispositivos, basadas en el tratamiento óptico de la luz (gestión de la luz o “light management”). Esta gestión de la luz se basa en la habilidad que tienen algunos materiales para interactuar con la luz que incide sobre ellos. Normalmente estos materiales necesitan estar en forma de nanopartículas, nanobarras o pequeñas redes de difracción. Usando varios softwares de simulación (COMSOL® y JCMSuite®) basados en el método de elementos finitos (FEM), se han obtenido varios resultados que

remarcan la importancia de incluir nanoestructuras dentro de los dispositivos, incrementando la cantidad de corriente fotogenerada en un 40% en un dispositivo basado en silicio amorfo hidrogenado y en un 20.5% en un dispositivo basado en un tándem de perovskita y silicio monocristalino.

Además, se han obtenido resultados preliminares que demuestran que estas nanoestructuras pueden ser también muy efectivas no solo en dispositivos receptores de luz, sino también en emisores. En este caso se aplicó una nanoestructura a un diodo emisor de luz ultravioleta profunda, que mejoró su eficiencia de extracción de luz de un 4.57% a alrededor de un 15%, triplicando la cantidad de luz emitida con el mismo consumo de potencia eléctrica.

En resumen, la conclusión principal de este trabajo es que es posible incrementar la eficiencia de los dispositivos actuales de una forma sustancial, quedando aún mucho espacio para mejorar. Se ha demostrado que un incremento en la eficiencia puede obtenerse no solo usando materiales novedosos con mejores propiedades ópticas y eléctricas, sino también optimizando los dispositivos existentes actualmente usando técnicas de gestión de la luz a través de la inclusión de nanoestructuras en estos dispositivos. Respecto a la primera aproximación, relacionada con la ciencia de materiales, en este trabajo se ha fabricado un material novedoso usando una técnica de fabricación poco explorada en estas aplicaciones (co-evaporación), descubriendo las propiedades y posibles aplicaciones de este material. Respecto a la segunda aproximación, relacionada con la fotónica, se han creado diseños de nanoestructuras y se ha simulado su respuesta, descubriendo una mejora muy importante en la eficiencia de los tres dispositivos estudiados.

Table of contents

List of Figures

List of Tables

Chapter 1: Introduction

"And so, we start anew" – Medivh, The last guardian.

Our planet is dying, and we must take full responsibility of it. Since the industrial revolution, the humanity has been through a lot of technological changes, and some of them have caused huge damage to our environment. We are running out of time, but we still have the opportunity to fix this problem.

The global warming is one of the biggest threats to the life as we know it and can lead to devastating effects to our planet. Actually, a lot of these effects that were predicted years ago are happening nowadays, such as the ice melting at the Earth's poles, the rising of the water level or the early flowering of vegetation. Moreover, these effects will be growing, and each year will be bigger, having a stronger impact. According to the Intergovernmental Panel on Climate Change, "the net damage costs of climate change are likely to be significant and to increase over time" [1].

Even though all these destructive events are happening in the real world right now, some people insist on not giving the right importance to it or saying that the human contribution to this climate change is negligible (even saying that the global warming is not real).

The scientific community is clear at this point. The global warming has reached alarming levels since the mid-20th century, and these high levels are produced due to the human activity (with more than 95% confidence among 1300 independent scientist from countries all over the world). This was stated in *"The Scientific Consensus on Climate Change"* in 2004 [2].

One of the main culprits of this warming is the increment of the greenhouse effect. This effect is not bad by itself, in fact, it regulates the temperature of our planet, making it habitable. The effects of having not enough greenhouse effect or an excess of it can be seen looking at our neighboring planets. On one side, Mars, with very small greenhouse effect, cannot hold temperatures high enough to handle any kind of known lifeform, due to the lack of greenhouse gases, such as water vapor or carbon dioxide, in its thin atmosphere. On the other side, Venus has a huge greenhouse effect, with its mainly carbon dioxide atmosphere (154 thousand times the amount that is on Earth). This makes the surface of Venus hot enough to even molt some metals [3].

We have been in the "sweet point" over all our existence, but during the last century an abnormal increase in Earth's temperature have been detected. And this is an increase that has nothing to do with the variation of the solar energy that the Earth receives, as it can be seen in Figure 1-1.

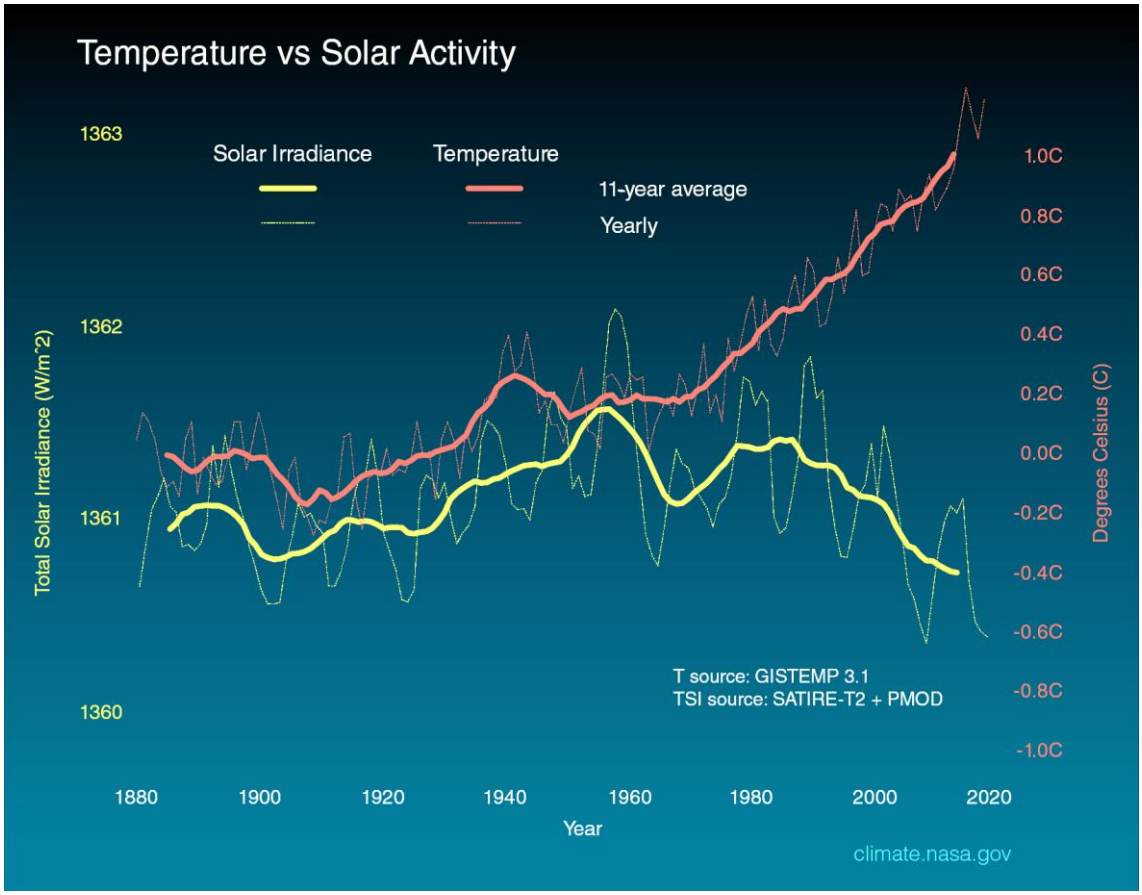

Figure 1-1 Comparison between Solar Irradiance and Global Heating. Adapted from [3].

Here, it can be seen that the global warming followed the trend of the solar irradiance until 1960 approximately, and then diverts, growing without control until nowadays.

So, what happened in those decades? Figure 1-2 is almost self-explanatory. Around 1950, the CO_2 emissions started to grow in an exponential way globally. However, the main part of the gases is emitted by some countries like China (9.8 billion tons) or United States (5.3 billion tons), followed by India and Russia, while the emission of all the African continent, South America and Oceania together results in 2.9 billion tons (see Figure 1-3).

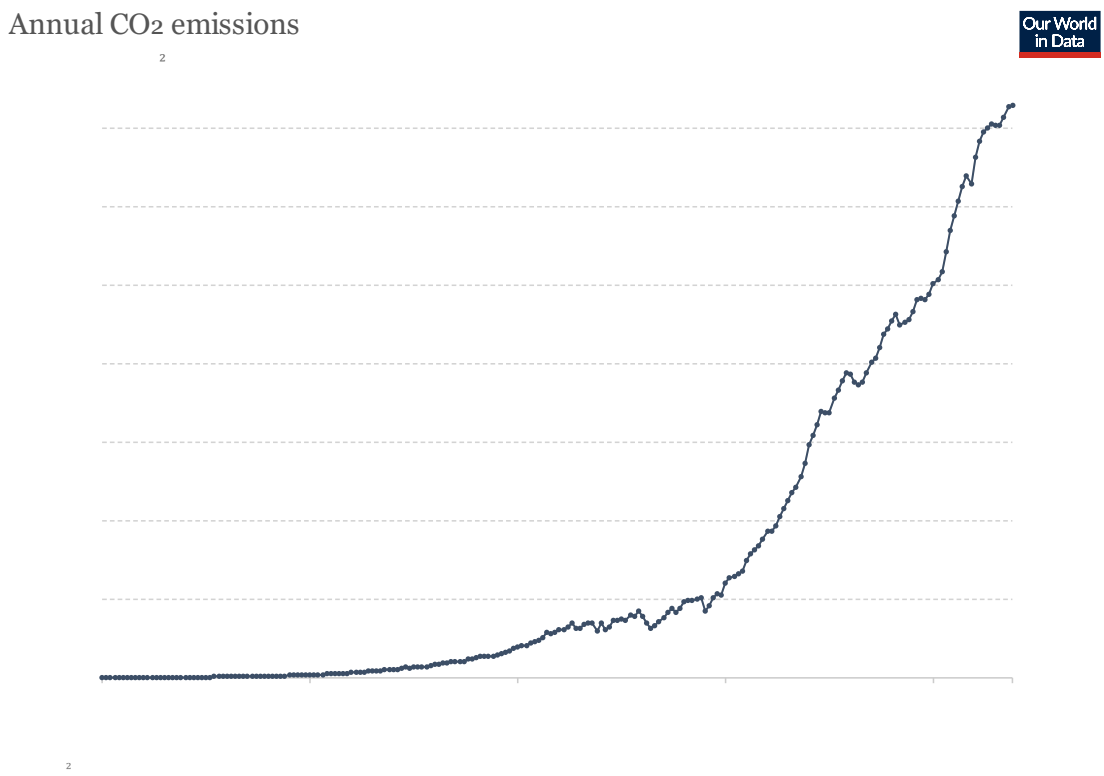

Figure 1-2 Annual CO_2 emissions worldwide. The exponential growth starts around 1950. Obtained from [4]

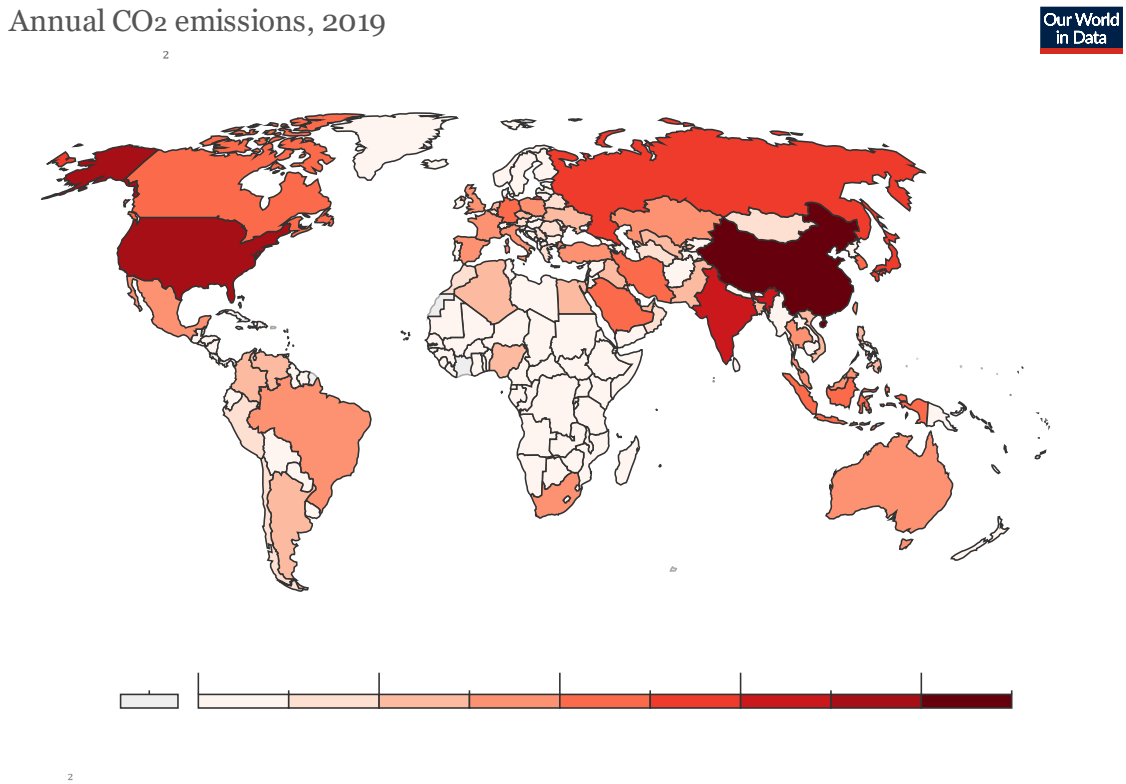

Figure 1-3 Annual CO_2 emissions per country in 2019. Obtained from [4].

One of the multiple solutions to mitigate the damage already caused and to stop this auto-destructive process is to stop the emission of greenhouse gases, especially CO_2. Although the carbon dioxide is the gas with less "Global Warming Power" (i.e., its effect is not as big as other gases such as nitrous oxide or methane) its huge emissions combined with its high durability in the atmosphere, make the CO_2 the main culprit of global warming [5].

CO_2 gas is generated in several human activities, so the emission should be reduced in the most efficient way. The most emitting activities should be targeted and modified in order to cut the emissions off. Figure 1-4 shows the global CO_2 emissions by sector. The remarkable factor is that almost three quarters of the emissions are produced by the energy sector (73.2%).

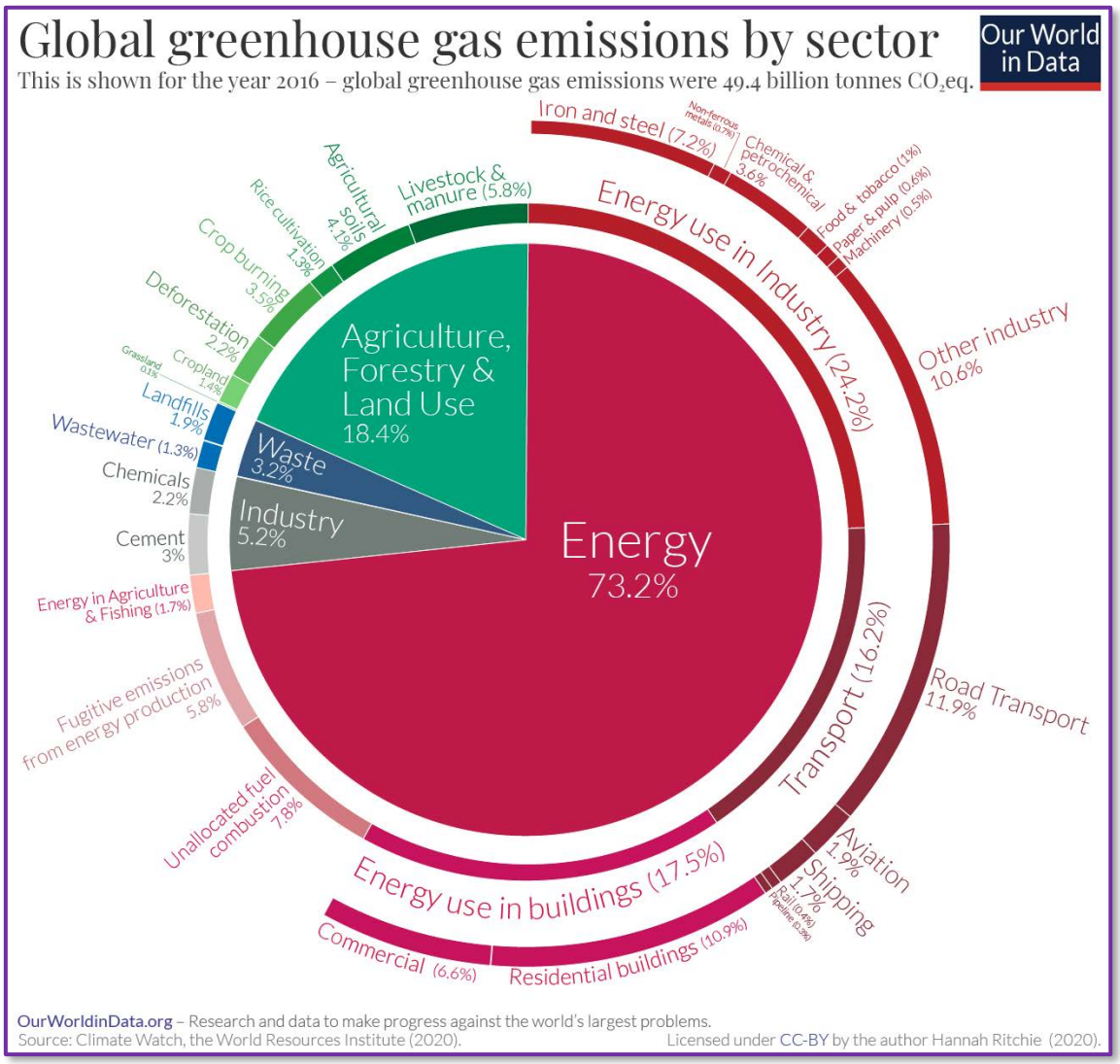

Figure 1-4 Global CO_2 emissions by sector in 2016. Obtained from [6].

Thus, making an ecological transition to produce energy using clean, non-emitting sources can be one successful approach to reduce the CO_2 emission.

Among all the clean sources that are available today, this thesis work is focused on one of the most promising, the solar energy. The basic principle behind this energy is well-known, the conversion of the light that comes from the Sun into electricity.

This phenomenon was first discovered by the French physicist Edmond Becquerel in 1839 [7] while he was experimenting with metallic electrodes into a conductive solution (electrochemical cell). During the following years, some experiments related with selenium were carried away, revealing that selenium could generate electricity when exposed to light.

The first selenium solar cell was finally developed at 1883 by the American inventor Charles Fritts [8]. But the working principle behind this phenomena was not explained until 1905, when Albert Einstein theorized about the so-called "photoelectric effect" [9]. Years later, in 1921, Albert Einstein was awarded with the Nobel Prize due to this discovering. Once this effect was explained and after the development of the first silicon solar cell by Bell Labs in 1954 [10], the efficiency race begun.

This piece of history leads us to the actual state of the art, where silicon solar panels are commercialized and slowly introduced into the electricity generation scheme of the countries. Figure 1-5 shows the electricity generation split by sources in Spain, 2020. It can be seen that adding solar photovoltaic and solar thermal generation, around 20 GWh were produced by solar energy, which represent around an 8% of the total energy generation of the country.

Applying some of the efficiency techniques studied in this thesis, we intend to push further the efficiency of the devices, in order to be able to suppress the non-renewable and gas emitting energy sources (56% of the energy generated in Spain during 2020 was produced using non-renewable energy sources).

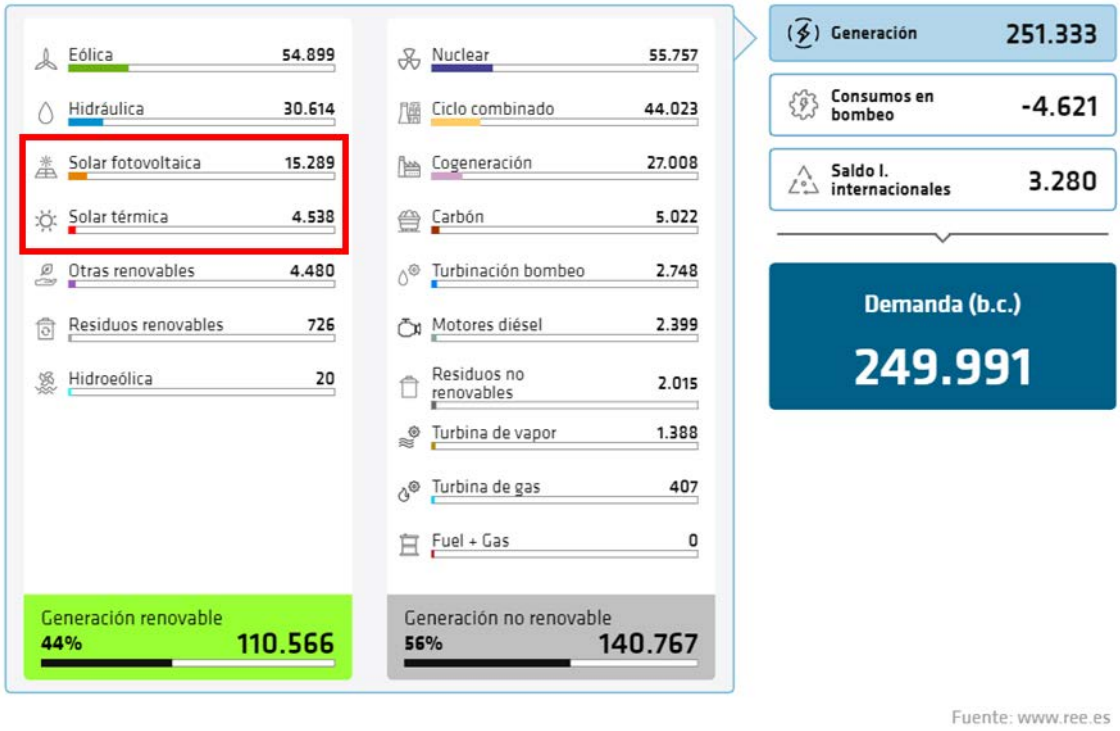

Figure 1-5 Electricity generation split by source in Spain during 2020. The units are GWh. Source: Red Eléctrica de España.

Although it is usually argued that the development and deployment of solar panels implies a huge cost in energy that comes from non-renewable sources and also generates CO_2 emissions [11], this statement is revoked when the energy to fabricate

the solar panels comes from a renewable, non-emitting source. Also, this huge amount of energy is consumed mainly in first generation solar cells (as the monocrystalline silicon solar cells). However, the solar cell research has been growing, together with material science, so other materials can be applied to manufacture solar cells, such as organic materials or perovskites, which consume much less energy during their fabrication [12].

In fact, the National Renewable Energy Laboratory has estimated that during their life cycle, the crystalline silicon solar cells produce around 46g of CO_2 per kWh, versus the approximately 1000g of CO_2 per kWh that the coal-based sources produce. So, even assuming the cost of fabrication, the carbon footprint is reduced more than 20 times [13]. This fact shows that solar energy can be a good candidate to reduce the carbon dioxide emissions to the atmosphere, even more if an efficiency improvement is achieved.

This efficiency increase can be achieved by material science, developing new materials with enhanced properties. The big solar evolutions have come from here (e.g., first, second, third generation solar cells).

But this is not the only path that can be taken to improve the cells. Photonic science can be applied in this field to manage the light in several ways. One of the most common applications of photonics science is the light trapping, which consists in concealing the received light inside the active layer of the solar cell, forcing its absorption and thus, increasing the efficiency of the device [14].

This thesis is focused onto solar cells, going through three main and well differentiated topics: last-generation solar cells, the characterization methods of the solar cells and photodevices and the inclusion of nanostructures inside the photodevices to increase their efficiency. Thus, the three topics of this thesis are different enough between themselves to have each one its own extended introduction in their corresponding chapter.

1.1. Motivation

Summarizing the previous introduction, in this section the motivation of this work is explained.

During the last years, even decades, a lot of scientists have been warning about the climate change and Earth's warming, mainly due to the greenhouse effect. For example, the work of Bolin and Doos comes from more than 30 years ago (1989) [15]. Furthermore, Carl Sagan warned about the dangers of climate change in his famous book and TV series *Cosmos*, from 1980 (more than 40 years ago) [16]. It has been studied that not all the gases contribute in the same way to the greenhouse effect [17], but all of them do it in some manner. One source of these gases is the power and energetic industry, that uses fossil fuels to generate electricity. Each year the electricity needs for the world increase, according to the data collected by the International Energy Agency [18], but the emission of gases cannot be increased further (actually, it should be reduced). From here it arises the fundamental motivation of this work, including in the equation sources of renewable, clean energy, with no gas emission, mainly centered in solar energy.

The main drawbacks of the solar cells is that they have very low-efficiency and are not cost-effective [19], [20]. These facts are true mainly in classical solar cells, i.e., silicon based. However, since the beginning of the solar cells around 1950 [10], this topic has gone from first generation solar cells, based on thick layers of mono and polycrystalline silicon, to second generation or thin-film solar cells (amorphous silicon, cadmium telluride, copper indium gallium selenide), ending with the third generation solar cells, also called emerging photovoltaics, which includes a wide range of technologies such as organic solar cells, dye-sensitized, quantum dots and the famous perovskites. The philosophy of these last ones is trying to achieve or even surpass the efficiency of the previous generation cells, but using less and cheaper material, i.e., they are intended to be more efficient and more cost-effective.

Besides the material used to create them, another method to increase the efficiency of a solar cell or any kind of photodevice, goes through a light management process, in which the light path can be modified to improve the properties of the device (e.g., absorbing more light in the case of a solar cell). This management can be accomplished using nanostructures, defined as structures which size is in the same scale as the visible wavelengths (in the order of nanometers). This small size allows these structures to interact with the light, producing diffractions and other non-classical effects, such as resonances, directional scattering, or anti-reflection phenomena [21].

Along this work I will show how some solar cells are fabricated, how they are characterized and how their efficiency can be improved making an optical management of light, in such a way that in a near future we can make low-cost devices with the highest possible efficiency to make them cost-effective and thus, a deployment of these devices could be done at a big scale.

1.2. Objectives

The specific goals that we want to achieve during this work are divided as a function of their topic, being each topic further explained in each of the following chapters:

- Regarding the study of last-generation solar cells:
    - Exploring the new technologies that arose a few years ago, such as perovskites or organic solar cells, to check their strengths and weaknesses and how they behave in a complete electronic system.
    - Understanding and learning the fabrication methods for solar cells, mainly solvent-based.
    - Making a proof of concept of a perovskite device with an efficiency over 15%.
    - Studying a lead-free perovskite material to achieve a more environmental-friendly substitute of the typical lead halide perovskite.
    - Including new generation devices in working applied systems, such as Visible Light Communication system, checking their new properties and characteristics and the added value that they provide to them.
- Regarding the characterization methods of solar cells:
    - Studying and analyzing the most common methods used for solar cell characterization (I-V curves, impedance spectroscopy, etc…)

    - Designing, building, and calibrating a low-cost solar simulator that can be used by any small laboratory around the world to characterize their own solar cells. It must be portable, small-sized and follow the appropriate standards. Also, it should have several working modes, to cover as much characterization techniques as possible.
- Regarding the inclusion of nanostructures in solar cells:
    - Studying and learning both theory behind nanostructures and how to compute their effects on light management using Finite Element Method software.
    - Successfully designing a structure that increases the efficiency on several types of solar cells.
    - Exploring the application of nanostructures not only in solar cells but also in emitting devices, as a new research line, applying the nanostructures to light emitter devices and checking if an increase of efficiency is also possible. These improved emitters could enhance the performance of several devices, such as our own solar simulator from the last section.

1.3. Document Structure

This document has a very clear structure, sectioned in several chapters:

- Chapter 1: In this chapter a brief introduction is done, along with the motivation for this work and the objectives that should be fulfilled.
- Chapter 2: This chapter focuses on the last generation solar cells. It explains some of the most recent technologies and their fabrication methods. In addition, it shows the step-by-step fabrication of a Methylammonium Lead Iodide perovskite solar cell, that I developed during my learning process and reached an efficiency of around 17%. Furthermore, this chapter goes through a material analysis and fabrication of Cs_2SnI_6 lead-free perovskite, using the co-evaporation technique. This study has expanded the state of the art due to the novelty of the material and the fabrication technique. Finally, the inclusion of an organic and a perovskite photodetectors in a visible light communication system is studied.
- Chapter 3: Along this chapter, the most used characterization techniques are explained. Moreover, this chapter explains the design, fabrication, development, and distribution of SUNBOX, which is a proprietary solar simulator created during this thesis. This device has been used not only in my Research Group, but also has been protected and licensed to a Company, which has sold three of them to other Groups, so far. This is a result in terms of Research transfer to the industry, which is one of the most remarkable achievements of this Ph.D. work as Engineer.
- Chapter 4: In this chapter, some of the light management approaches applied to devices using nanostructures are explained. Furthermore, several nanostructure application examples of studies done during this work are exposed. Nanostructures were applied to an amorphous hydrogenated silicon solar cell, a perovskite-silicon tandem solar cell and even a deep ultraviolet light emitting diode, with their corresponding efficiency increase. The works based on solar cells generated a total of three scientific publication, while the emitter study is still in progress, pushing the actual state of the art.

- Chapter 5: This final chapter concludes summarizing the goals achieved during this thesis and some future works that can be explored further.
- Appendix A: Here a list of contributions by the author, directly related and not so close-related to the thesis are shown. Papers, congress contributions and knowledge transfer to the industry is also shown.

1.4. Bibliography

[1] R. Jackson, "The Effects of Climate Change," *Climate Change: Vital Signs of the Planet*. https://climate.nasa.gov/effects (accessed May 06, 2021).

[2] N. Oreskes, "The Scientific Consensus on Climate Change," *Science*, vol. 306, no. 5702, pp. 1686–1686, Dec. 2004, doi: 10.1126/science.1103618.

[3] "The Causes of Climate Change," *Climate Change: Vital Signs of the Planet*. https://climate.nasa.gov/causes (accessed May 06, 2021).

[4] "CO2 emissions," *Our World in Data*. https://ourworldindata.org/co2-emissions (accessed May 06, 2021).

[5] July 16 and 2019 Melissa Denchak, "Greenhouse Effect 101," *NRDC*. https://www.nrdc.org/stories/greenhouse-effect-101 (accessed May 06, 2021).

[6] "Emissions by sector," *Our World in Data*. https://ourworldindata.org/emissions-by-sector (accessed May 06, 2021).

[7] M. E. BECQUEREL, "Memoire sur les Effets Electriques Produits sous l'Influence des Rayons Solaires," *Comptes Rendus Hebdomadaires des Seances de L'Academie des Sciences*, vol. 9, pp. 561–567, 1839.

[8] Fritts, "On a New Form of Selenium Photocell," *American J. of Science*, vol. 26, p. 465, 1883.

[9] "This Month in Physics History." http://www.aps.org/publications/apsnews/200501/history.cfm (accessed May 07, 2021).

[10] "This Month in Physics History." http://www.aps.org/publications/apsnews/200904/physicshistory.cfm (accessed Dec. 22, 2020).

[11] D. Chandrasekharam and G. Ranjith Pathegama, "CO2 emissions from renewables: solar pv, hydrothermal and EGS sources," *Geomech. Geophys. Geo-energ. Geo-resour.*, vol. 6, no. 1, p. 13, Dec. 2019, doi: 10.1007/s40948-019-00135-y.

[12] L. Qiu, L. K. Ono, and Y. Qi, "Advances and challenges to the commercialization of organic–inorganic halide perovskite solar cell technology," *Materials Today Energy*, vol. 7, pp. 169–189, Mar. 2018, doi: 10.1016/j.mtener.2017.09.008.

[13] "Search: life cycle greenhouse gas emissions from solar photovoltaics." https://search4.nrel.gov/texis/search/?mode=&opts=&pr=metanrel&dropXSL=html&sq=&prox=page&rorder=750&rprox=1000&rdfreq=0&rwfreq=250&rlead=1000&rdepth=62&sufs=1&order=r&query=life+cycle+greenhouse+gas+emissions+from+solar+photovoltaics (accessed May 06, 2021).

[14] K. Li *et al.*, "Light trapping in solar cells: simple design rules to maximize absorption," *Optica, OPTICA*, vol. 7, no. 10, pp. 1377–1384, Oct. 2020, doi: 10.1364/OPTICA.394885.

[15] B. Bolin and B. R. Doos, "Greenhouse effect," Jan. 1989, Accessed: Apr. 14, 2021. [Online]. Available: https://www.osti.gov/biblio/6761224

[16] “COSMOS | CARL SAGAN | Casa del Libro,” *casadellibro*. https://www.casadellibro.com/libro-cosmos/9788408053040/978634 (accessed Apr. 22, 2021).
[17] H. Rodhe, “A Comparison of the Contribution of Various Gases to the Greenhouse Effect,” *Science*, vol. 248, no. 4960, pp. 1217–1219, Jun. 1990, doi: 10.1126/science.248.4960.1217.
[18] “Electricity Information 2019 – Analysis,” *IEA*. https://www.iea.org/reports/electricity-information-overview (accessed Apr. 22, 2021).
[19] Ecavo.com, “Solar Energy Disadvantages: The Top Drawbacks of Solar Power,” *Ecavo*, Dec. 16, 2016. https://ecavo.com/solar-energy-disadvantages/ (accessed Apr. 22, 2021).
[20] “Advantages & Disadvantages of Solar Energy.” https://www.greenmatch.co.uk/blog/2014/08/5-advantages-and-5-disadvantages-of-solar-energy (accessed Apr. 22, 2021).
[21] G. Kang, J. Yoo, J. Ahn, and K. Kim, “Transparent dielectric nanostructures for efficient light management in optoelectronic applications,” *Nano Today*, vol. 10, no. 1, pp. 22–47, Feb. 2015, doi: 10.1016/j.nantod.2015.01.008.

Chapter 2:Last generation solar cells fabrication

"Any sufficiently advanced technology is indistinguishable from magic" – Arthur C. Clarke

In this Chapter, we will start reviewing the state of the art of different solar cell technologies and focusing mainly on the game-changer of the decade: perovskites. Then, I will go through the most used fabrication techniques to develop high efficiency solar cells, stressing the ones that I have experience with, due to my research stay at the Institute of Advanced Materials at Jaume I University of Castellón. After that, I will explain the work that I have done related to the developing and characterization of a lead-free perovskite (we will see why this is important). Finally, I will show some examples of inclusions of these devices into a real-world application, a Visible Light Communications (VLC) system.

2.1. The revolution of the decade: Perovskites

Since 1950, several types of technology have been discovered, as previously explained. But in the most recent times, one material has demonstrated outstanding properties, which made it one of the most interesting research topics. This material is perovskite. Checking the state of the art for the efficiency vs time (Figure 2-1) we can see the huge improvement slope of perovskite, which went from an efficiency of 3.8% in 2009 [1] to 25.5% in 2020 [2]. It is worth mentioning that this increment is the same that monocrystalline silicon experimented since the first practical silicon solar cell by Bell Labs back in 1954 [3]. So, in only ten years of research, perovskite achieved the levels that monocrystalline silicon reached with more than 50 years of development. Naturally, this has been a huge claim for scientists all over the world to start their research in the perovskite field. In fact, we can see this effect if we check the number of publications over time dedicated to this topic. Figure 2-2 shows the number of publications that appears at Web of Science [4] if we look for "perovskite solar cell". It is impressive to see this almost exponential behavior in the amount of published content.

But, what really perovskite is? Actually, perovskite is a mineral with the composition $CaTiO_3$ (Calcium Titanium Oxide), discovered in 1839 and named after Russian mineralogist Lev Perovski [5]. However, its name is also used to name the materials with the same crystal structure as $CaTiO_3$. So, we can define perovskite as any material with a generic crystal structure of ABX_3, being A an organic/inorganic cation, B a metal cation smaller than A, and X an anion (usually oxygen or halide) that bonds with both cations. The crystal structure can be seen at Figure 2-3 [6].

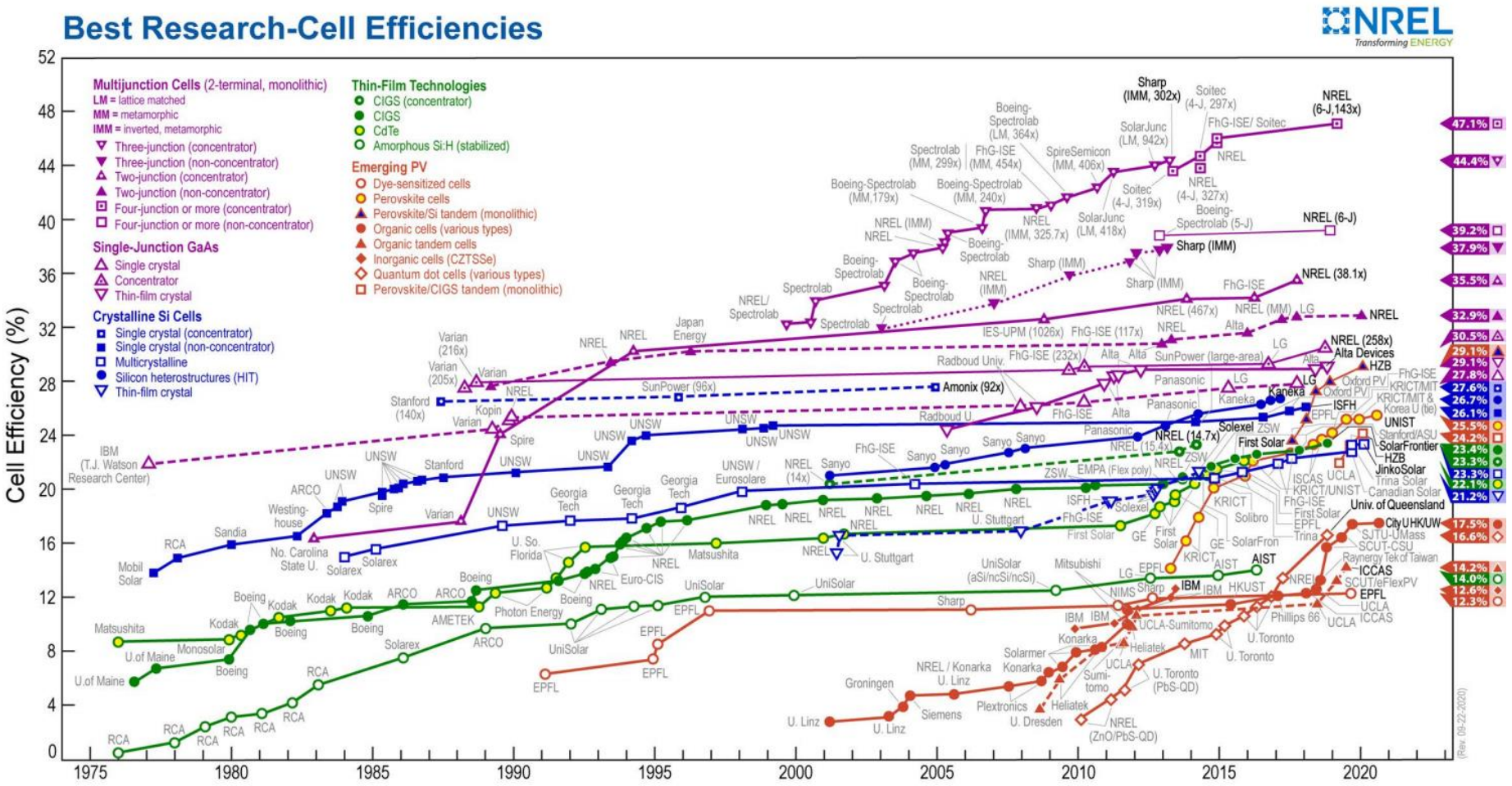

Figure 2-1 Best Research-Cell Efficiencies graph obtained from National Renewable Energy Laboratory [2].

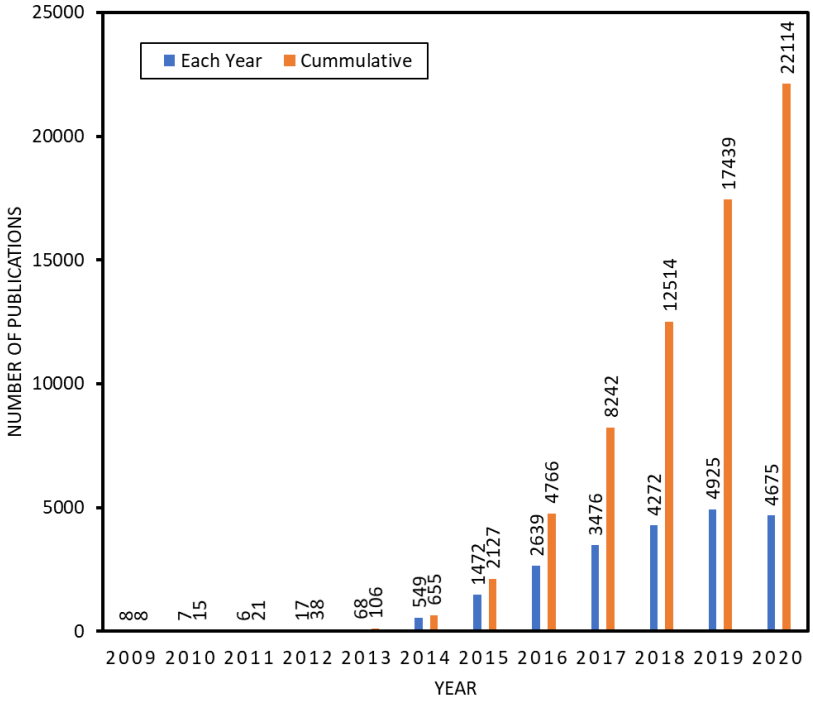

Figure 2-2 Perovskite solar cell related publications during last decade.

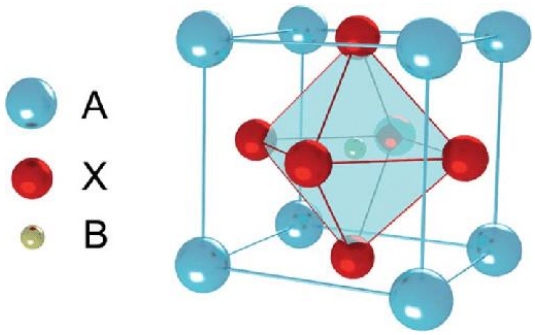

Figure 2-3 Crystal Structure of Perovskite ABX3, obtained from [6]

Regarding photovoltaics, the journey started when Kojima et al. [1] at 2009, used two organolead halide perovskite nanocrystals ($CH_3NH_3PbI_3$ and $CH_3NH_3PbBr_3$) as photosensitizers for TiO_2 in a dye-sensitized solar cell (DSSC). Surprisingly, they discovered that the DSSC based on $CH_3NH_3PbI_3$ had an efficiency of 3.8% and absorbed light up to 800nm. Checking that MAPI did behave as a semiconductor, the technology moved from a DSSC approach to a single junction approach, the one that was used in c-Si solar cells.

So, since the beginning of perovskite solar cells, $CH_3NH_3PbI_3$ (also known as MAPI) has been the most famous material, but there are a huge number of combinations. Typical configurations use Methyl-ammonium (MA), Formamidinium (FA), Cesium (Cs) or Rubidium (Rb) at A position; Lead (Pb), Tin (Sn) or Germanium (Ge) at B position; Iodine (I) or Bromine (Br) at X position. This implies the opening of a huge research field in which a lot of materials must be developed and characterized. Nevertheless, not every combination generates a success, being some of them unstable.

To predict if a certain combination will generate a stable compound, some computational approaches can be applied [7], [8] but usually they are too expensive in resources. To avoid these complex procedures, a geometrical approach is used, known as the Goldschmidt tolerance factor [9], showed in Equation 1:

$$t = \frac{r_A + r_X}{\sqrt{2}(r_B + r_X)} \quad (1)$$

where r_A, r_B and r_X stand for the ionic radius of A, B and X compounds. This t factor can predict the fitting of the compounds inside the cubic lattice, 1 meaning a perfect fitting, and $0.8 \leq t \leq 1$ a feasible, stable fitting. Notwithstanding, Travis et al. in 2016 [10] discovered that this factor was not precise determining the stability in halide perovskites and proposed another approach capable of predicting correctly 31 of 32 inorganic iodide perovskites and 147 out of 159 ABX_3 compositions. Studies like this one show the right combinations to build a perovskite. This scan over all the possible combinations is an arduous work, so a huge research field is open.

In order to estimate what would be the power conversion efficiency (PCE) theoretical limit of some of these perovskites, Qian et al. [11] performed Density Functional Theory (DFT) calculations over the next combinations of ABX_3, being A= CH_3NH_3, $CH(NH_2)_2$, Cs, Rb; B= Pb, Sn, Ge; X=I, Br, Cl, F. Also, they applied Shockley-Queisser maximum solar cell efficiency and Spectroscopic Limited Maximum Efficiency (SLME) mathematical models. The results of their study are shown in Table 2-1, where they are compared with the most recent experimental results.

	$FAPbI_3$	$MAPbI_3$	$MASnI_3$	$CsSnI_3$	$FASnI_3$	$CsGeI_3$
Theoretical	26.4%	26.7%	19.9%	25.6%	26.9%	27.9%
Experimental	16.4% [12]	25.5% [2]	6.4% [13]	2.58% [14]	7.7% [15]	0.11% [16]

Table 2-1 - Theoretical and experimental power conversion efficiencies of different perovskite combination.

We can see that the experimental results using MAPI are very close to their theoretical limit (25.5% vs 26.7%). This PCE value, combined with the low cost of fabrication compared with the silicon solar cells, and the solvent processing techniques that ease the manufacturing, make perovskite an ideal candidate to surpass the silicon-based technology. However, currently there are several concerns about the usage of MAPI in real world applications, regarding the life cycle, stability, and toxicity.

One of these main concerns is the lead toxicity, due to the degradation and decomposition of MAPI under high temperatures and the solubility of lead in water, which can affect in a serious way to the environment [17]. This is why lead-free perovskite is another hot-topic nowadays, with perovskites such as tin-based ($CsSnI_3$, $MASnI_3$) or tin-germanium alloys ($CsSn_{0.5}Ge_{0.5}I_3$) [18].

2.2. Fabrication techniques: state of the art

One of the main differences between the silicon and perovskite solar cells is the fabrication procedure. In silicon, high temperatures and complex processes are required [19], while perovskite cells use a solvent-based approach, reducing the manufacturing

costs. In this section I will talk about the most common fabrication procedures regarding perovskite technology, although these methods are so generic that can be applied to any solvent-based technology, such as organic solar cells. It is worth mentioning that, in the following section (2.3), a practical example will be exposed: the fabrication of a lead-free double perovskite ($CsSnI_3/Cs_2SnI_6$).

2.2.1. Spin coating

This technique is the angular stone of the solvent-based thin film depositions and maybe the most common one. The spin coating technique uses the centripetal force generated by a rotating substrate to spread evenly a solution, forming a thin layer of liquid material over the substrate. A schematic of this process can be seen at Figure 2-4 [20]. There are two ways to apply the solution:

- Static spin coating: In this approach, the solution is poured over the substrate (usually with a pipette) evenly, and then the rotation of the substrate starts.
- Dynamic spin coating: In this approach, the substrate starts spinning, and then, when it reaches the desired speed, the solution is deposited over the spinning substrate.

It is common to use the dynamic deposition as a general method because it avoids the evaporation of the solvent while we are setting up the spinner. This method also achieves better spreading of the solution with less quantity of it, since the solution is pushed outwards as soon as it touches the rotating substrate. Although, this approach is also the most difficult to apply, because it requires skill and practice to drop the solution in the middle of the substrate (to avoid center holes) and in a fast, constant, and smooth way, to avoid the formation of several layers or the injection of bubbles in between.

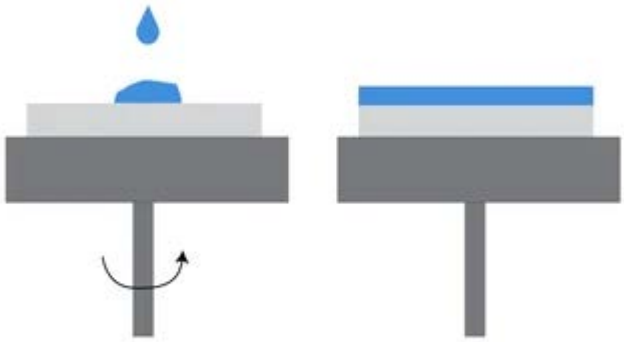

Figure 2-4 Spin coating process illustration.

On the other hand, the static deposition is typically used in special cases, such as low spinning speeds (when the solution cannot spread all over the substrate, due to the low centripetal force exerted by the rotational motion) or high viscosity solutions. As commented before, the big disadvantage of this method is the poor substrate to substrate film uniformity, due to the time in which the solvent eventually evaporates

while the spin coater is turned on, and that is why often a dynamic deposition is preferred.

We have seen that both approaches can be used, but how is the thickness of the deposited layer controlled in this deposition method? The layer thickness is one of the main parameters that we want to control, and this is not trivial regarding this method. As a rule of thumb, it is stated that the layer thickness is inversely proportional to the angular speed of the substrate, as seen in Equation 2.

$$h_{layer} \propto \frac{1}{\sqrt{\omega}} \tag{2}$$

being h_{layer} the layer thickness and ω the angular speed.

The disadvantage here is that this is an experimentally determined equation, similar to a calibration procedure, in which we must make several depositions at different speeds and measure the resulting thicknesses to obtain the final equation. Using those results we can predict the thickness at a certain speed. Several researchers have tried to determine this value theoretically, such as Emslie, Bonner and Peck in 1958 [21], which developed Equation 3:

$$h = \frac{h_0}{\sqrt{(1+\frac{4\rho\omega^2}{3\eta}h_0^2 t)}} \tag{3}$$

where t is the time since the start of the process, h is the liquid thickness after the spinning process (this equation does not consider the evaporation of the solvent), h_0 is the initial uniform thickness of the film ($t = 0$), ρ is the fluid density, η is the fluid viscosity, and ω is the angular velocity. To calculate the final dry film thickness, we can use the concentration of the solution to estimate the amount of solvent evaporated.

More modern approach comes from Meyerhofer in 1978 [22]. Here, a new equation that includes the evaporation of the solvent was developed (Equation 4).

$$h = \left(\frac{3}{2}\right)^{\frac{1}{3}} k^{\frac{1}{3}} C_0 (1 - C_0)^{-\frac{1}{3}} \rho^{-\frac{1}{3}} \eta_0^{\frac{1}{3}} \omega^{-\frac{1}{2}} \tag{4}$$

where ρ and η_0 are the density and the viscosity of the fluid, C_0 is the initial concentration of solute, ω is the angular velocity and k is a constant related to the coating solvent. This equation demonstrates the relationship between the final thickness and the speed of the substrate, as stated in Equation 1. Nevertheless, even in this last equation some factors are ignored, so usually the so called “spin curve” is used. As explained earlier, this method consists of measuring the thickness of several depositions at different speeds to generate a curve, and then make an interpolation to estimate the ideal speed for the target thickness. Some “spin curves” associated with two common resists (poly methyl methacrylate/PMMA and methyl methacrylate/MMA) can be found at [23].

Regarding the machinery, spin coating can be done with one compact machine, that can fix the substrate to the rotary platform, with or without vacuum [24], [25]. Both examples can be seen at Figure 2-5.

Figure 2-5 Spin coater with vacuum from Laurell [24] (left) and without vacuum from Ossila [25] (right).

2.2.2. Dip coating

The dip coating method is based on the immersion of a substrate on a solution, followed by a careful removal at a controlled speed. This allows the deposition of the solution mainly over both faces of the substrate. The thickness is adjusted controlling the withdrawal speed. Once the substrate is removed, some time is needed to evaporate the solvents and volatile compounds, leaving a dry thin film coating. A schematic vision of the procedure is shown in Figure 2-6 [26].

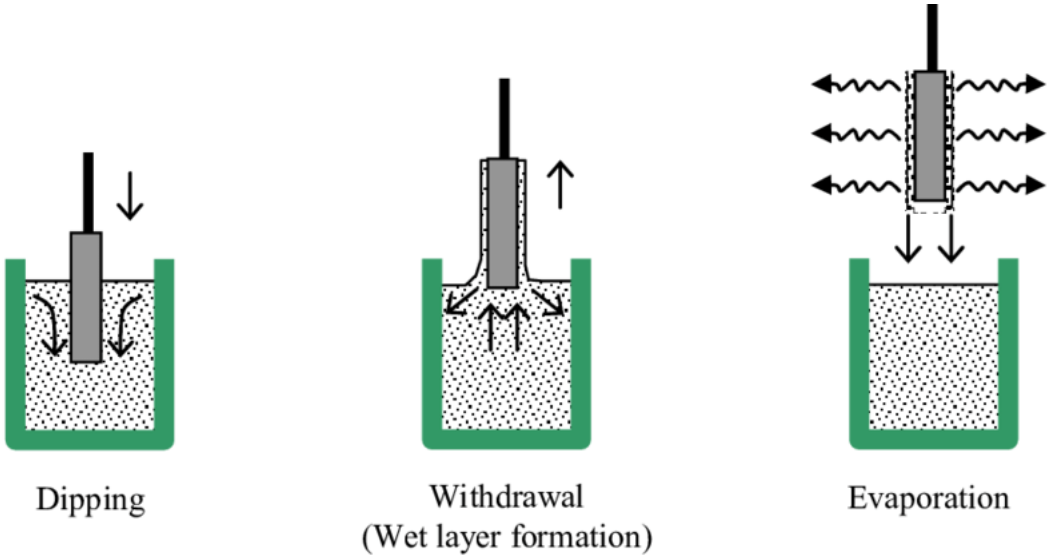

Figure 2-6 Dip coating schematic procedure [26].

In this method, the calculation of the film thickness is not something trivial, due to its dependence on several factors. This thickness depends on a delicate equilibrium

between forces that pull the liquid back to the reservoir and forces that retain the liquid onto the substrate. Depending on this equilibrium three different regimes are stablished, each one with their corresponding equation.

- Viscous flow regime: viscous solutions with a high withdrawal velocity cause this regime. Thickness dependence is shown in Equation 5

$$h_0 = c\sqrt{\frac{\eta U_0}{\rho g}} \tag{5}$$

  where ρ and η stands for density and viscosity of the fluid, U_0 is the withdrawal velocity, g is the gravitational constant and c is a constant related with the curvature of the dynamic meniscus (the one that is formed between the substrate and the liquid reservoir surface during the extraction process).
- Drainage regime: When the viscosity or the withdrawal speed is lower, the process no longer belongs to viscous flow regime, but to drainage regime. Now the process is also surface-tension dependent. At this regime, the Landau-Levich equation is used (Equation 6) [27].

$$h_0 = c\frac{(\eta U_0)^{\frac{2}{3}}}{\gamma_{LV}^{\frac{1}{6}}(\rho g)^{\frac{1}{2}}} \tag{6}$$

  where γ_{LV} is a constant related to the surface tension of the solution. The other parameters are the same as in Equation 5.
- Capillary regime: This regime only appears when very low withdrawal speeds are applied (<0.1 mm/s). That means that the rate of evaporation of the solvent (drying process) is now considered. Thickness in this regime is estimated using Equation 7.

$$h = \frac{cM}{\alpha\rho}\cdot\frac{E}{LU_0} \tag{7}$$

  Here, different parameters are considered, such as the evaporation rate (E), the width of the substrate (L), the porosity of the deposited film (α), the concentration of solute in solution (c), the density and the molar weight of the solute (ρ, M).

Nevertheless, these regimes are not clearly differentiated, so a transition zone exists. This can be seen at Figure 2-7, that shows the thickness of the film vs the withdrawal speed [28].

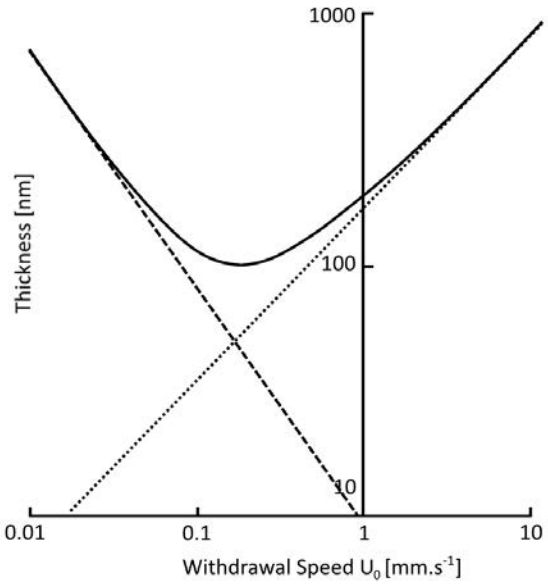

Figure 2-7 Film thickness vs withdrawal speed on a dip coating process [28].

So, the evolution is clearly appreciated, being the left side the Capillary regime and the right side the Drainage regime. In between a transition zone appears, which changes the slope from $h \propto U_0^{-1}$ (Equation 7) to $h \propto U_0^{2/3}$ (Equation 6). Therefore, the minimum thickness can be achieved at some point into this transition region where $\delta h/\delta U_0 = 0$. A scheme of a commercial dip coater is shown in Figure 2-8 [29].

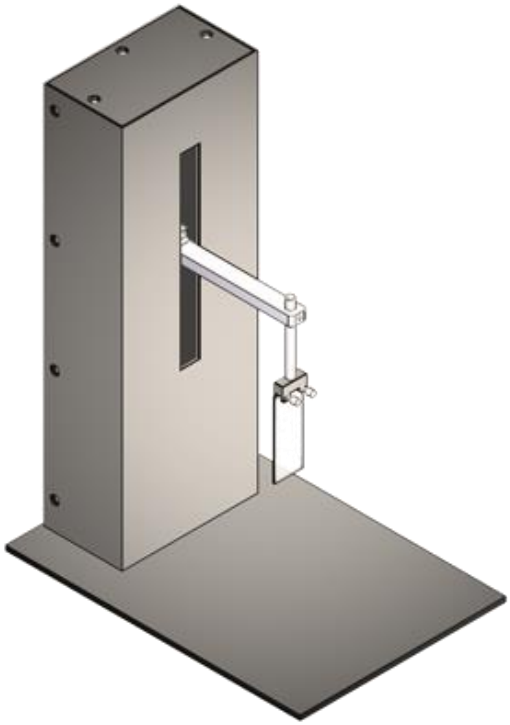

Figure 2-8 Commercial dip coater by Nadetech [29].

2.2.3. Slot-Die coating

In Slot-Die coating technique, the solution is deposited onto the substrate through a moving "head" that delivers a certain amount of solution while moving at a

certain speed. This kind of setup, although is more complex than the previous ones, allows better control of the layer thickness. A schematic illustration of the technique can be found at Figure 2-9 [30].

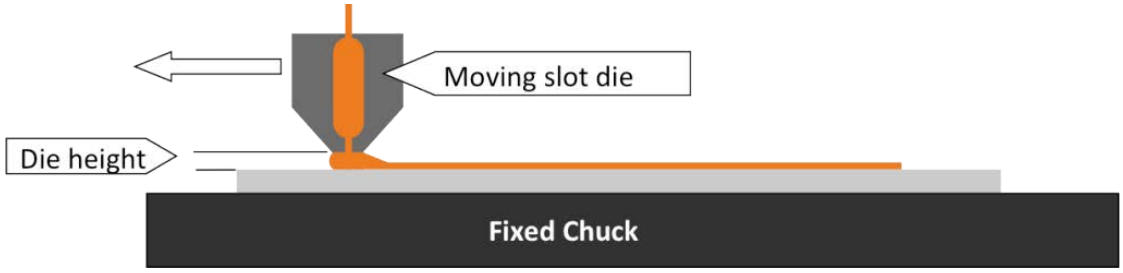

Figure 2-9 Slot-Die coating technique schematic [30].

Several parameters must be controlled very carefully to achieve a homogeneous deposition of a thin film, such as a constant speed of the head over the substrate and a maintained flux of solution over all the wideness of the dispenser. This adjustment will vary depending on the target thickness, the area of the substrate to cover, and the properties of the coating solution.

To be able to determine the liquid pressure profile and check the behavior of each kind of solution, finite element method (FEM) computations can be used, to model complex equations and achieve the right setup profile. This is a very extensive topic, but a first approximation can be found at [31].

Another great advantage of this method is the up-scaling capability. Therefore, a lot of researchers choose this method to check if a certain solution can go from a single substrate deposition to an industrial production. This is particularly useful applied to flexible substrates, in a technique known as roll to roll (R2R) processing, in which a big strip of substrate is rolled around a cylinder in which the slot-die coater head is spreading the solution. Using R2R coating, lengths of several meters can be achieved.

2.2.4. Blade coating (Doctor Blading) / Bar coating

Blade coating or knife coating technique is used to make uniform thin film in a scalable way. It is based on spreading a solution over a substrate moving a metal blade over the substrate at a certain distance. Although this is an easy and scalable technique, it cannot achieve very thin thicknesses, usually nothing smaller than tenths of microns [32]. This method is also not able to produce any kind of texturing in the film, and caution should be taken to avoid any kind of dust contamination during the process, to avoid irregularities during the film deposition.

The last technique is the bar coating; however, it is very similar to the blade coating technique and that is why it belongs to the same section. In this method, a bar covered by a metal spiral is used, instead of a blade. This allows the user to coat all kind of substrates, rigid and flexibles. The disadvantage is that the amount of solution allowed is determined through the gaps between the spiral bar and the substrate. Due to this, neither film structuring, nor a thickness gradient are possible.

2.3. Fabrication and characterization results

Throughout this section, I will explain some experiments done in this thesis going from an initial material research to a fabrication of a complete solar cell device, achieving the inclusion of this kind of devices in a whole electronic system.

In previous sections the importance of perovskite, pros and cons of well-known MAPI have been explained. Lead has a lot of toxicity related problems, although lead-free has a long way to go to achieve the efficiency levels of their lead counterpart. That is the reason why, during my research stay at Jaume I University of Castellón (Spain) I worked on the last ones.

To take out the lead of the perovskite, we must introduce another element in its place [33]. Researchers have tried different elements to fulfill this requirement and gave birth to several configurations using tin, germanium, bismuth, copper, antimony or titanium [34], [35]. Some of these configurations can distort the original perovskite structure to form the so called "double perovskites", that are produced when the lead cation (Pb^{2+}) is substituted with one monovalent (M^{+}) and one trivalent cation (M'^{3+}) to form $AMM'X_6$, instead of the standard ABX_3 [36]. This discovery creates a whole new field of research in which several steps have been taken, mainly in cesium and silver based double perovskites, regarding solar cells [37]–[41], nanocrystals [42] and LEDs [43]. Due to several parameters (time schedule, complexity of the processes, availability of materials in the laboratory, security protocols and training stage) the selected material for this study was the cesium tin-halide perovskite. Although there is also several tin-halide perovskites [44], such as methylammonium or formamidinium, we put the cesium as our target to achieve a full inorganic perovskite, which has been estimated to be less toxic for the human body that its hybrid organic-inorganic counterparts [45]. Furthermore, it has been calculated that a theoretical power conversion efficiency of 25.6% can be achieved in a solar cell using this material [11].

$CsSnI_3$ was shown as a direct band-gap semiconductor material [46], and in the first attempt of doing a Schottky solar cell using $CsSnI_3$, it achieved a PCE of 0.88% [47]. Analyzing this low PCE led scientist to debate its electrical behavior, discussing if it was a semiconductor or a metal. Kanatzidis et al.[48] arrived to the conclusion that, although this perovskite is a semiconductor with a band gap of around 1.3eV, the material is prone to form intrinsic defects related with Sn vacancies [49]–[51]. This generates a huge hole mobility, so the material appears to be metallic.

To compensate these tin vacancies, some studies show that using a tin excess during fabrication can be beneficial, achieving PCE between 2% and 2.76% [52], [53]. But the most important problem to be addressed is that Sn^{2+} ion is not stable in air because it gets oxidized to Sn^{4+}, causing the destruction of $CsSnI_3$. Some approaches have been developed to solve this problem, such as introducing SnF_2 as a reducing agent [54] or mixing it with other ions, such as germanium, to make a passivation layer that avoids the oxidation of tin, forming a double perovskite (Cs_2SnGeI_6) [18]. However, the eye-catching point of this oxidation in the case of $CsSnI_3$, is the transformation into Cs_2SnI_6 which turns to be also a double perovskite.

Surprisingly, this material is quite useful, and has been used previously as a hole transport layer (HTL) on dye sensitized solar cells [55]–[57], nanowires [58] and quantum

rods [59]. It should be mentioned that this material is stable when exposed to air due to the oxidized state of tin [60]. That is the reason why I wanted to explore the evolution process and the optical properties of Cs_2SnI_6. This work generated a publication in ACS Applied Energy Materials [61], and I will go through it during next sections.

2.3.1. Building $MAPbI_3$ solar cells

Once the fabrication techniques have been analyzed, the next step is building a standard perovskite solar cell to apply the theoretical concepts and check its efficiency, in order to check that the necessary fabrication skills have been acquired. So, this section summarizes the building process of a $MAPbI_3$ solar cell. This device can be fabricated in two main architectures: standard and inverted configuration. Both start with the same substrate, but then differ in the deposited layers. The schematic of both structures can be seen at Figure 2-10.

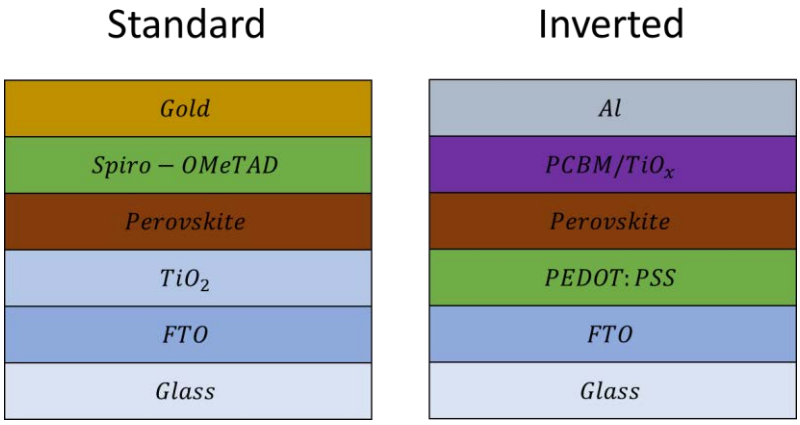

Figure 2-10 Standard and inverted planar architectures examples.

On one hand, the standard architecture starts with the substrate (Glass) with a transparent electrode, called transparent conductive oxide (TCO) because usually these materials are oxides, such as Indium Tin Oxide (ITO) or Fluorine doped Tin Oxide (FTO), with a very high transmittance to let the light pass through them. After that, an Electron Transport Layer (ETL) is deposited. This layer is responsible of the electron extraction and hole blocking, to avoid the recombination of the carriers (TiO_2, SnO_2, ZnO, SiO_2, ZrO_2, PCBM) [62]. Now, the active layer appears, that is the responsible of the conversion between light and electricity due to the photoelectric effect (perovskite). Then, the Hole Transport Layer (HTL) is deposited. This layer has the exact opposite function that ETL. In this case it allows the flow of holes, blocking the electrons. Several materials have been studied as HTL, such as organic molecules (P3HT, PTAA, PEDOT:PSS, Spiro-OMeTAD) and inorganic (CuI, Cu_2O, CuO, CuSCN) just to cite a few [63]. Finally, another electrode is deposited. Usually, this electrode is made of metal (Au, Ag, Al, Pt), due to the high conductivity and the high reflectance of light, to redirect it back to the active layer.

On the other hand, the inverted architecture is produced when we invert the standard process (Figure 2-10). This means that the process starts with the same substrate (Glass) and then a TCO. But now the HTL is deposited, then the active layer and then the ETL, ending with also a metallic electrode. Deciding an architecture is a

fundamental step because it will determine the fabrication process and the material that would be used.

In this work, a standard architecture was developed, following the next steps:

1. Preparation and cleaning of the substrate: FTO-coated glass substrates are cleaned with distilled water and soap (Extran®) using an ultrasonic cleaner. Then, they are rinsed with MilliQ® water (ultrapure) and ultrasonicated again in a bath of Ethanol and Isopropanol (1:1 ratio). Finally, they are dried using a nitrogen gun and stored.
2. FTO Etching: Taking advantage of the already coated glass, the FTO is etched in convenience according to the electrode design. Adhesive tape is used to protect the electrode at the interest zone. The remaining part is etched using zinc powders and applying hydrochloric acid (HCl) 2M over the surface. The chemical reaction will produce bubbles. Then, the substrate is cleaned through a cycle of ultrasonic baths, using distilled water with soap, isopropanol and ethanol, and finally acetone and ethanol. Each bath takes around 15 minutes.
3. ETL deposition: Tin oxide (SnO_2) is used as ETL. Tin oxide solution (2.5% weight) is spin coated at 3000 rpm over the substrate. Immediately, the sample is annealed in a hotplate at 150°C for 30 minutes and then cooled down under standard atmosphere. It is worth mentioning that, previously to the deposition, the substrates are exposed to a UV-Cleaning process for 15 minutes minimum. This process not only clean the surface, but also helps improving the adhesion of the SnO_2 layer [64].
4. Perovskite deposition: Here, $MAPbI_3$ is selected as an active layer. To avoid oxidation of the solutions, the following depositions are done inside a glovebox with nitrogen atmosphere. The MAPI solution is prepared inside the glovebox mixing its precursors, MAI and PbI_2 (1:1 molar ratio) into dimethyl sulfoxide (DMSO) solvent. This solution is spin coated over the sample with a certain speed profile for 40 seconds. While the substrate is still spinning, ethyl acetate is dropped to act as an antisolvent, helping the crystallization process of the perovskite [65]. Just after the spin coating, the samples are annealed at 130°C for 10 minutes. During this process, the layer will go from a yellowish color to a darker brown, almost black, proving that the crystallization is correct, and the perovskite crystal is formed.
5. HTL deposition: Spiro-OMeTAD is used as HTL. The solution is formed of Spiro-OMeTAD solved in chlorobenzene, and doped with lithium bis(trifluoromethylsulfonyl)-imide (LiTFSI) and tert-butyl pyridine (TBP) to improve its electrical conductivity and hole mobility [66]. This doped solution is spin coated over the perovskite layer at 4000rpm for 30 seconds. The samples are taken out of the glovebox and left under a standard atmosphere inside an aluminum foil wrapped box to start their oxidation process. This oxidation is crucial to exploit the doping properties of the HTL [67].
6. Metal electrode deposition: Last step is the deposition of the other electrode (pure gold in this case). This deposition is done using a thermal evaporator (the same that was used in section 2.3.1 during $CsSnI_3$ co-evaporation) with a mask, that has the right pattern in which gold should be deposited. The thickness of the gold electrode layer is 100 nm.

Figure 2-11 shows one of the final devices and its characteristic J-V curve (this and other device characterization techniques will be explained in detail along the next chapter). The best device fabricated in this work reached a PCE of 16.9%.

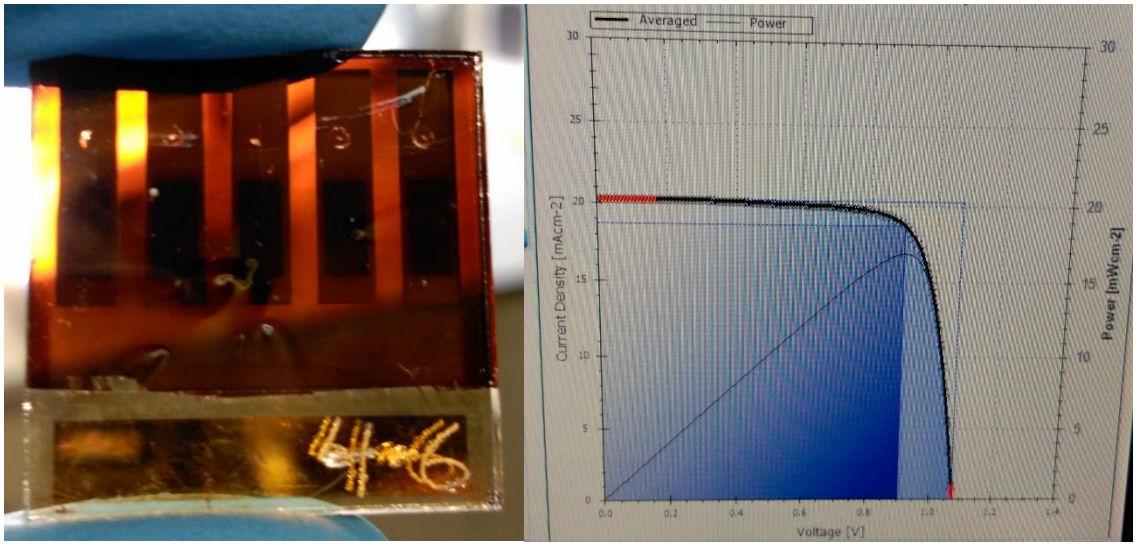

Figure 2-11 Photograph of a $MAPbI_3$ solar cell (Left) and its J-V curve, giving an efficiency of 16.9% (Right).

2.3.2. Developing a lead-free, tin-halide perovskite

Now that we have determined the material that we are looking for, several approaches can be taken. During this work three different fabrication approaches were tried, and all of them will be explained (Figure 2-12). However, it will be seen that only one approach gave successful results.

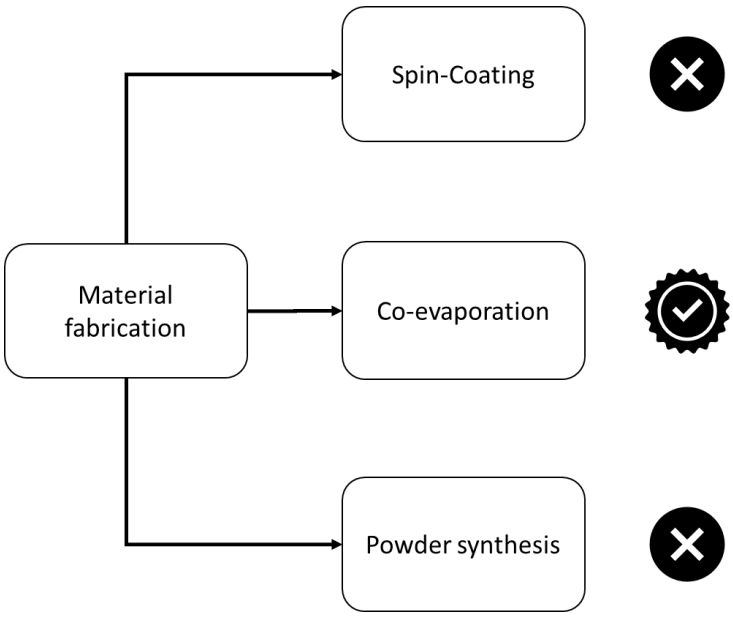

Figure 2-12 Material fabrication approaches. Only co-evaporation gave successful results.

2.3.2.1. Spin-coating

The easiest one is trying to deposit this material using spin-coating. To do that we need a $CsSnI_3$ solution, that is obtained through its precursors, cesium iodide (CsI)

and tin iodide (SnI_2). The solvent selected was dimethylformamide (DMF) [60]. The proposed reaction is shown in Equation 8.

$$CsI + SnI_2 \rightarrow CsSnI_3 \quad (8)$$

Knowing the molecular weight of both substances, 26mg of CsI were diluted on 1mL of DMF, obtaining a yellowish solution. After that, 37.3mg of SnI_2 were added, to form a brownish solution. Now, 100µL of this solution were spin coated over a FTO (Fluorine-doped Tin Oxide) coated glass substrate. The substrate was spinning at 4000 revolution per minute (rpm) during 30s and the deposition was made statically. After that, the samples were annealed at 150°C over 30 minutes, to allow the formation of the crystal. Unfortunately, although the samples had a brownish color, they were almost transparent, demonstrating very low optical absorption. So, our guessings were whether the crystal was not well formed, or the layer was too thin. It is important to mention that this deposition was made on a spin coater set up inside a glove box (nitrogen atmosphere), so an oxidation process could not occur (see Figure 2-13 left).

2.3.2.2. Co-evaporation

Apart from the classical spìn-coating technique, other deposition methods have been developed, such as a hybrid spin coating followed by annealing in vapor [68], or an alternative evaporation process with a reconstruction annealing under iodine vapor too [69]. Alternatively, in this work, we made a co-evaporation process in an evaporator chamber to form thin films in a controlled way, with a good crystal growth. The process was carried out into a MBraun thermal evaporator, also placed inside of a glovebox to avoid an undesired reaction with the standard atmosphere (see Figure 2-13 right).

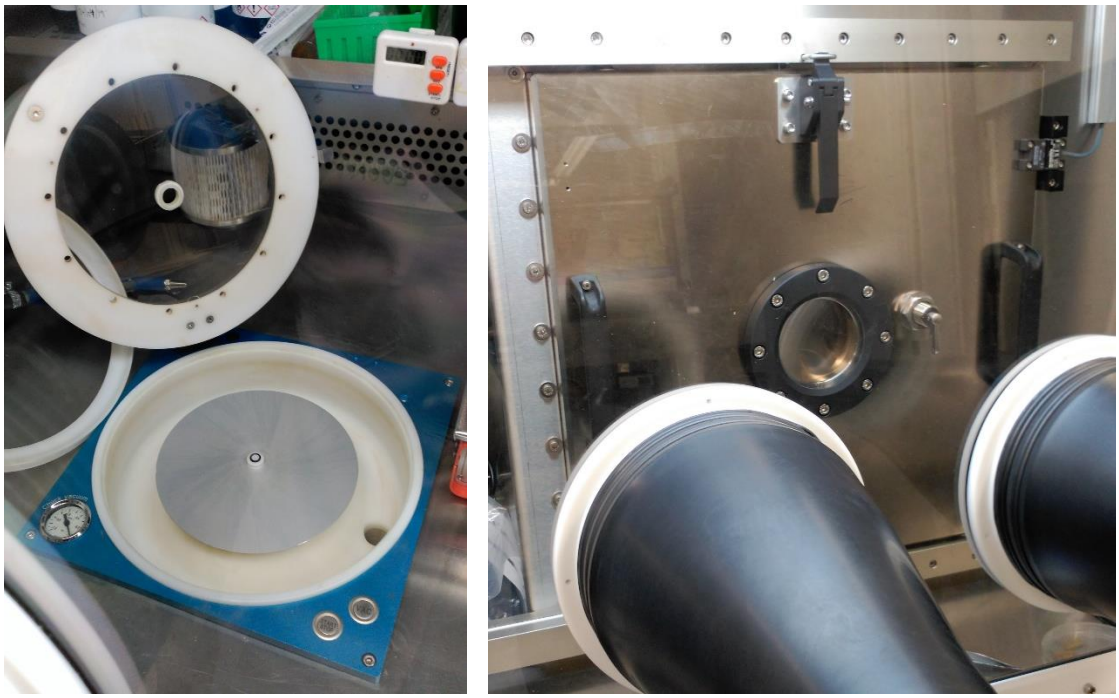

Figure 2-13 Spin coater (left) and thermal evaporator (right) embedded into a glovebox to avoid oxidation processes during depositions.

Producing a thin film using a thermal evaporator is a totally different process than doing it with a spin coater, so, targeting the same chemical reaction (Equation 8), the parameters that we must consider now are the final thickness that we want to achieve and the evaporation rate of each compound. Another important parameter is the ratio between the evaporation rate of both components because this ratio will give us the correct stoichiometry. This can be calculated using the molecular weight and density of each compound, to get the deposited volume (mL), and then relate it with the deposition rate (Å/s) using the deposition area and the time (Equation 9 and 10):

$$(CsI) \rightarrow 1\ mol = 259.81g\ = 57.61mL\ = rate_{CsI}[\text{Å}/s] \cdot Area \cdot t \quad (9)$$

$$(SnI_2) \rightarrow 1\ mol = 372.52g = 49\ mL = rate_{SnI_2}[\text{Å}/s] \cdot Area \cdot t \quad (10)$$

Making the ratio of these two volumes we can obtain the ratio between the deposition rates (Equation 11)

$$\frac{57.61\ mL\ CsI}{49\ mL\ SnI_2} = \frac{rate_{CsI}}{rate_{SnI_2}} = 1.176 \quad (11)$$

So, to achieve the 1:1 molar ratio, the deposition rate of CsI should be 1.176 higher than the deposition rate of SnI_2. Now, the only thing to calculate before starting the process is the deposition rate of SnI_2. This can be an arbitrary value. Of course, the higher the deposition rate, the higher the impurities that can be formed. Moreover, the maximum deposition rate will depend on the temperatures achievable on the crucibles of the evaporator.

Therefore, as we had no previous information, we did an evaporation test of each compound, just putting the desired elements into the crucibles and raising the temperature until the system started measuring a deposition rate. This gave us the evaporation temperature of each element. In this case we got temperatures of around 460°C in CsI and around 260°C in SnI_2. These temperatures were obtained when the evaporator was at $4x10^{-6}$ mbar approximately. Figure 2-14 shows an image of the display that monitors the temperatures of each source and the pressure of the chamber.

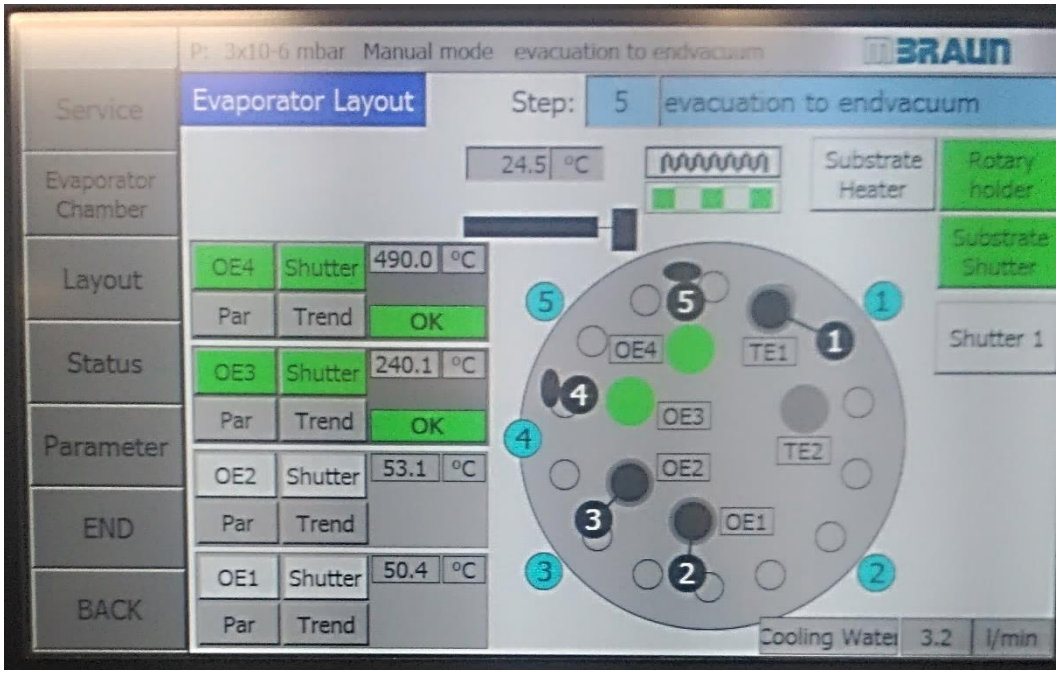

Figure 2-14 MBraun evaporator monitor, showing temperatures of CsI source, SnI_2 source, and pressure of the chamber.

Also, the time taken to deposit the layer is important, and can be calculated using Equation 12 (e.g., 100nm of final thickness as our goal, with a SnI_2 deposition rate of 0.33Å/s):

$$rate_{CsI} \cdot t + rate_{SnI_2} \cdot t = h_{layer} \tag{12}$$

Putting (11) into (12) and solving for time, we obtain (13):

$$t = \frac{h_{layer}}{2.176 rate_{SnI_2}} = 1408.45s \approx 40min \tag{13}$$

So, the evaporator will take around 40 min to deposit a 100nm layer of $CsSnI_3$ at that deposition rates (it should be added to this time the vacuum and refill processes of the chamber, thus, the full process can take up to 2 hours). These are theoretical approximations, but in the next section it is shown how to characterize these films to achieve an optimal result. Figure 2-15 shows a picture of the produced films.

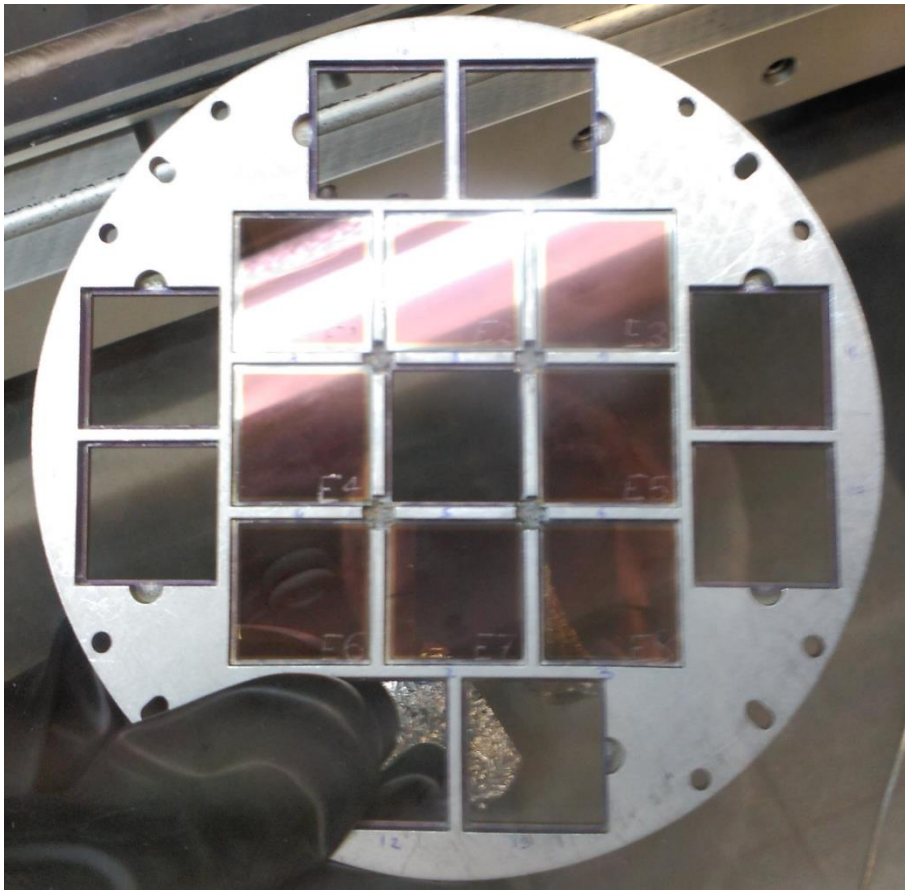

Figure 2-15 First attempt of CsSnI3 Co-evaporation samples.

During the work, the evaporation process was done several times to produce different samples, but all of them followed the same calculations. The final optimized recipe included an excess of SnI_2, that helped the material to cover tin and iodine vacancies [69]. This was achieved making equal the deposition rates of the compounds, making the reverse calculation of Equation 11. This gives as a result the Equation 14.

$$\frac{rate_{CsI}}{rate_{SnI_2}} = 1 = \frac{1mL}{1mL} \rightarrow \frac{17.36mmol}{20.40mmol} = \frac{1}{1.176} \qquad (14)$$

Therefore, instead of having a molar ratio of 1:1, now we have a ratio of 1:1.176, that implies an excess of SnI_2. The deposition controller during the process can be seen at Figure 2-16.

Figure 2-16 Deposition co-evaporation controller showing almost 1:1 deposition rates of CsI and SnI_2.

Films with tin iodide excess can be seen at Figure 2-17. The films have a very deep black color that means great light absorption properties. Also, the films appeared to be very homogeneous along the substrate surface in every sample. This high coverage is one of the main advantages when using thermal evaporation process.

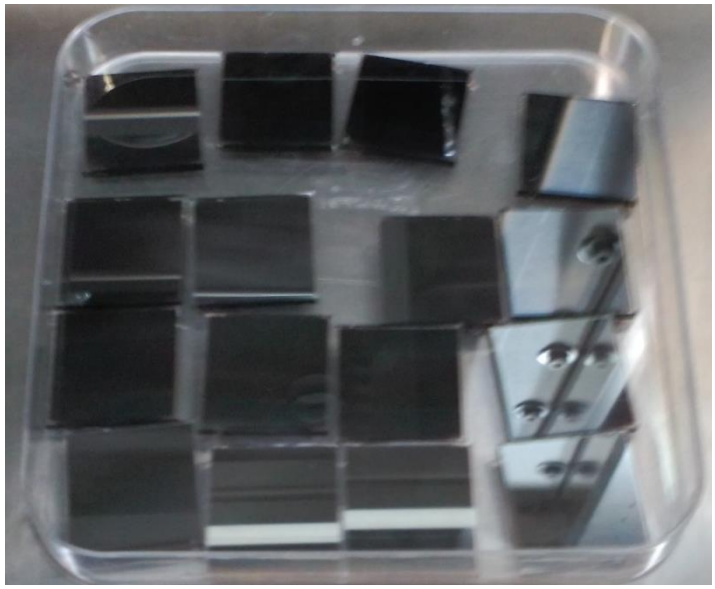

Figure 2-17 $CsSnI_3$ films with SnI_2 excess after the co-evaporation process. Black color shows the quality of the film.

Storing the $CsSnI_3$ films under nitrogen atmosphere prevents their degradation, but as soon as we took them out of it, the decomposition process began. The result of

this whole decomposition process produced by the environmental conditions and the consequent tin oxidation is shown at Figure 2-18.

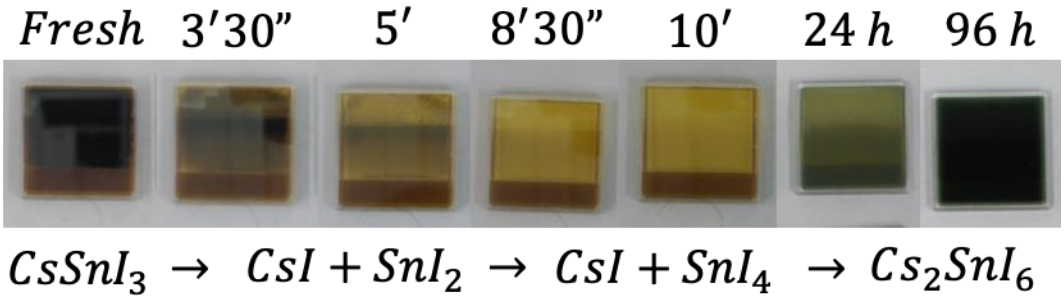

Figure 2-18 Transformation of the thin film: From $CsSnI_3$ (left) to total decomposition (center) to the reconstruction as Cs_2SnI_6 (right).

One remarkable feature obtained from this figure is that the sample degradation is slower in the bottom line. Interestingly, this is the zone where the FTO is exposed in the substrate. That led us to the guessing that the fluorine inside the FTO acts as a reducing agent, blocking the tin oxidation. This behavior of fluorine has been demonstrated previously when SnF_2 was added during the fabrication process of $CsSnI_3$ [54].

2.3.2.3. Powder synthesis

In parallel with the thin film fabrication procedure, we also tried to synthesize Cs_2SnI_6 as powder to test its evaporation capabilities. To do so, we followed the next procedure: A vial with 1mmol of CsI (259.81mg) and 1mmol of SnI_2 (372.52mg) was prepared. Then, 1mL of acetone was added, and all the solution was stirred at 750 rpm for 2 hours, to totally disperse the precursors (Figure 2-19 left).

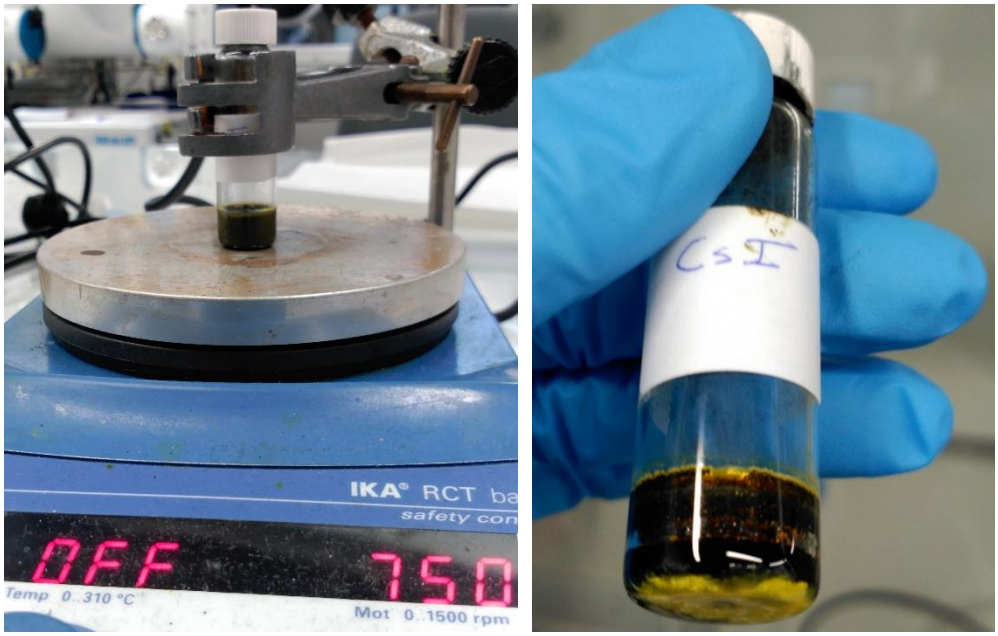

Figure 2-19 Black solution (left) containing 1mmol of CsI and 1mmol of SnI_2 in 1mL of acetone. Same vial after acetone evaporation (right).

After that time, the lid was left open to allow the evaporation of the acetone, and the leftover was a black and yellow powder (which can match a black and yellow phase of this perovskite, see Figure 2-19 right). To completely dry the powders, the vial was placed onto a hotplate at 100°C for around 40 minutes (this can also allow the conversion from a yellow phase into a black phase) [48]. At that time, only black powder remained into the vial (see Figure 2-20). All this process was done on standard atmosphere to allow the oxidation and evolution of the material from $CsSnI_3$ into Cs_2SnI_6.

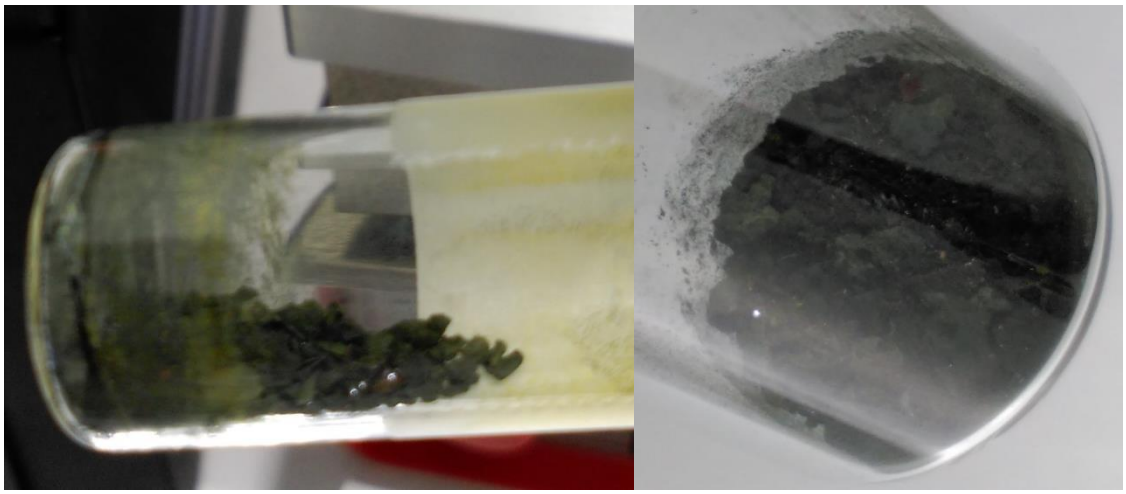

Figure 2-20 Black powder after the synthesis process and drying (Cs_2SnI_6).

In the next section we will identify this powder using X-Ray Diffraction (XRD) analysis, checking that it is pure Cs_2SnI_6. Unfortunately, we also discovered that, in this state, the material is not suitable for making thin films using the evaporator, because it suffers from thermal decomposition before arriving to the evaporation point.

2.3.3. Characterization of material properties

Starting with the thin films and the powders synthesized in the last section, I will go through all the characterization methods and steps that we followed. Moreover, I will explain the conclusions extracted in each characterization step. To ease the readiness, this section will be divided in subsections, one per characterization technique. A general view of all the characterizations applied and the expected result from each one is given at Figure 2-21.

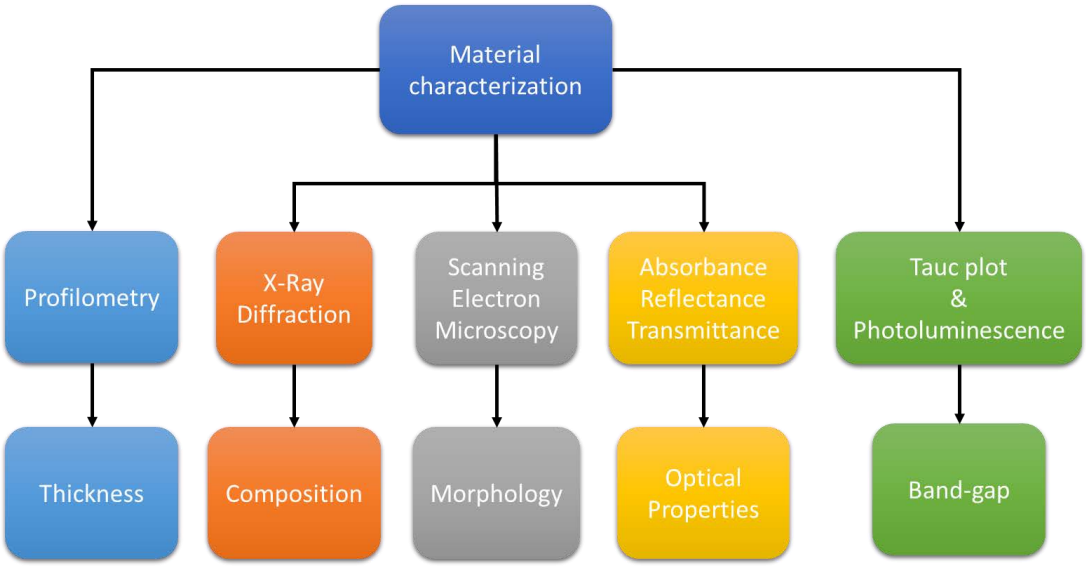

Figure 2-21 Material characterization flowchart including the expected results from each test.

After this material characterization I tried to develop a solar cell using Cs_2SnI_6 as an active layer, maintaining a typical layer structure used for another perovskite solar cell such as MAPI. Several configurations were built, such as Glass/FTO/SnO_2/Cs_2SnI_6/P3HT/Au or Glass/FTO/SnO_2/Cs_2SnI_6/Spiro-OMeTAD/Au. Unfortunately, both of them gave a short-circuit behavior, probably due to the highly doped p-type material (Cs_2SnI_6) that has almost metallic response [48]. To take advantage of this fact, this lead-free perovskite was used as a hole transport layer (HTL) too. In this case the structure used was Glass/FTO/SnO_2/MAPI/Cs_2SnI_6/Au. Here, we obtained some results that oscillated between 1% and 5% PCE, very unstable.

2.3.3.1. Profilometry

This technique is very useful when we want a fast way to measure the thickness of a thin film and it was used to measure the thickness of the films produced by the evaporator.

The system is formed by a very small lever with a pointy tip that goes over the film applying a constant force. When some bump or trench is reached, the system can calculate the depth or the height of that irregularity. So, the material is deposited over glass, and then it is scratched, removing the layer at that zone. When the profilometer reaches that zone, it can see the height difference between the top of the thin film and top of the glass, which is equivalent to the film thickness.

This was a crucial step, because it allowed the calibration of the evaporator, to correct the deposition rate and the estimated thickness. In Table 2-2, the relation between profilometer measurements and evaporator estimations after each calibration can be seen. Here, the profilometer took 3 measures per sample and then they were averaged and compared to the evaporator estimated thickness.

Calibration	1st measure	2nd measure	3rd measure	Mean	Evaporator estimation
First	49.2 nm	53.9 nm	43.6 nm	48.9 nm	100 nm
Second	39.0 nm	44.5 nm	41.2 nm	41.6 nm	29 nm
Third	242.9 nm	225.4 nm	219.4 nm	229.2 nm	205.0 nm

Table 2-2 - Calibration of evaporator using the tooling factor and profilometry.

To calibrate the evaporator, the so called "tooling factor" was changed. Equation 15 shows how to calculate this tooling factor:

$$Tooling\ factor = \frac{h_{measured}}{h_{estimated}} \cdot 100[\%] \tag{15}$$

At first test, the error was higher than 50%, but after two corrections of the tooling factor, the error was only around 10%. It is important to mention the resolution of the profilometer (in our case 1 Å), to estimate the measurement error.

The equipment used for these measurements was the Veeco Dektak M6 Profilometer.

2.3.3.2. X-Ray Diffraction

When we want to check if our compound is properly formed, the X-Ray Diffraction is a very useful technique. This technique analyzes the diffraction pattern generated by the structure of a crystal when it is illuminated with light. The foundation of this is Bragg's Law (Equation 16)

$$n\lambda = 2dsin\theta \tag{16}$$

being n the diffraction order, λ the wavelength, θ the diffraction angle and *d* the distance between the atomic planes of the crystal. However, the diffraction can only occur when the incident wavelength is in the same order of magnitude as the interplanar spacing, which is of a few angstroms. That is the reason why X-Rays must be used [70].

An X-Ray Diffractometer is composed by three parts: an X-Ray tube (source), a sample holder and an X-Ray detector. There are several types of sources (Cu, Fe, Mo, Cr, Ag), and each one will generate a certain wavelength. In this work, the source was based on copper, and its associated wavelength was 1.5418 Å.

So, for an unknown crystal we can record the X-Ray diffraction pattern and then compare it to the diffraction pattern of a known material. Because the d-spacing of each material is different, we can identify our material in an unequivocal way. The reference data for Cs_2SnI_6 was obtained from the American Mineralogist Crystal Structure Database (AMCSD) [71]. Figure 2-22 shows the X-Ray diffraction pattern of our sample powder and of a thin film exposed to standard atmosphere during 5 and 8 days.

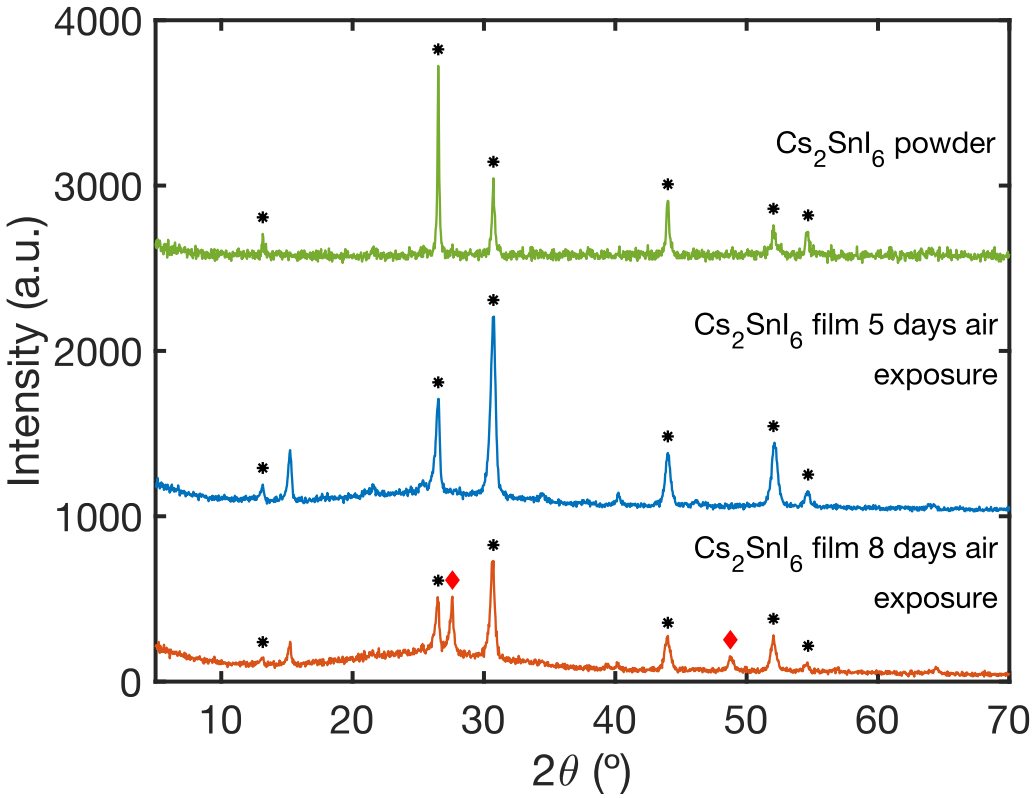

Figure 2-22 X-Ray Diffraction patterns of black powder (top) and thin films after 5 (middle) and 8 (bottom) days of air exposure. The material should be Cs_2SnI_6.

The diffraction pattern of powder has 6 well-defined peaks, corresponding to the next 2θ values: 13.16°, 26.52°, 30.72°, 44.04°, 52.08° and 54.68°. Checking the most powerful peaks of the Cs_2SnI_6 pattern [72], they are localized at 13.19°, 26.55°, 30.75°, 44.05°, 52.17° and 54.68° (black dots in the graph). Therefore, we have a perfect match in the crystal structure, thus the proof that we synthesized pure Cs_2SnI_6 successfully.

Same peaks with different relative intensities (due to different growth of the crystal) appear on the thin film exposed to air for 5 days, that proves the stability of this material. After 8 days of exposure, other peaks start appearing (red diamonds), mainly at 27.6° and 48.76°. If we search for those peaks into AMCSD [73] we can found that cesium iodide (CsI) shows its maximum peaks at 27.62° and 48.85°, obtaining a perfect match with our results.

So, we can conclude from the X-Ray Diffraction Analysis that either the powder direct synthesis or the co-evaporation thin film deposition ($CsSnI_3$) with an ulterior oxidation and reconstruction process, are both generating a perfect Cs_2SnI_6 material. Furthermore, a thin film of this material is stable on air during a week. Then a decomposition of the material can be appreciated due to the appearing of CsI crystals.

All the XRD measurements of this work were done used a Bruker D8 Advance diffractometer [74].

2.3.3.3. Scanning Electron Microscopy (SEM)

To check the morphology, surface, and thickness of the created film, we need an instrument capable of taking images with nanometric resolution. That is why we used Scanning Electron Microscopy (SEM). SEM relies on the same principle that the classical optical microscopy does, the main difference is the excitation source. In optical microscopy we use visible light (white) with a mean wavelength of 550nm. This wavelength is limiting the amplification capability and that is why the highest amplification in optical microscopy is around x1000. SEM uses electrons instead of visible light, which have shorter wavelengths, thus increasing the maximum amplification achievable. Figure 2-23 shows a schematic version of an scanning electron microscope [75].

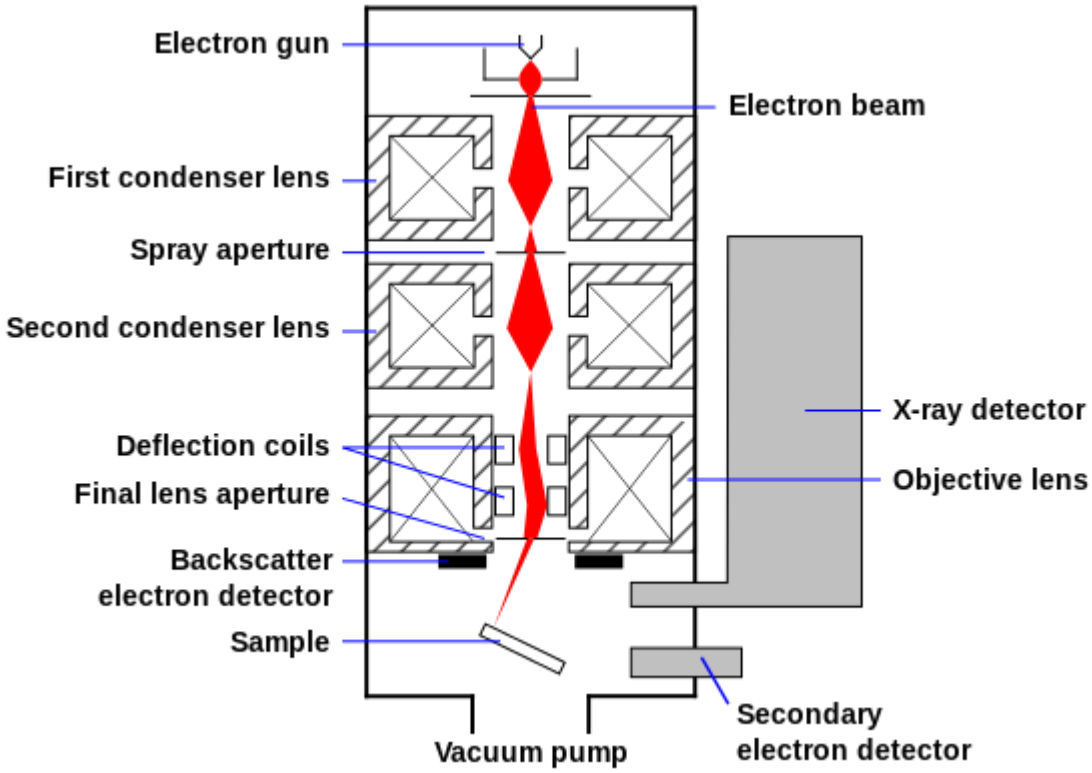

Figure 2-23 Schematic of an scanning electron microscope (SEM) obtained from [75].

So, in a very simplified way, the scanning electron microscope is composed by an electron gun (that generates the electron beam), a series of electromagnetic lenses to focus the beam, a sample holder and several detectors (for secondary and backscatter electrons, and X-Rays that can be generated during the process). All these elements are placed inside a chamber that should be in vacuum to function properly. Moreover, the sample should be conductive to avoid the accumulation of electrons in its surface, otherwise a wrong image is produced. That is why, when the sample is not conductive, receives a pre-treatment in which is covered with a very thin layer of a conductive material (e.g., gold, palladium, platinum, or graphite) to relief the electrons accumulation. In these measurements the thin films were coated with platinum and the powders were laying onto conductive graphite tape.

Regarding the images, there are basically two capture modes. One of them counts the secondary electrons that are produced at depths of few nanometers, so it is

useful to observe the morphology of the surface of the film. The other one counts the backscattered electrons, which come from a deeper place, thus useful for knowing the composition of the material (also considering the X-Rays generated by the sample).

The scanning electron microscope used in this section was JSM-7001F from JEOL [76]. Figure 2-24 shows the most representative SEM pictures obtained. There, we can see the powder, composed by cubic crystals (as expected from Cs_2SnI_6). At (b) the surface of the film can be appreciated. It is observed that is irregular, with some holes. We guess that this is due to the degradation and reconstruction process (remember that the film that we originally developed was $CsSnI_3$ that suffered natural oxidation and reconversion process). Finally, at (c) and (d) the degradation of the material is shown. After 11 days exposed to ambient conditions, small crystals appeared onto the surface.

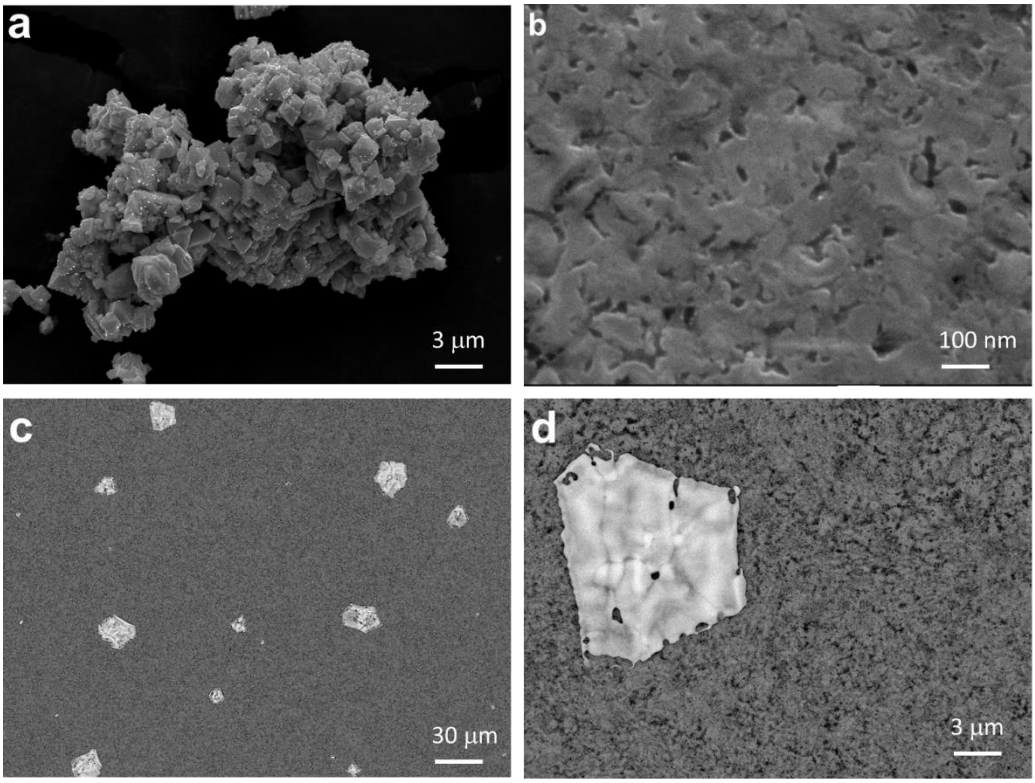

Figure 2-24 Scanning Electron Microscopy (SEM) images of (a) Cs_2SnI_6 pure powder and (b) thin film. (c) Same image after 11 days of air exposure: CsI crystals appear. (d) Detailed picture of a CsI crystal.

To check that our assumptions were correct, we used a capability of the SEM called Energy-Dispersive X-Ray Spectroscopy (EDS). The working principle of this technique is similar to XRD explained previously, but here the excitation source is the electron beam itself. With this technique we analyzed the composition of the Cs_2SnI_6 powder (Figure 2-25a) and the crystals that appeared during degradation (Figure 2-25b).

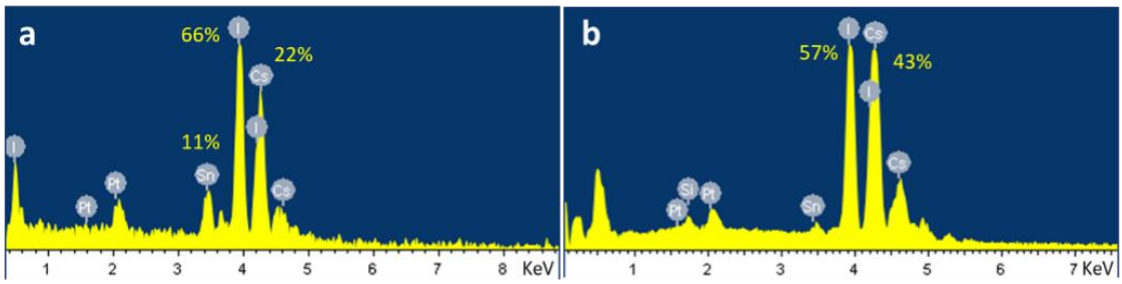

Figure 2-25 Energy-Dispersive X-Ray Spectroscopy Analysis of (a) Cs_2SnI_6 powders and (b) crystals appeared during degradation (CsI).

Looking at EDS results, we could confirm that the powders were made of Cs_2SnI_6 (weighted composition of Cs=22%, Sn=11% and I=66%). Furthermore, we confirmed that the white crystals that appeared during degradation were in fact CsI (weighted composition of Cs=43%, I=57%), showing the decomposition of the perovskite.

As a final double-check and to fully exploit the functionalities of SEM, we also made a cross-section scan to inspect the thickness of the developed film, and the deviation between evaporator estimation, profilometer and SEM. Figure 2-26 shows this scan.

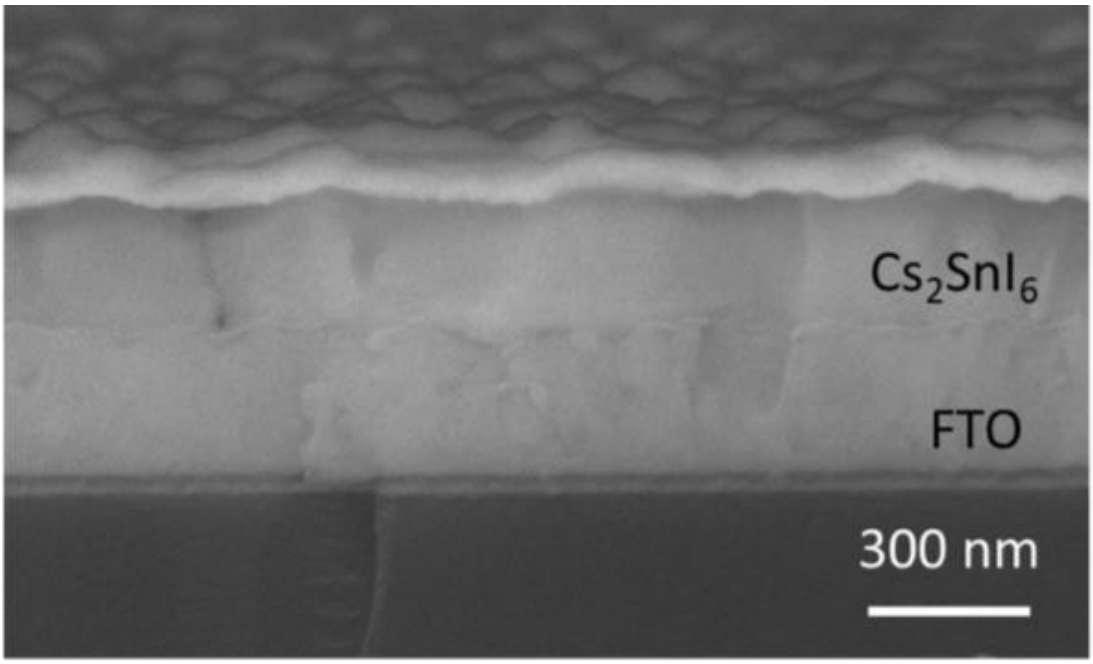

Figure 2-26 SEM Cross-section of Cs_2SnI_6 thin-film on FTO-covered glass substrate.

Here, we can see 3 main layers related from bottom to top to Glass, FTO and perovskite (Cs_2SnI_6). The measurement of the perovskite layer thickness using SEM gave us a value around 230nm, which matches perfectly with the mean value obtained from the profilometer and deviated from the value expected from the evaporator.

2.3.3.4. Absorbance, Reflectance and Transmittance

Now that we have confirmed size, shape, and composition of our material, we should study its optical properties. One on the easiest measurements that can be done is UV-Vis Spectroscopy. In this technique, the intensity of light passing through the

sample (I) is measured and compared with the intensity of light going through a known reference (I_0). The ratio between both values (I/I_0) is known as Transmittance. Of course, this ratio should be analyzed in each wavelength of interest, and that is why the spectrophotometer is composed by a light source and a monochromator, apart from the photodetector. A schematic view of transmittance and reflectance measurements can be seen at Figure 2-27.

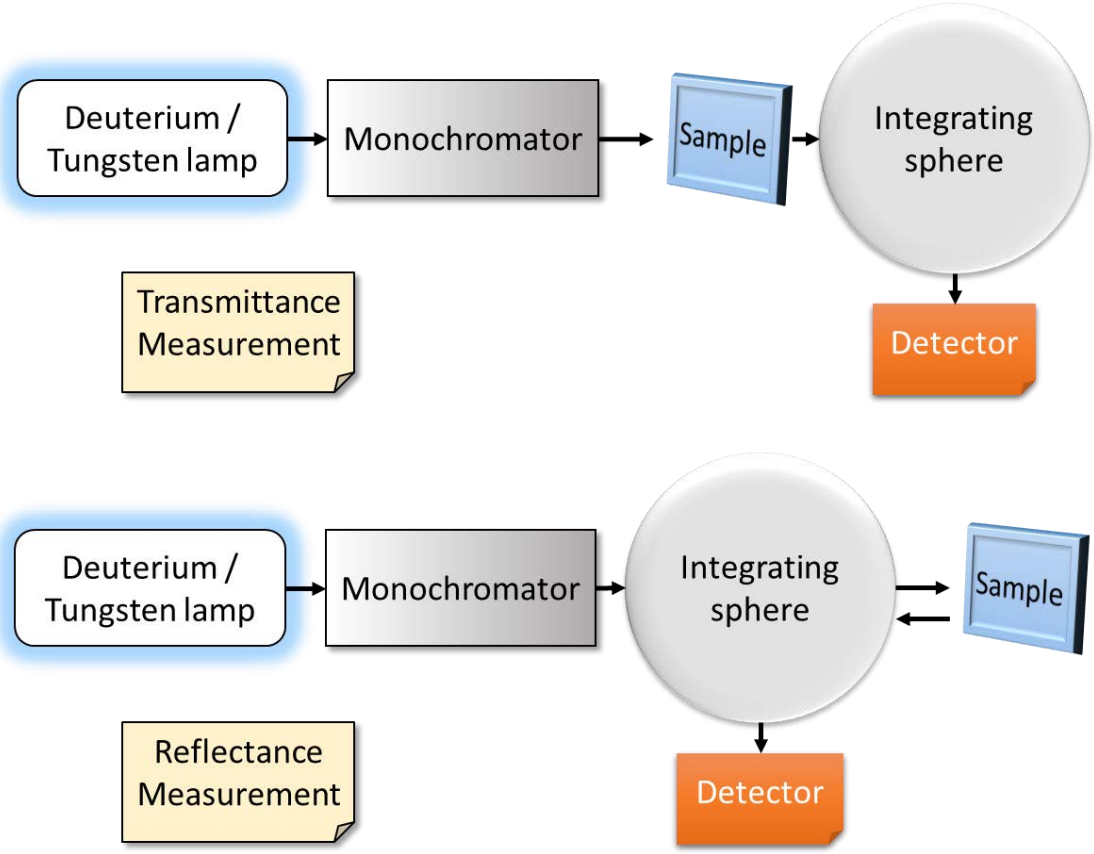

Figure 2-27 Schematic view of Transmittance and Reflectance measurements using a UV-Vis double spectrophotometer with integrating sphere.

Transmittance and reflectance of the film were acquired using this system, and then the absorptance was calculated according to Equation 17:

$$A + T + R = 1 \tag{17}$$

This equation simply means that the normalized impinging light should be equal to the sum of the reflected light (R), the transmitted light (T) and the absorbed light (A). Thus, usually a term referred to the scattered light (S) is added, here the scattering term is included in both transmittance and reflectance measurements, due to the use of an integrating sphere.

Figure 2-28 shows these three components plotted against a spectral range between 350 nm and 850 nm.

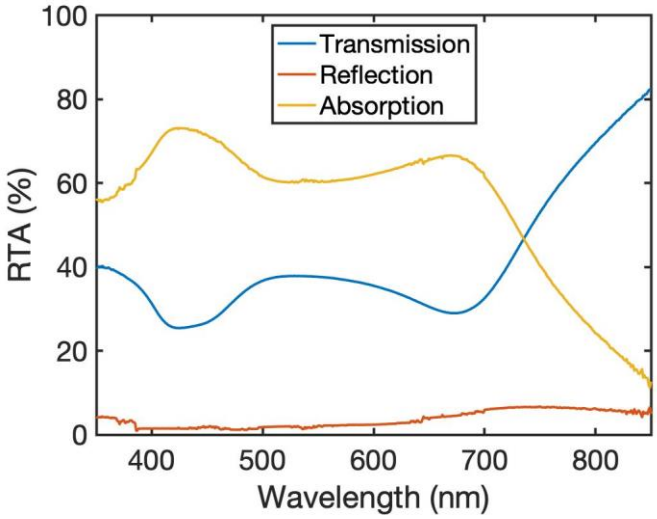

Figure 2-28 RTA plot of a Cs2SnI6 thin film (230nm).

This Transmittance is given in percent units, and it is easily convertible into Absorbance (this **is not the same** that Absorptance) using Equation 18:

$$\mathcal{A} = -\log(T) \tag{18}$$

This Absorbance has no units itself, so usually it is given in absorbance units (a.u.). This value is useful to compare the amount of light that is being absorbed by the sample. Using these data, another material parameter can be calculated, the absorption coefficient, using Equation 19 [77]:

$$\alpha = \frac{1}{t}\ln\left[\frac{(1-R)^2}{T}\right] \approx 2.303\frac{\mathcal{A}}{t} \tag{19}$$

Here, α is the absorption coefficient, t is the thickness of the film, R is the reflectance, T is the transmittance and $\mathcal{A}$ is the absorbance. It is worth mentioning that the final approximation (sometimes found in the literature without context) is only true when the reflectance is very low (close to 0).

Figure 2-29 (left) shows the calculated values for the absorption coefficient of a fresh $CsSnI_3$ sample and the degradation suffered in only 10 minutes exposed to the air. Four days after, the reconstruction was fully completed (right). The purple line represents the new Cs_2SnI_6, which fully reproduces the absorption levels that its antecessor had between 700 nm and 800 nm. Remarkable fact here is that the original $CsSnI_3$ had an absorption coefficient very dependent on wavelength (e.g., much stronger in blue than in red). Surprisingly, after reconversion into Cs_2SnI_6, it can be checked that the absorption coefficient is much more independent on the wavelength. This could be an interesting property in semitransparent windows applications [78]. In fact, this sample had an average visible transmittance (AVT) of 42.1%, doubling the value of the AVT reported for 150nm MAPI films[79], [80]. So, in this case, we can have high transmittance values without sacrificing the layer thickness (230nm), thus, avoiding problems related with the eventual physical contact between the layers deposited above and below perovskite, leading to short-circuit behavior.

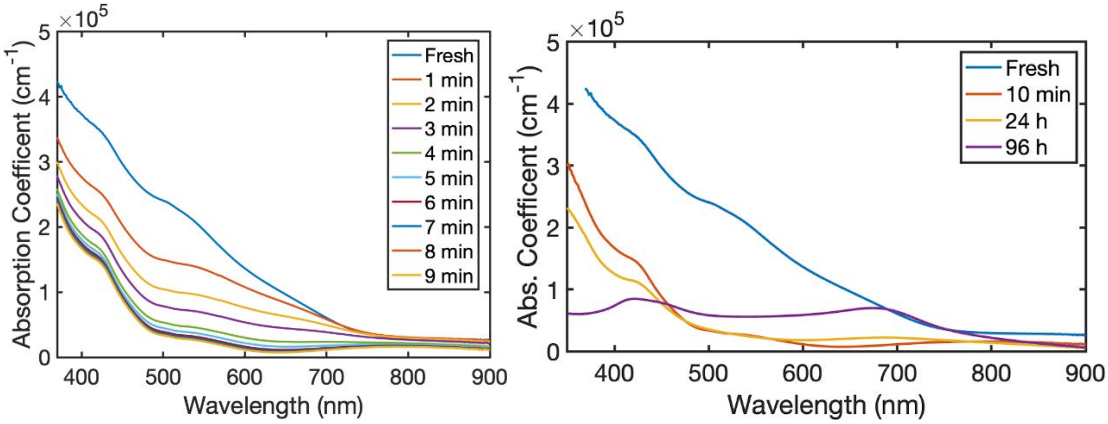

Figure 2-29 Absorption coefficient evolution in a $CsSnI_3$ co-evaporated film for 1 to 10 min (Left) and up to 96 hours (Right).

Moreover, with the measurements taken in this section we can also estimate the refractive index of Cs_2SnI_6 along this spectral interval. The refractive index of a material is of crucial importance in an optical study because it will determine the behavior of light crossing it. The complex refractive index is composed by the real (n) and the imaginary (k) parts. Both parts can be computed using the following equations [77].

$$k = \frac{\alpha\lambda}{4\pi} \tag{20}$$

$$R = \frac{(n-1)^2+k^2}{(n+1)^2+k^2} \rightarrow n = \frac{1+R}{1-R} \pm \frac{\sqrt{(1+R)^2-(1-R)^2(1+k^2)}}{1-R} \tag{21}$$

In first place, the imaginary part (also called extinction coefficient) is calculated following Equation 20 and it is directly related with the absorption coefficient. It is remarkable that two absorption peaks are found, one around 450nm and the other near 700nm.

With k and reflectance values, the real part (n) of the refractive index can be calculated using Equation 21. The results of n and k respect to the wavelength are plotted in Figure 2-30:

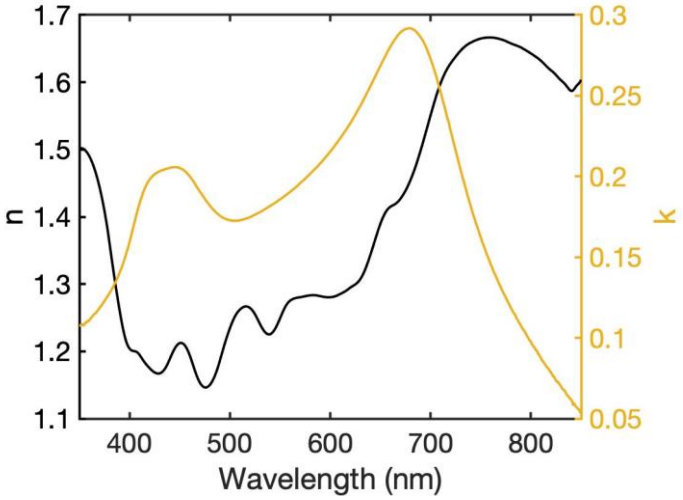

Figure 2-30 Real (n) and imaginary (k) parts of the Cs_2SnI_6 computed refractive index.

Reflection, transmission, and absorption measurements were taken using Cary 300 UV-Vis spectrophotometer from Agilent (Figure 2-31).

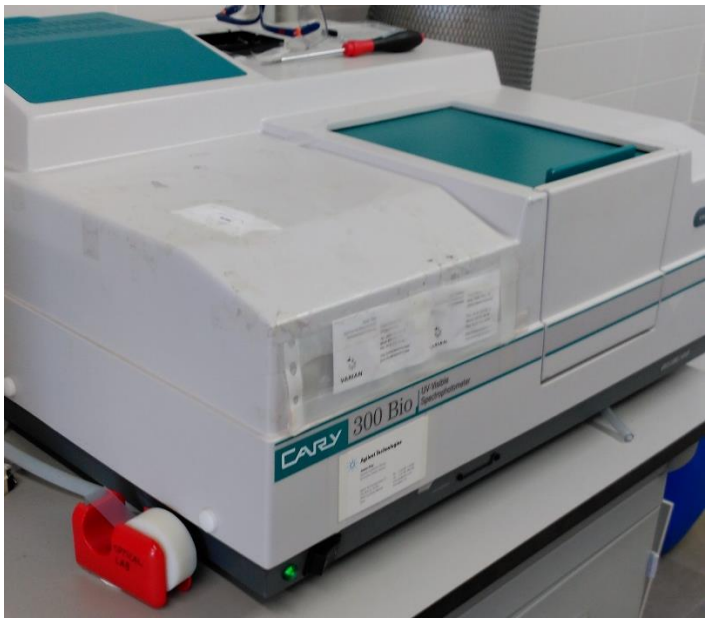

Figure 2-31 Cary 300 UV-Vis Spectrophotometer from Agilent.

2.3.3.5. Tauc plot

From the results of the previous section (absorption coefficient) we can also estimate the optical bandgap of our material. This was achieved using the so called Tauc plot, due to Jan Tauc, who related the optical absorption spectrum of amorphous germanium with their indirect transitions and proposed a method to find these gaps [81]. The method can be summarized in Equation 22 [82]:

$$(\alpha h\nu)^{\frac{1}{\gamma}} = B(h\nu - E_g) \tag{22}$$

where α is the absorption coefficient, $h\nu$ is the photon energy, E_g is the bandgap of the material, B is a constant and γ is a factor dependent on the nature of the electron transitions, being 1/2 for direct or 2 for indirect transitions. In this case, we consider Cs_2SnI_6 as a direct bandgap material. Figure 2-32 shows the Tauc plot for the material under study.

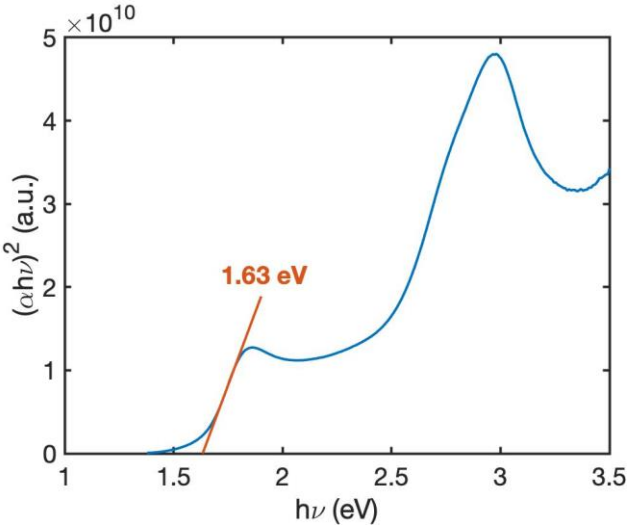

Figure 2-32 Tauc plot showing a bandgap of 1.63eV for Cs_2SnI_6 perovskite.

After the extrapolation, we obtain a value of 1.63eV for Cs_2SnI_6 perovskite. This value is coherent with the ones estimated on the literature [55]–[57], [60], [68], [83].

2.3.3.6. Photoluminescence

To check the optical gap of the material and see the kind of recombination that electrons suffered, we measured the photoluminescence of the material. Photoluminescence technique consists of illuminating a sample with light to generate electron transitions. Then the light is turned off and a detector measures the light reemitted by the sample due to radiative recombination of the electron-hole pairs generated previously. The photoluminescence signal obtained is shown in Figure 2-33.

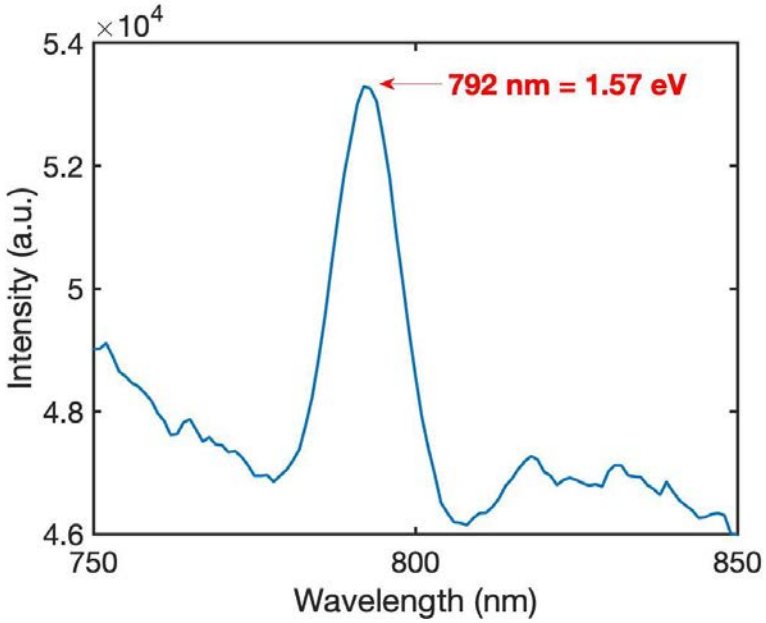

Figure 2-33 Photoluminescence measurement of Cs_2SnI_6 thin film.

An emission peak at around 792nm is observed. This wavelength is equivalent to a bandgap energy of 1.57eV, pretty similar to the value obtained using the Tauc plot from the previous section (1.63eV). This small difference could be provoked by a Stokes

shift [84]. This measurement was taken using a spectrofluorometer, Fluorolog by Horiba [85].

Furthermore, the Photoluminescence Quantum Yield (PLQY) was measured using an integrating sphere setup. This yield measures the ratio between the reemitted light and the excitation light. A high PLQY means that most of the recombination processes suffered inside the material are radiative. The highest the PLQY, the better solar cell can be built, according to [86], [87], due to the high open circuit voltage that is generated. Unfortunately, our measurements over Cs_2SnI_6 gave a PLQY value near 0%, so most of the recombination processes are non-radiative.

2.4. Visible Light Communication system with perovskite

Once having functional devices, the inclusion of them in an electronic system was studied. Of course, typical applications of these devices are focused on energy harvesting as a solar cell or solar panel. Notwithstanding, in this section we studied the performance of these devices into a Visible Light Communication (VLC) system.

But what is a VLC system? The VLC system is based on transmitting information using the light, instead of the classical Radio Frequencies (RF system). This approach leads to a lot of improvements, due to several facts:

- VLC systems are immune to electromagnetic noise or interferences (however, other light sources, as sunlight, could interfere).
- The available bandwidth is much bigger (430 to 790 THz), than in radio waves (radio waves have frequencies between 30 Hz and 300 GHz).
- VLC is more secure than RF, because light cannot go through the walls, so, the receiver should be in the same room as the emitter. Any receiver outside the line of sight of the emitter will not receive any signal.
- VLC systems have very low latency compared to RF, due to the operation frequency.
- The VLC emitter can be used also for lighting purposes using modulation, so a lot of energy can be saved.

Due to these facts, some applications are Light-Fidelity (Li-Fi), vehicle to vehicle communication or crucial installations on hospitals or aircrafts (due to interference immunity) [88]. Usually, the receivers of these systems are based on silicon photodetectors [89]–[91], but during this work we developed two different setups using an organic and a perovskite photodetector. This technology change is due to the fact that, in the recent years, there is an interest in including either perovskite [92] or organic [93] photodetectors in visible light communication systems to explore their properties.

The emitter design is shared between both works and consists of an emitter driver that transforms an audio signal (coming from a cell phone in this case) to an FM signal that modulates the current flowing through an OLED panel. This panel is the light source that illuminates the photodetector with the modulated light.

The receiver circuit design consists of the photodetector itself (which will change between studies) and a driver block which converts the photo-generated current into an adequate voltage signal to drive a loudspeaker.

It is remarkable that all the circuitry is made with off-the-shelf components, using a voltage amplifier for conditioning the cell phone signal to the next stage, then an FM modulator based on a voltage-controlled oscillator (VCO) and after that a LED conditioning circuit that uses the FM modulated signal to control the current flowing through the OLED, and thus, modulating the emitted light. The receiver is design exactly like the emitter, but following the reverse path, using a transimpedance amplifier to transform the photo-generated current into a voltage, then using a phase-lock loop (PLL) to demodulate the FM signal and ending with a power amplifier (based on LM386) to drive the loudspeaker. Both the FM modulation using VCO and the demodulation using PLL are based on CD4046 integrated circuit. Figure 2-34 shows the block diagram of the electronic design.

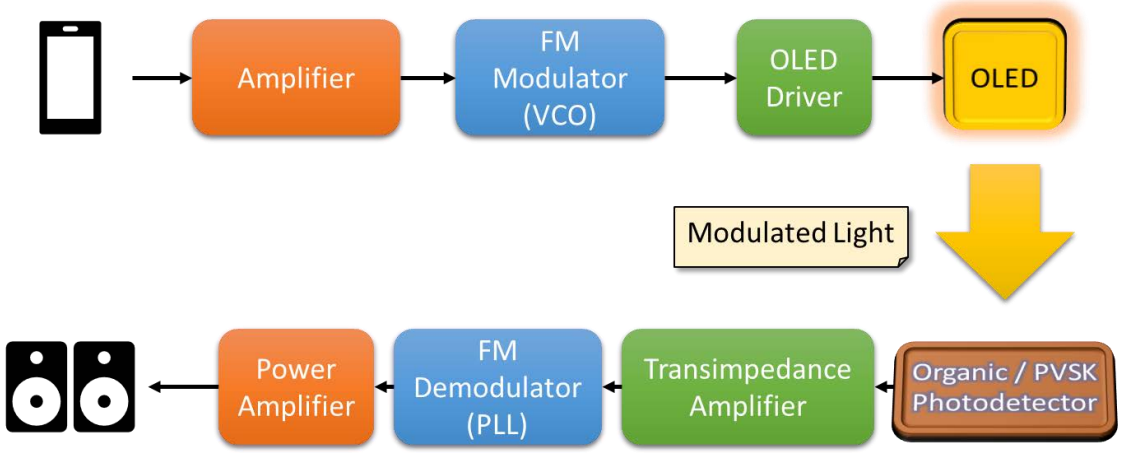

Figure 2-34 Visible Light Communication System block diagram.

The whole system requires to have a bandwidth higher than 40kHz following the Nyquist criterion, because we are working with an audio signal, which goes from 20Hz to 20kHz. Also, all the system will be flexible in order to increase its integration properties (e.g., integrate the receiver in clothes).

To check the transmission capabilities, the bandwidth of the emitter and receiver are analyzed. The emitter (OLED) is modelled using impedance spectroscopy analysis at several bias current, to check its parameter variation depending on the bias. The equivalent circuit and the parameter variation are shown at Figure 2-35. It should be mentioned that the series resistance (Rs) which represents the wires and contacts do not depend on the bias polarization, i.e., is constant.

This equivalent circuit represents a low-pass filter behavior, being the cut-off frequency determined by Equation 23:

$$f_c = \left(2\pi \cdot C_{OLED} \cdot (R_s||R_P)\right)^{-1} \tag{23}$$

being C_{OLED} the associated OLED capacitance, and $(R_s||R_P)$ the parallel between the series resistance and parallel resistance of the equivalent circuit of the OLED. Using this equation, the cut-off frequency goes from 9.22kHz (at 5mA bias) to 56kHz (at 85mA). So, we can conclude that, if the bias current is high enough, the OLED will not limit the bandwidth in an audio link.

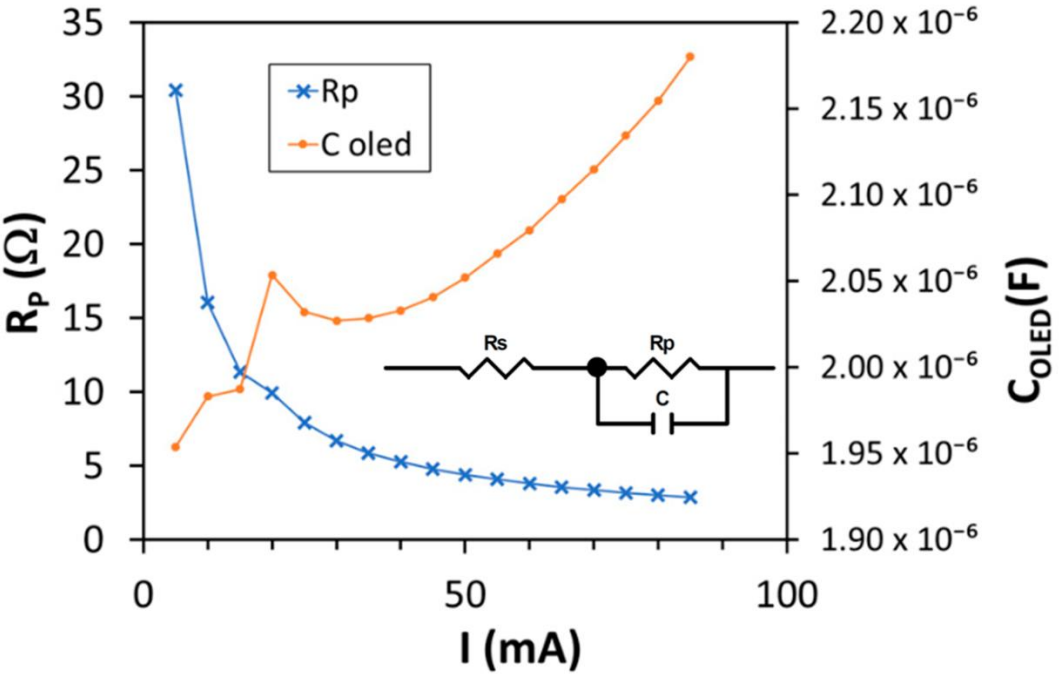

Figure 2-35 Impedance Spectroscopy analysis of OLED. The equivalent circuit is shown.

Regarding the photodetectors, the frequency response of the organic flexible detector and the perovskite detector is also analyzed. Here, the frequency response is measured using a lock-in amplifier, going from 10Hz to 10MHz. This system uses a red LED biased with a square signal driven from the lock-in amplifier and detects the signal coming from the photodetector. Figure 2-36 shows the frequency response of the organic photodetector (top) and the perovskite detector (bottom).

It can be seen that the cut-off frequency, and thus, the bandwidth of the organic photodetector is bias-dependent, and it goes from around 100kHz at 0V up to 200kHz at 2V. In the case of perovskite detector, the bandwidth is around 116kHz at 0V bias. However, in this case the reverse bias is not analyzed, because reverse bias can accelerate the degradation process of perovskite-based devices [94]. So, it can be concluded that every component in both systems is able to transmit information successfully in an audio link.

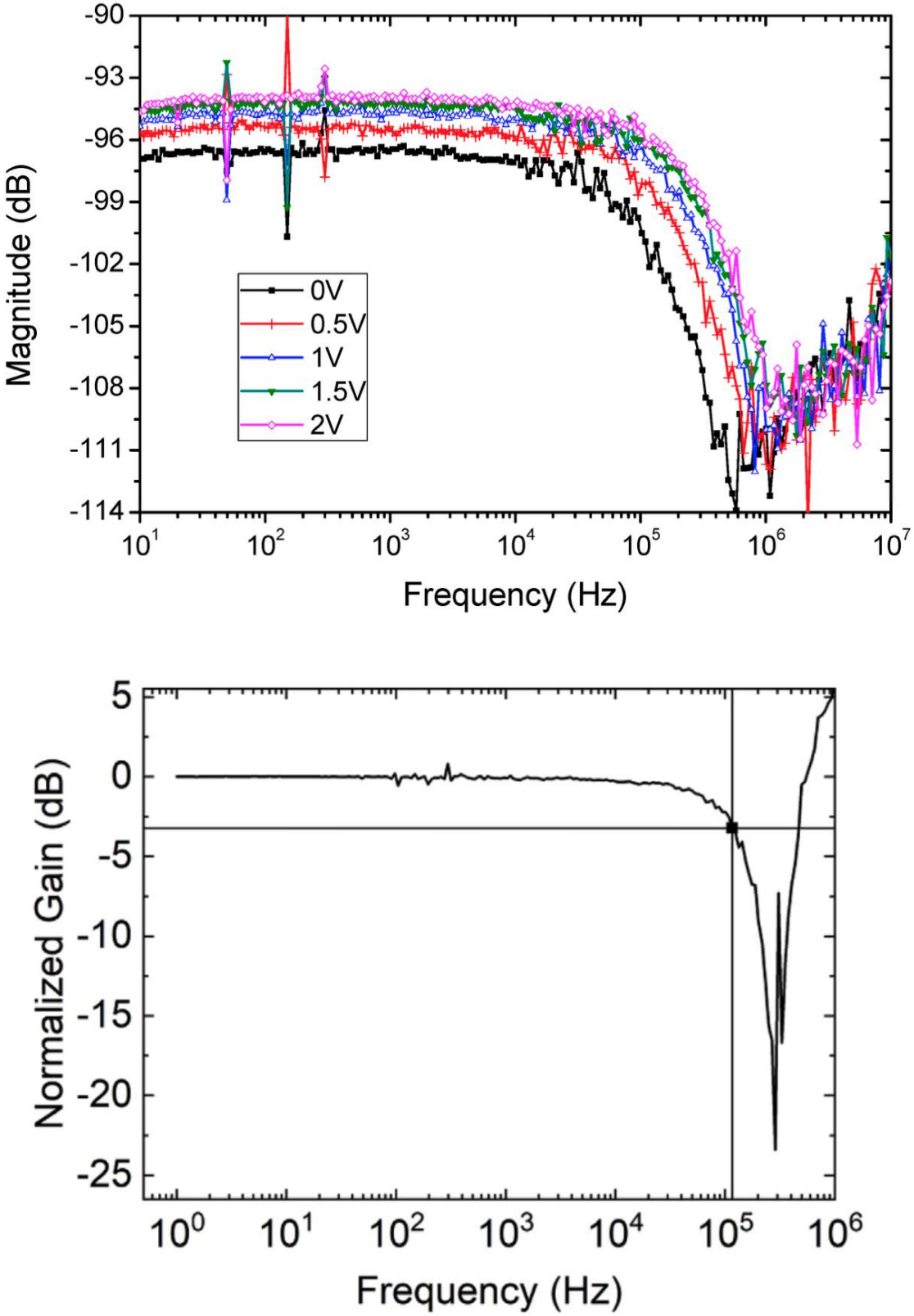

Figure 2-36 Frequency response of organic photodiode at several reverse bias (top) and perovskite detector at no-bias (bottom).

A summary of the characterization results of both systems can be checked at Table 2-3, where also other parameters are included, like the Noise-Equivalent Power (NEP) and the specific detectivity. The complete studies can be found at MDPI Sensors [95] and Organic Electronics journals [96].

	Organic PD VLC	Perovskite PD VLC
Bandwidth	$100\sim200\ kHz$	$\sim120\ kHz$
Noise Equivalent Power	$2.78 \cdot 10^{-12}\ [WHz^{-1/2}]$	$6.6\sim9.9 \cdot 10^{-15} [WHz^{-1/2}]$
Specific Detectivity	$1.8 \cdot 10^{11}\ Jones$	$4.1\sim6.1 \cdot 10^{13}\ Jones$

Table 2-3 Main characteristics of Organic vs Perovskite Photodiode in a VLC system.

We can conclude here, analyzing both VLC systems that, despite that the perovskite photodetector is more limited in terms of bandwidth, its specific detectivity is two orders of magnitude higher than the organic photodetector. Using these new generation technologies in these applications can lead to cost-effective systems, much cheaper than the actual ones.

Both systems in their actual state can effectively transmit audio signals, so both can be applied, for example, as a closed-communication system inside an office, where the luminaires could send messages to each desk of the office. Then, the employee could hear the message connecting a set of headphones in its desk. This would be a more secure method compared to a telephone call or a communication via Internet.

2.5. Bibliography

[1] A. Kojima, K. Teshima, Y. Shirai, and T. Miyasaka, "Organometal Halide Perovskites as Visible-Light Sensitizers for Photovoltaic Cells," *J. Am. Chem. Soc.*, vol. 131, no. 17, pp. 6050–6051, May 2009, doi: 10.1021/ja809598r.

[2] "Best Research-Cell Efficiency Chart." https://www.nrel.gov/pv/cell-efficiency.html (accessed Dec. 22, 2020).

[3] "This Month in Physics History." http://www.aps.org/publications/apsnews/200904/physicshistory.cfm (accessed Dec. 22, 2020).

[4] "Web of Science [v.5.35] - Colección principal de Web of ScienceBúsqueda básica." https://apps.webofknowledge.com/WOS_GeneralSearch_input.do?product=WOS&search_mode=GeneralSearch&SID=E2Drj48qA6GvnVAG5mw&preferencesSaved= (accessed Dec. 22, 2020).

[5] "Perovskite Mineral Data." http://webmineral.com/data/Perovskite.shtml#.X-IoMNhKiUk (accessed Dec. 22, 2020).

[6] Y. Chen, L. Zhang, Y. Zhang, H. Gao, and H. Yan, "Large-area perovskite solar cells – a review of recent progress and issues," *RSC Adv.*, vol. 8, no. 19, pp. 10489–10508, 2018, doi: 10.1039/C8RA00384J.

[7] A. Walsh, "The quest for new functionality," *Nature Chem*, vol. 7, no. 4, pp. 274–275, Apr. 2015, doi: 10.1038/nchem.2213.

[8] S. M. Woodley and R. Catlow, "Crystal structure prediction from first principles," *Nature Mater*, vol. 7, no. 12, pp. 937–946, Dec. 2008, doi: 10.1038/nmat2321.

[9] V. M. Goldschmidt, “Die Gesetze der Krystallochemie,” *Naturwissenschaften*, vol. 14, no. 21, pp. 477–485, May 1926, doi: 10.1007/BF01507527.

[10] W. Travis, E. N. K. Glover, H. Bronstein, D. O. Scanlon, and R. G. Palgrave, “On the application of the tolerance factor to inorganic and hybrid halide perovskites: a revised system,” *Chem. Sci.*, vol. 7, no. 7, pp. 4548–4556, 2016, doi: 10.1039/C5SC04845A.

[11] J. Qian, B. Xu, and W. Tian, “A comprehensive theoretical study of halide perovskites ABX3,” *Organic Electronics*, vol. 37, pp. 61–73, Oct. 2016, doi: 10.1016/j.orgel.2016.05.046.

[12] S. Wozny *et al.*, “Controlled Humidity Study on the Formation of Higher Efficiency Formamidinium Lead Triiodide-Based Solar Cells,” *Chem. Mater.*, vol. 27, no. 13, pp. 4814–4820, Jul. 2015, doi: 10.1021/acs.chemmater.5b01691.

[13] N. K. Noel *et al.*, “Lead-free organic–inorganic tin halide perovskites for photovoltaic applications,” *Energy Environ. Sci.*, vol. 7, no. 9, pp. 3061–3068, Aug. 2014, doi: 10.1039/C4EE01076K.

[14] T. Zhang, H. Li, H. Ban, Q. Sun, Y. Shen, and M. Wang, “Efficient CsSnI3-based inorganic perovskite solar cells based on a mesoscopic metal oxide framework via incorporating a donor element,” *J. Mater. Chem. A*, vol. 8, no. 7, pp. 4118–4124, Feb. 2020, doi: 10.1039/C9TA11794F.

[15] S. Shao *et al.*, “Enhancing the crystallinity and perfecting the orientation of formamidinium tin iodide for highly efficient Sn-based perovskite solar cells,” *Nano Energy*, vol. 60, pp. 810–816, Jun. 2019, doi: 10.1016/j.nanoen.2019.04.040.

[16] T. Krishnamoorthy *et al.*, “Lead-free germanium iodide perovskite materials for photovoltaic applications,” *J. Mater. Chem. A*, vol. 3, no. 47, pp. 23829–23832, 2015, doi: 10.1039/C5TA05741H.

[17] A. Urbina, “The balance between efficiency, stability and environmental impacts in perovskite solar cells: a review,” *J. Phys. Energy*, vol. 2, no. 2, p. 022001, Feb. 2020, doi: 10.1088/2515-7655/ab5eee.

[18] M. Chen *et al.*, “Highly stable and efficient all-inorganic lead-free perovskite solar cells with native-oxide passivation,” *Nature Communications*, vol. 10, no. 1, Art. no. 1, Jan. 2019, doi: 10.1038/s41467-018-07951-y.

[19] “How solar cell is made - material, manufacture, making, used, parts, structure, procedure, steps.” http://www.madehow.com/Volume-1/Solar-Cell.html (accessed Jan. 14, 2021).

[20] “Thin Film Coating Solution-Processing Techniques Compared | Ossila.” https://www.ossila.com/pages/solution-processing-techniques-comparison#SpinCoating (accessed Jan. 14, 2021).

[21] A. G. Emslie, F. T. Bonner, and L. G. Peck, “Flow of a Viscous Liquid on a Rotating Disk,” *Journal of Applied Physics*, vol. 29, no. 5, pp. 858–862, May 1958, doi: 10.1063/1.1723300.

[22] D. Meyerhofer, “Characteristics of resist films produced by spinning,” *Journal of Applied Physics*, vol. 49, no. 7, pp. 3993–3997, Jul. 1978, doi: 10.1063/1.325357.

[23] “MMA / PMMA resists.” https://www.epfl.ch/research/facilities/cmi/equipment/ebeam-lithography/raith-ebpg5000/ebeam-resists-available-in-cmi/mma-pmma-resists/ (accessed Jan. 14, 2021).

[24] L. S. Coaters, “Spin coaters from Laurell - WS-650-23B Spin Coater,” *Laurell Technologies Corporation*. http://www.laurell.com/spin-coater/?model=WS-650-23B (accessed Jan. 15, 2021).
[25] “Spin Coater, Low Price Compact Spin Coater Machine,” *Ossila*. https://www.ossila.com/products/spin-coater (accessed Jan. 15, 2021).
[26] A. J. Sanchez-Herencia, “Water Based Colloidal Processing of Ceramic Laminates,” *KEM*, vol. 333, pp. 39–48, Mar. 2007, doi: 10.4028/www.scientific.net/KEM.333.39.
[27] L. Landau, L. B., “Dragging of a liquid by a moving plate,” *Acta Physicochim.*, vol. 17, pp. 42–54, 1942.
[28] “Dip Coating Theory | Dip Coating Thin Films, Complete Guide,” *Ossila*. https://www.ossila.com/pages/dip-coating-theory-film-thickness (accessed Jan. 15, 2021).
[29] “ND-DC Dip Coater | Nadetech Innovations.” https://nadetech.com/products/dip-coating/nd-dc (accessed Jan. 15, 2021).
[30] “Slot Die Coating,” *nTact*. https://ntact.com/applications/slot-die-coating/ (accessed Jan. 18, 2021).
[31] “Slot-Die Coating Theory, Design & Applications,” *Ossila*. https://www.ossila.com/pages/slot-die-coating-theory (accessed Jan. 18, 2021).
[32] A. Berni, M. Mennig, and H. Schmidt, “Doctor Blade,” in *Sol-Gel Technologies for Glass Producers and Users*, M. A. Aegerter and M. Mennig, Eds. Boston, MA: Springer US, 2004, pp. 89–92.
[33] S. Chatterjee and A. J. Pal, “Influence of metal substitution on hybrid halide perovskites: towards lead-free perovskite solar cells,” *J. Mater. Chem. A*, vol. 6, no. 9, pp. 3793–3823, Feb. 2018, doi: 10.1039/C7TA09943F.
[34] F. Sani, S. Shafie, H. N. Lim, and A. O. Musa, “Advancement on Lead-Free Organic-Inorganic Halide Perovskite Solar Cells: A Review,” *Materials*, vol. 11, no. 6, Art. no. 6, Jun. 2018, doi: 10.3390/ma11061008.
[35] X. Wang, T. Zhang, Y. Lou, and Y. Zhao, “All-inorganic lead-free perovskites for optoelectronic applications,” *Mater. Chem. Front.*, vol. 3, no. 3, pp. 365–375, Feb. 2019, doi: 10.1039/C8QM00611C.
[36] H. Fu, “Review of lead-free halide perovskites as light-absorbers for photovoltaic applications: From materials to solar cells,” *Solar Energy Materials and Solar Cells*, vol. 193, pp. 107–132, May 2019, doi: 10.1016/j.solmat.2018.12.038.
[37] J. Zhou, Z. Xia, M. S. Molokeev, X. Zhang, D. Peng, and Q. Liu, “Composition design, optical gap and stability investigations of lead-free halide double perovskite Cs2AgInCl6,” *J. Mater. Chem. A*, vol. 5, no. 29, pp. 15031–15037, Jul. 2017, doi: 10.1039/C7TA04690A.
[38] G. Volonakis *et al.*, “Cs2InAgCl6: A New Lead-Free Halide Double Perovskite with Direct Band Gap,” *J. Phys. Chem. Lett.*, vol. 8, no. 4, pp. 772–778, Feb. 2017, doi: 10.1021/acs.jpclett.6b02682.
[39] L. Schade *et al.*, “Structural and Optical Properties of Cs2AgBiBr6 Double Perovskite,” *ACS Energy Lett.*, vol. 4, no. 1, pp. 299–305, Jan. 2019, doi: 10.1021/acsenergylett.8b02090.
[40] W. Gao *et al.*, “High-Quality Cs2AgBiBr6 Double Perovskite Film for Lead-Free Inverted Planar Heterojunction Solar Cells with 2.2 % Efficiency,” *ChemPhysChem*, vol. 19, no. 14, pp. 1696–1700, 2018, doi: https://doi.org/10.1002/cphc.201800346.

[41] M. Wang *et al.*, "High-Quality Sequential-Vapor-Deposited Cs2AgBiBr6 Thin Films for Lead-Free Perovskite Solar Cells," *Solar RRL*, vol. 2, no. 12, p. 1800217, 2018, doi: https://doi.org/10.1002/solr.201800217.

[42] F. Locardi *et al.*, "Colloidal Synthesis of Double Perovskite Cs2AgInCl6 and Mn-Doped Cs2AgInCl6 Nanocrystals," *J. Am. Chem. Soc.*, vol. 140, no. 40, pp. 12989–12995, Oct. 2018, doi: 10.1021/jacs.8b07983.

[43] "Efficient and stable emission of warm-white light from lead-free halide double perovskites | Nature." https://www.nature.com/articles/s41586-018-0691-0?WT.feed_name=subjects_materials-for-optics (accessed Jan. 19, 2021).

[44] M. Konstantakou and T. Stergiopoulos, "A critical review on tin halide perovskite solar cells," *J. Mater. Chem. A*, vol. 5, no. 23, pp. 11518–11549, Jun. 2017, doi: 10.1039/C7TA00929A.

[45] A. Babayigit, A. Ethirajan, M. Muller, and B. Conings, "Toxicity of organometal halide perovskite solar cells," *Nature Materials*, vol. 15, no. 3, Art. no. 3, Mar. 2016, doi: 10.1038/nmat4572.

[46] K. Shum *et al.*, "Synthesis and characterization of CsSnI3 thin films," *Appl. Phys. Lett.*, vol. 96, no. 22, p. 221903, May 2010, doi: 10.1063/1.3442511.

[47] Z. Chen, J. J. Wang, Y. Ren, C. Yu, and K. Shum, "Schottky solar cells based on CsSnI3 thin-films," *Appl. Phys. Lett.*, vol. 101, no. 9, p. 093901, Aug. 2012, doi: 10.1063/1.4748888.

[48] I. Chung *et al.*, "CsSnI3: Semiconductor or Metal? High Electrical Conductivity and Strong Near-Infrared Photoluminescence from a Single Material. High Hole Mobility and Phase-Transitions," *J. Am. Chem. Soc.*, vol. 134, no. 20, pp. 8579–8587, May 2012, doi: 10.1021/ja301539s.

[49] Z. Xiao, Y. Zhou, H. Hosono, and T. Kamiya, "Intrinsic defects in a photovoltaic perovskite variant Cs2SnI6," *Phys. Chem. Chem. Phys.*, vol. 17, no. 29, pp. 18900–18903, Jul. 2015, doi: 10.1039/C5CP03102H.

[50] A. E. Maughan, A. M. Ganose, D. O. Scanlon, and J. R. Neilson, "Perspectives and Design Principles of Vacancy-Ordered Double Perovskite Halide Semiconductors," *Chem. Mater.*, vol. 31, no. 4, pp. 1184–1195, Feb. 2019, doi: 10.1021/acs.chemmater.8b05036.

[51] G. Bounos *et al.*, "Defect Perovskites under Pressure: Structural Evolution of Cs2SnX6 (X = Cl, Br, I)," *J. Phys. Chem. C*, vol. 122, no. 42, pp. 24004–24013, Oct. 2018, doi: 10.1021/acs.jpcc.8b08449.

[52] M. H. Kumar *et al.*, "Lead-Free Halide Perovskite Solar Cells with High Photocurrents Realized Through Vacancy Modulation," *Advanced Materials*, vol. 26, no. 41, pp. 7122–7127, 2014, doi: https://doi.org/10.1002/adma.201401991.

[53] K. P. Marshall, R. I. Walton, and R. A. Hatton, "Tin perovskite/fullerene planar layer photovoltaics: improving the efficiency and stability of lead-free devices," *J. Mater. Chem. A*, vol. 3, no. 21, pp. 11631–11640, May 2015, doi: 10.1039/C5TA02950C.

[54] "Fabrication of Efficient Formamidinium Tin Iodide Perovskite Solar Cells through SnF2–Pyrazine Complex | Journal of the American Chemical Society." https://pubs.acs.org/doi/10.1021/jacs.6b00142 (accessed Jan. 20, 2021).

[55] B. Lee *et al.*, "Air-Stable Molecular Semiconducting Iodosalts for Solar Cell Applications: Cs2SnI6 as a Hole Conductor," *J. Am. Chem. Soc.*, vol. 136, no. 43, pp. 15379–15385, Oct. 2014, doi: 10.1021/ja508464w.

[56] H. Shin *et al.*, "Surface State-Mediated Charge Transfer of Cs2SnI6 and Its Application in Dye-Sensitized Solar Cells," *Advanced Energy Materials*, vol. 9, no. 3, p. 1803243, 2019, doi: https://doi.org/10.1002/aenm.201803243.

[57] A. Kaltzoglou *et al.*, "Optical-Vibrational Properties of the Cs2SnX6 (X = Cl, Br, I) Defect Perovskites and Hole-Transport Efficiency in Dye-Sensitized Solar Cells," *J. Phys. Chem. C*, vol. 120, no. 22, pp. 11777–11785, Jun. 2016, doi: 10.1021/acs.jpcc.6b02175.

[58] J. Chen *et al.*, "Tin(IV)-Tolerant Vapor-Phase Growth and Photophysical Properties of Aligned Cesium Tin Halide Perovskite (CsSnX3; X = Br, I) Nanowires," *ACS Energy Lett.*, vol. 4, no. 5, pp. 1045–1052, May 2019, doi: 10.1021/acsenergylett.9b00543.

[59] L.-J. Chen, C.-R. Lee, Y.-J. Chuang, Z.-H. Wu, and C. Chen, "Synthesis and Optical Properties of Lead-Free Cesium Tin Halide Perovskite Quantum Rods with High-Performance Solar Cell Application," *J. Phys. Chem. Lett.*, vol. 7, no. 24, pp. 5028–5035, Dec. 2016, doi: 10.1021/acs.jpclett.6b02344.

[60] J. C.-R. Ke *et al.*, "Ambient-air-stable inorganic Cs2SnI6 double perovskite thin films via aerosol-assisted chemical vapour deposition," *J. Mater. Chem. A*, vol. 6, no. 24, pp. 11205–11214, Jun. 2018, doi: 10.1039/C8TA03133A.

[61] E. López-Fraguas, S. Masi, and I. Mora-Seró, "Optical Characterization of Lead-Free Cs2SnI6 Double Perovskite Fabricated from Degraded and Reconstructed CsSnI3 Films," *ACS Appl. Energy Mater.*, vol. 2, no. 12, pp. 8381–8387, Dec. 2019, doi: 10.1021/acsaem.9b01827.

[62] K. Mahmood, S. Sarwar, and M. T. Mehran, "Current status of electron transport layers in perovskite solar cells: materials and properties," *RSC Adv.*, vol. 7, no. 28, pp. 17044–17062, Mar. 2017, doi: 10.1039/C7RA00002B.

[63] S. Pitchaiya *et al.*, "A review on the classification of organic/inorganic/carbonaceous hole transporting materials for perovskite solar cell application," *Arabian Journal of Chemistry*, vol. 13, no. 1, pp. 2526–2557, Jan. 2020, doi: 10.1016/j.arabjc.2018.06.006.

[64] P. F. Méndez, S. K. M. Muhammed, E. M. Barea, S. Masi, and I. Mora-Seró, "Analysis of the UV–Ozone-Treated SnO2 Electron Transporting Layer in Planar Perovskite Solar Cells for High Performance and Reduced Hysteresis," *Solar RRL*, vol. 3, no. 9, p. 1900191, 2019, doi: https://doi.org/10.1002/solr.201900191.

[65] M. Konstantakou, D. Perganti, P. Falaras, and T. Stergiopoulos, "Anti-Solvent Crystallization Strategies for Highly Efficient Perovskite Solar Cells," *Crystals*, vol. 7, no. 10, Art. no. 10, Oct. 2017, doi: 10.3390/cryst7100291.

[66] E. J. Juarez-Perez, M. R. Leyden, S. Wang, L. K. Ono, Z. Hawash, and Y. Qi, "Role of the Dopants on the Morphological and Transport Properties of Spiro-MeOTAD Hole Transport Layer," *Chem. Mater.*, vol. 28, no. 16, pp. 5702–5709, Aug. 2016, doi: 10.1021/acs.chemmater.6b01777.

[67] A. Abate *et al.*, "Lithium salts as 'redox active' p-type dopants for organic semiconductors and their impact in solid-state dye-sensitized solar cells," *Phys. Chem. Chem. Phys.*, vol. 15, no. 7, pp. 2572–2579, Jan. 2013, doi: 10.1039/C2CP44397J.

[68] "Thin-Film Deposition and Characterization of a Sn-Deficient Perovskite Derivative Cs2SnI6 | Chemistry of Materials."

https://pubs.acs.org/doi/abs/10.1021/acs.chemmater.6b00433 (accessed Jan. 21, 2021).

[69] F. Guo *et al.*, "A two-step dry process for Cs_2SnI_6 perovskite thin film," *Materials Research Letters*, vol. 5, no. 8, pp. 540–546, Nov. 2017, doi: 10.1080/21663831.2017.1346525.

[70] "X-ray Powder Diffraction (XRD)," *Techniques*. https://serc.carleton.edu/research_education/geochemsheets/techniques/XRD.html (accessed Jan. 27, 2021).

[71] "American Mineralogist Crystal Structure Database." http://rruff.geo.arizona.edu/AMS/amcsd.php (accessed Jan. 27, 2021).

[72] W. Werker, "Die Krystallstruktur des Rb2SnJ6 und Cs2SnJ6," *Recueil des Travaux Chimiques des Pays-Bas*, vol. 58, no. 3, pp. 257–258, 1939, doi: https://doi.org/10.1002/recl.19390580309.

[73] J. Zemann, "Crystal structures, 2nd edition. Vol. 1 by R. W. G. Wyckoff," *Acta Crystallographica*, vol. 18, no. 1, pp. 139–139, 1965, doi: https://doi.org/10.1107/S0365110X65000361.

[74] "D8 ADVANCE." https://www.bruker.com/en/products-and-solutions/diffractometers-and-scattering-systems/x-ray-diffractometers/d8-advance-family/d8-advance.html (accessed Jan. 28, 2021).

[75] "Scanning Electron Microscopy," *Nanoscience Instruments*. https://www.nanoscience.com/techniques/scanning-electron-microscopy/ (accessed Jan. 28, 2021).

[76] "JSM-7001F Schottky Emission Scanning Electron Microscope | Products | JEOL Ltd." https://www.jeol.co.jp/en/products/detail/JSM-7001F.html (accessed Jan. 28, 2021).

[77] "Optics, 5th Edition." /content/one-dot-com/one-dot-com/us/en/higher-education/program.html (accessed Feb. 01, 2021).

[78] G. E. Eperon, V. M. Burlakov, A. Goriely, and H. J. Snaith, "Neutral Color Semitransparent Microstructured Perovskite Solar Cells," *ACS Nano*, vol. 8, no. 1, pp. 591–598, Jan. 2014, doi: 10.1021/nn4052309.

[79] E. Della Gaspera *et al.*, "Ultra-thin high efficiency semitransparent perovskite solar cells," *Nano Energy*, vol. 13, pp. 249–257, Apr. 2015, doi: 10.1016/j.nanoen.2015.02.028.

[80] S. Masi *et al.*, "Organic Gelators as Growth Control Agents for Stable and Reproducible Hybrid Perovskite-Based Solar Cells," *Advanced Energy Materials*, vol. 7, no. 14, p. 1602600, 2017, doi: https://doi.org/10.1002/aenm.201602600.

[81] J. Tauc, "Optical properties and electronic structure of amorphous Ge and Si," *Materials Research Bulletin*, vol. 3, no. 1, pp. 37–46, Jan. 1968, doi: 10.1016/0025-5408(68)90023-8.

[82] P. Makuła, M. Pacia, and W. Macyk, "How To Correctly Determine the Band Gap Energy of Modified Semiconductor Photocatalysts Based on UV–Vis Spectra," *J. Phys. Chem. Lett.*, vol. 9, no. 23, pp. 6814–6817, Dec. 2018, doi: 10.1021/acs.jpclett.8b02892.

[83] X. Qiu *et al.*, "From unstable CsSnI3 to air-stable Cs2SnI6: A lead-free perovskite solar cell light absorber with bandgap of 1.48eV and high absorption coefficient," *Solar Energy Materials and Solar Cells*, vol. 159, pp. 227–234, Jan. 2017, doi: 10.1016/j.solmat.2016.09.022.

[84] “Stokes Shift, Fluorescence Spectroscopy,” *Edinburgh Instruments*. https://www.edinst.com/blog/what-is-the-stokes-shift/ (accessed Feb. 01, 2021).
[85] “Fluorolog-QM Horiba.” https://www.horiba.com/en_en/products/detail/action/show/Product/fluorolog-qm-1997/ (accessed Feb. 01, 2021).
[86] L. M. Pazos-Outón *et al.*, “Photon recycling in lead iodide perovskite solar cells,” *Science*, vol. 351, no. 6280, pp. 1430–1433, Mar. 2016, doi: 10.1126/science.aaf1168.
[87] E. Yablonovitch, “Lead halides join the top optoelectronic league,” *Science*, vol. 351, no. 6280, pp. 1401–1401, Mar. 2016, doi: 10.1126/science.aaf4603.
[88] L. U. Khan, “Visible light communication: Applications, architecture, standardization and research challenges,” *Digital Communications and Networks*, vol. 3, no. 2, pp. 78–88, May 2017, doi: 10.1016/j.dcan.2016.07.004.
[89] Y. Wang, Y. Wang, N. Chi, J. Yu, and H. Shang, “Demonstration of 575-Mb/s downlink and 225-Mb/s uplink bi-directional SCM-WDM visible light communication using RGB LED and phosphor-based LED,” *Opt. Express, OE*, vol. 21, no. 1, pp. 1203–1208, Jan. 2013, doi: 10.1364/OE.21.001203.
[90] N. Chi, Y. Wang, Y. Wang, X. Huang, and X. Lu, “Ultra-high-speed single red-green-blue light-emitting diode-based visible light communication system utilizing advanced modulation formats,” *Chin. Opt. Lett., COL*, vol. 12, no. 1, p. 010605, Jan. 2014.
[91] R. Li, Y. Wang, C. Tang, Y. Wang, H. Shang, and N. Chi, “Improving performance of 750-Mb/s visible light communication system using adaptive Nyquist windowing,” *Chin. Opt. Lett., COL*, vol. 11, no. 8, p. 080605, Aug. 2013.
[92] I. Dursun *et al.*, “Perovskite Nanocrystals as a Color Converter for Visible Light Communication,” *ACS Photonics*, vol. 3, no. 7, pp. 1150–1156, Jul. 2016, doi: 10.1021/acsphotonics.6b00187.
[93] P. Corral, F. Rodríguez-Mas, J. L. Alonso, J. C. Ferrer, and S. Fernández de Ávila, “A Low-Cost IEEE 802.15.7 Communication System Based on Organic Photodetection for Device-to-Device Connections,” *Sensors*, vol. 20, no. 3, Art. no. 3, Jan. 2020, doi: 10.3390/s20030714.
[94] A. R. Bowring, L. Bertoluzzi, B. C. O’Regan, and M. D. McGehee, “Reverse Bias Behavior of Halide Perovskite Solar Cells,” *Advanced Energy Materials*, vol. 8, no. 8, p. 1702365, 2018, doi: https://doi.org/10.1002/aenm.201702365.
[95] C. Vega-Colado *et al.*, “An All-Organic Flexible Visible Light Communication System,” *Sensors*, vol. 18, no. 9, Art. no. 9, Sep. 2018, doi: 10.3390/s18093045.
[96] E. López-Fraguas *et al.*, “Visible Light Communication system using an organic emitter and a perovskite photodetector,” *Organic Electronics*, vol. 73, pp. 292–298, Oct. 2019, doi: 10.1016/j.orgel.2019.06.028.

Chapter 3:Solar cell characterization. SUNBOX

"The power of the sun in the palm of my hand" – Dr. Otto Octavius

In this Chapter, we will explore the most common solar cell characterization techniques and the elements needed in such measurements. The fundamental characterization instrument that we are going to use -although not the only one- is a solar simulator. Due to the lack of a solar simulator in our lab, we developed one from scratch. Along this Chapter the development of such a low-cost AAA-Class solar simulator (SUNBOX) is also explained, as well as its final performance, using it to characterize several samples with a variety of studies.

3.1. Solar cells characterization techniques

When the building process of a new device is done (see Chapter 2) a proper characterization is needed. Only in this way main characteristics of a device can be correctly stated and compared with other devices of the same or different technology. Throughout this section, several characterization techniques will be explained, from their physical basis to the results that can be obtained by using them.

3.1.1. I-V or J-V curves

One of the easiest measurements that return very useful information is the current-voltage curve. This measurement consists of setting a known voltage along the device under test and measure the electric current that is flowing through it. Actually, this method can be applied to a lot of electronic components (e.g., resistors, diodes, LEDs, etc.), not only solar cells, and it gives useful information about the DC (direct current) response of the component. Focusing on a solar cell, its DC behavior can be modelled as a diode, with a current source that acts as the photogenerated current and a series and shunt resistors that model the losses of the device (Figure 3-1 [1]).

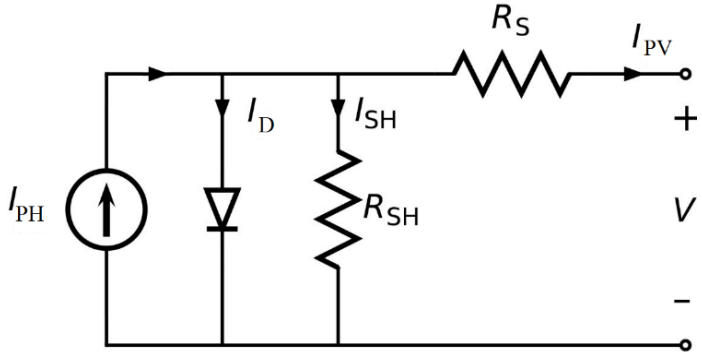

Figure 3-1 DC Equivalent circuit of a solar cell. Obtained from [1]

Here, of course, I_{PH} will depend on the illumination level, and that is why the I-V measurements are done under standard conditions, defined as 1 atm of pressure, 25°C of temperature and 1000W/m^2 of irradiance. These fixed conditions make the results of several experiments in several samples comparable. Apart from these conditions, we also need the I-V tracer, in other words, the device to measure the I-V curve. Usually this

is known as a potentiostat, and it is very useful in electrochemical measurements. Notwithstanding, it can be also used with a solar cell. Figure 3-2 shows an example of a solar cell J-V curve traced with a potentiostat [2].

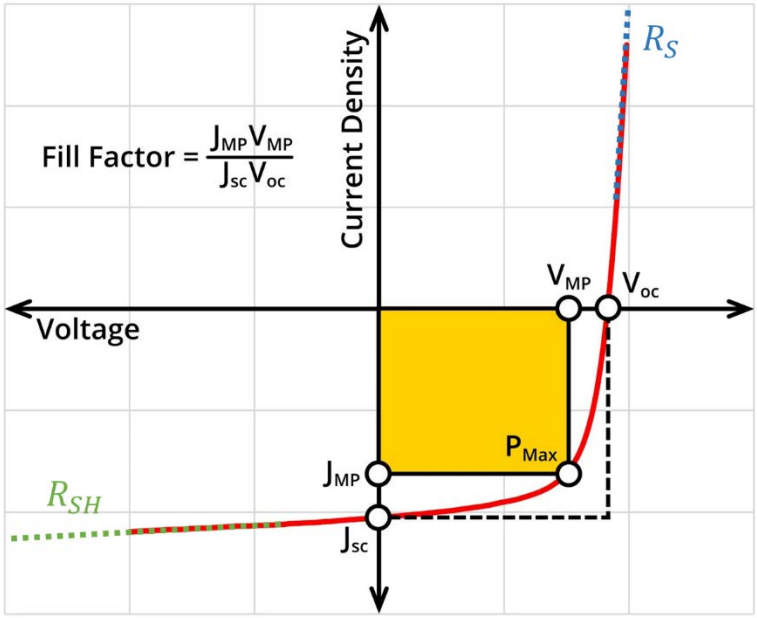

Figure 3-2 Example of a Solar cell J-V curve. Adapted from [2].

It can be noted that both I-V and J-V are used, but they are not the same. The parameter I stands for current (A) while J stands for current density (A/m^2). J-V curve is the most used, because it neglects the effect of the active area of the device, making samples of several sizes comparable between them. This cannot be made with I-V curve, because a sample of 1 m^2 of active area will generate much more current than one with 1 cm^2.

The main parameters that can be obtained from the J-V curve are the following:

- J_{SC}, Short circuit current density: This is the current density given by the device when their terminals are short circuited (i.e., the voltage across the terminals is 0V). It is worth mentioning that this current is dependent mainly on the amount of light that the device is receiving (1000W/m^2 under standard conditions). The higher the current, the best photogeneration the device will have.
- V_{OC}, Open circuit voltage: This is the voltage generated by the sample when it is not connected to any load. Equation 24 [3] shows that it is mainly dependent on temperature (T), short circuit current (I_{SC}) and dark saturation current (I_{o1}), which represents a property of the modelled diode at Figure 3-1.

$$V_{OC} = \frac{kT}{q}\ln\left(\frac{I_{SC}+I_{o1}}{I_{o1}}\right) \approx \frac{kT}{q}\ln\left(\frac{I_{SC}}{I_{o1}}\right) \quad (24)$$

- P_{MAX}, Maximum-power point: This value represents the maximum power that the solar cell can produce, and it is calculated searching the maximum point of the P-V (power vs voltage) curve. Theoretical calculation is shown in Equation 25 [3]:

$$\left.\frac{\delta P}{\delta V}\right|_{V=V_{MP}} = \left.\frac{\delta(IV)}{\delta V}\right|_{V=V_{MP}} = \left[I + V\frac{\delta I}{\delta V}\right]\Big|_{V=V_{MP}} = 0 \quad (25)$$

From this equation we can define two additional parameters, known as V_{MP} and I_{MP}. These stands for the voltage and current at maximum power point, showing the exact bias point of the solar cell at which it will generate the maximum power. Ideally, V_{MP} and I_{MP} should be equal to V_{OC} and I_{SC}, but due to the parasitic losses and the non-ideal behavior of the diode, this is not true. To qualify the "goodness" of a solar cell, we define the next parameter.

- FF, Fill Factor: This parameter is one of the most representative in terms of guessing how good or bad a solar cell performs, and shows the ideality of the diode and its losses. It is computed using Equation 26.

$$FF = \frac{P_{MAX}}{P_{Ideal}} = \frac{V_{MP}I_{MP}}{V_{OC}I_{SC}} = \frac{V_{MP}J_{MP}}{V_{OC}J_{SC}} \quad (26)$$

Figure 3-2 shows a visual representation of the concept of FF. The dotted line rectangle shows the maximum power that the cell could generate with everything being ideal, while the yellow rectangle shows the actual maximum power that the solar cell can give. The ratio between the area of these two rectangles is the FF and it is always between 0 and 1, being this last one the ideal behavior. It is usually given in % units, multiplying this last value by 100.

- R_S, Series Resistance: This resistance represents the losses mainly related with the contacts of the cell, and it can be estimated using the slope of the I-V curve around the V_{OC} point (Equation 27):

$$R_S = \left(\left.\frac{\delta I}{\delta V}\right|_{V\sim V_{OC}}\right)^{-1} \quad (27)$$

- R_{SH}, Shunt Resistance: This resistance represents the losses related with the bulk material and manufacturing defects that provides an alternate path to the current flow. Due to this diversion, not all the current can be extracted, part will be lost going through this resistor. Its value can be estimated using the slope of the I-V curve around the I_{SC} point (Equation 28):

$$R_{SH} = \left(\left.\frac{\delta I}{\delta V}\right|_{V\sim 0V}\right)^{-1} \quad (28)$$

- η, Power Conversion Efficiency (PCE): The parameter that summarizes everything. Only with this number the output (electric) vs input (optical) power is known, thus, the efficiency of the solar cell. Equation 29 shows how the rest of parameters are contained inside this parameter.

$$\eta = \frac{P_{out}}{P_{in}} = \frac{J_{MP}V_{MP}}{Irr\ [W/m^2]} = \frac{FFJ_{SC}V_{OC}}{Irr\ [W/m^2]} \quad (29)$$

To apply all these concepts, Figure 3-3 shows a I-V curve traced during the measurements of a MAPI solar cell fabricated in this work (Chapter 2). This cell was an average cell, with the most common values during my fabrication process. It is worth mentioning that the active area of this cell was of 0.118 cm^2.

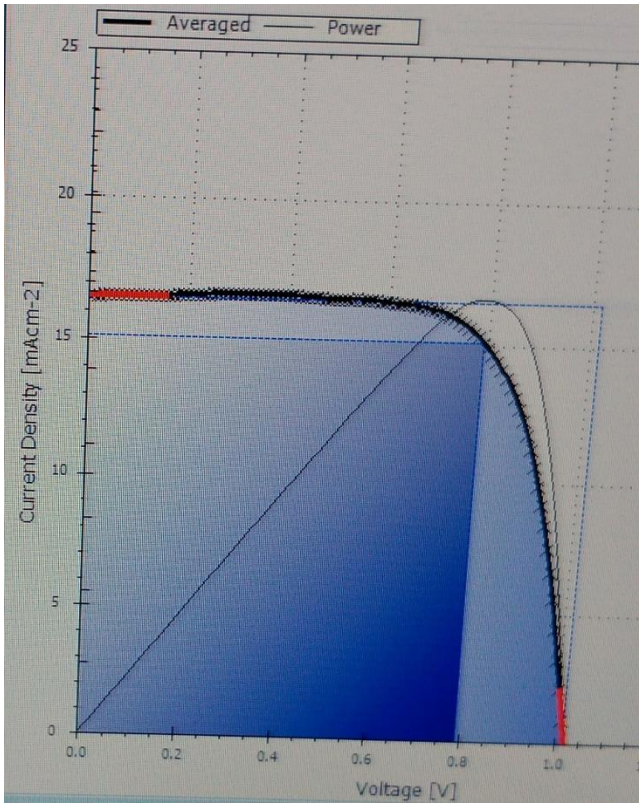

Figure 3-3 J-V curve of a MAPI solar cell sample.

Analyzing the curve, we can determine a J_{SC} of 16.52mA/cm^2, I_{SC} of 1.95mA, V_{OC} of 1.018V. Furthermore, the software traces the P-V curve, showing the maximum power point at V_{MP} of 793.34mV and I_{MP} of 1.78mA. With these values we can calculate the remaining ones using Equations 26 and 29, but this is usually automatically done by measurement software, obtaining FF of 71.25% and a PCE of 12%.

3.1.2. Quantum Efficiency Measurement

To look at the inner phenomena that occur in a solar cell, several measurements can be done. One of them is quantum efficiency. This value measures the relationship between the generated electrons and the incident photons. But, before going further, two concepts should be defined: internal and external quantum efficiency.

- External Quantum Efficiency (EQE): This value is obtained calculating the ratio between the generated electrons by the solar cell and the photons incident on it. Naturally, it varies depending on the incident light wavelength (a solar cell does not react in the same way against blue light that against red light, although ideally it should). Also depends on the material stack of the device and its optical behavior, due to the reflection and transmission of light through the different device layers.

- Internal Quantum Efficiency (IQE): This value relates the generated electrons with the **absorbed** photons. It is obtained correcting the EQE measurement, by discounting the transmission and reflection phenomena. That is why the IQE is always higher than the EQE.

Comparison between both values is crucial to analyze and improve the device, checking where are the bottlenecks in the generation process. If EQE is low but the IQE is very high, it can be stated that the optical behavior of the stack should be improved (the losses are mainly due to transmission and reflection). On the other hand, if EQE and IQE are very similar, we can remark an optimal optical behavior (both transmission and reflection will be almost 0). Finally, if the IQE it is low, improving the transmission and reflection will not make a difference, and internal properties of the absorber material should be optimized, such as the diffusion lengths, recombination processes and carrier mobilities. Figure 3-4 [4] shows EQE and IQE graphs of a crystalline silicon solar cell. In this example, the transmittance is 0, so the difference between EQE and IQE is given only by the reflectance.

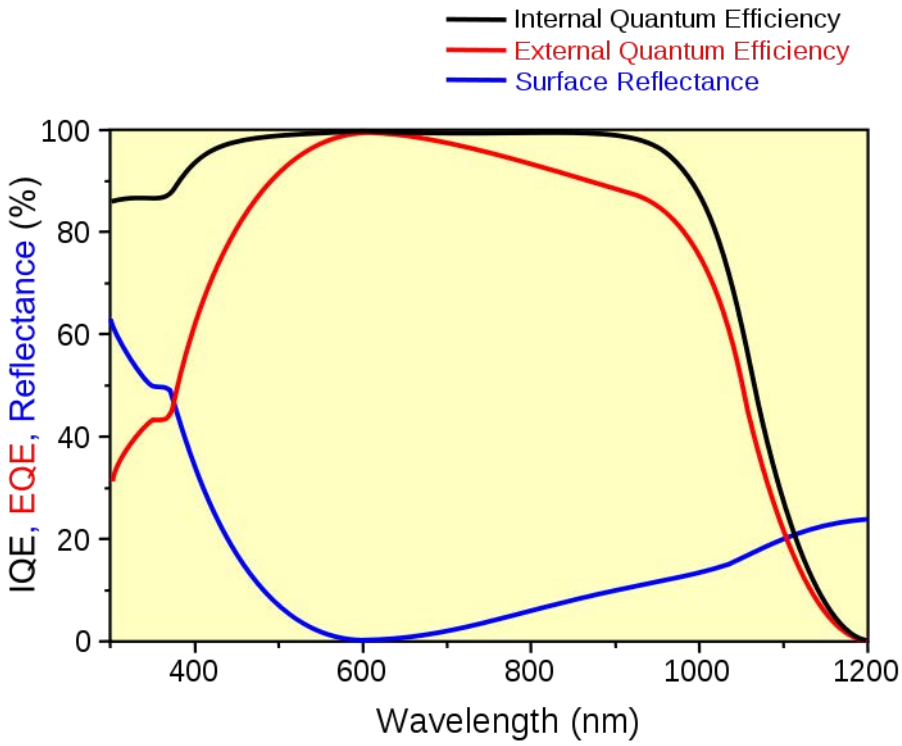

Figure 3-4 IQE and EQE graph of a crystalline silicon solar cell. ©Eric Bajart/CC-BY-SA-3.0 [4]

From EQE/IQE measurements, the bandgap of the material can be roughly estimated observing the longest wavelength that the material can absorb. With that value and applying Equation 30 the bandgap is estimated.

$$\lambda_{onset} = \frac{hc}{E_g} = \frac{1240\ [nm{\cdot}eV]}{E_g\ [eV]} \rightarrow E_g = \frac{1240\ [nm{\cdot}eV]}{\lambda_{onset}\ [nm]} \quad (30)$$

being h the Planck's constant, c the speed of light, λ_{onset} the longest absorbed wavelenght and E_g the bandgap of the material. In the example of Figure 3-4, this gives a result of 1.04eV. However, the bandgap of silicon is 1.1242eV [5], [6] so there is a

difference of around 0.08eV. This is understandable considering that silicon is an indirect bandgap semiconductor, so a photon with less energy than the bandgap can generate an electron-hole pair if it is pushed properly by a phonon of the lattice. Due to this fact, the c-Si solar cell is absorbing light up to 1200nm, instead of stopping at 1103nm (1.1242eV).

3.1.3. Impedance spectroscopy

The impedance spectroscopy technique is based on the analysis of the complex impedance (magnitude and phase) of the device under test. This impedance is defined following Ohm's law (Equation 31):

$$Z(\omega) = \frac{V(\omega,t)}{I(\omega,t)} = \frac{V_0 e^{i\omega t}}{I_0 e^{i(\omega t+\phi)}} = Z_0 e^{-i\phi} = R + iX \quad (31)$$

where Z stands for impedance in ohms, expressed by the ratio of voltage (V) and current (I), which are both time (t) and angular frequency ($\omega = 2\pi f$) dependent. ϕ represents the phase shift between voltage and current, R is the resistance and X is the reactance. So, the impedance of a device is a complex value which is also frequency dependent. The working principle of the impedance analyzer is the following: an AC signal is applied to the device. The user configures the applied voltage amplitude, the DC bias voltage (if any) and the frequency range of measurement. Then, the equipment will apply the voltage on the device and measure the current, computing the impedance. Some analyzers can also fix the current and measure the voltage, making the reverse process. As a rule of thumb, the AC voltage amplitude should be the highest value that is able to maintain the linearity of the circuit (i.e., no problem when measuring a resistor, because its behavior is linear, however if diode characteristics appear special care should be taken).

The typical output of this analysis is the impedance plot, which compares the imaginary vs the real impedance components, i.e., $-Z_{imag}(\omega)\ vs\ Z_{real}(\omega)$. Figure 3-5 shows an impedance plot measurement of an organic photodetector [7]. This impedance measurement can be adjusted to an equivalent electric circuit that emulates its behavior. The values of the components of this circuit can then be related with some physical properties of the device.

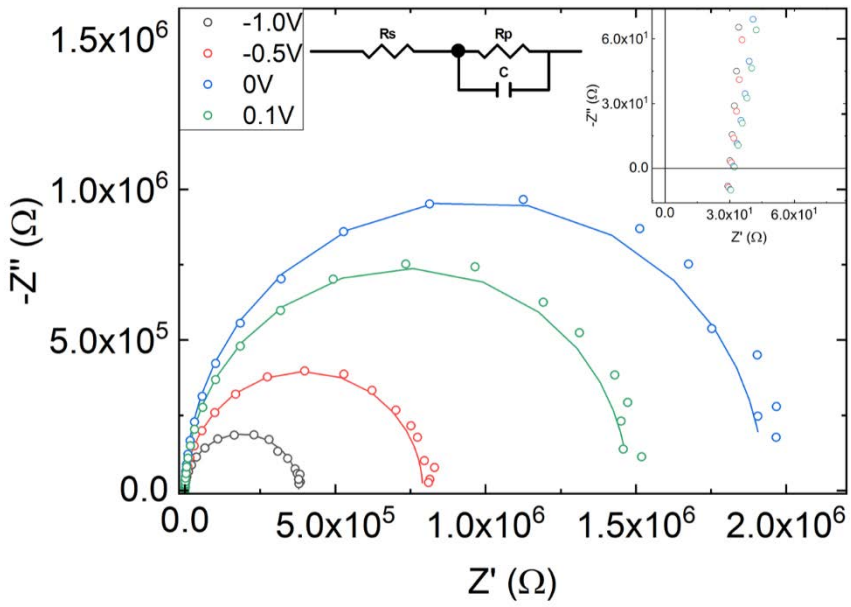

Figure 3-5 Impedance plot of an organic photodetector at different bias voltage and its computed equivalent circuit. Inset shows a detail of the high frequency zone [7].

Each dot represents an impedance measurement with certain steady state conditions (bias voltage, illumination, etc.) and frequency. The lines represent the fit of the impedance response of the equivalent circuit for each steady state configuration. But how can the equivalent circuit be estimated? In this case it is easy and almost unequivocal. In very low frequencies, almost DC (right side of the plot), the intersection with the real axis is search. This means that in low frequencies, the device acts as a resistor (reactance $X = 0$). Furthermore, in very high frequencies (left side of the plot) the curve also intersects with the real axis, so in high frequencies the device acts as a resistor too. In the mean path, the curve traces an arc, which is a sign of a process associated with a characteristic time. This kind of perfect semicircles are matched with an RC branch in the equivalent circuit. Thus, from this plot it is deduced the configuration of the equivalent circuit as a resistor R_s connected in series with a RC parallel branch (R_p and C, see inset in Figure 3-5). The relationship between the resistors and the plot are shown in the following equations:

$$R_s = Z^*(\omega \to \infty) \tag{32}$$

$$R_s + R_p = Z^*(\omega \to 0) \tag{33}$$

Finally, the capacitance is related with the characteristic relaxation time. This time is the reciprocal of the characteristic angular frequency, and it is the angular frequency for the point placed on the top of the semicircle. Then, applying Equation 34:

$$\omega_c = \frac{1}{\tau_c} = \frac{1}{R_p C} \to C = \frac{\tau_c}{R_p} = \frac{1}{\omega_c R_p} \tag{34}$$

For this example, it is depicted an $R_s = 30\ \Omega$ (it is remarkable that this series resistance is generated due to the physical contacts of the device, connections and wires going to the measurement system, so it does not change with bias voltage). Then $R_p = 1.9\ M\Omega$ and $C = 19\ nF$ for a bias voltage of 0V. All these electrical values can be related with physical properties of the device, such as recombination times, carrier lifetime, carrier mobility, dielectric constant, accumulation of charges in the contacts, etc.

In this section, the impedance spectroscopy and its adjustment using equivalent circuits has been explained. Notwithstanding, I want to stress that the selection of an equivalent circuit is not trivial, and it depends on the complexity of the measured impedance response. Actually, various equivalent circuit configurations can lead to the same impedance frequency response behavior. The right selection will come mainly from a deep understanding on the device under test and the researcher experience [8].

Detailed analysis for characterizing dye sensitized solar cells using this technique can be found at Chapter 12 of the book [9]. This analysis have been applied to a huge amount of technologies, such as silicon solar cells [10], organic solar cells [11]–[13], III-V solar cells [14], perovskite solar cells [15], [16] and emerging photovoltaics [17].

3.1.4. Mott-Schottky plot

The Mott-Schottky plot is a characterization technique that relates the capacitance generated by the depletion layer of a semiconductor with the potential difference along the bulk material. With this technique some physical parameters can be determined, such as the built-in potential or the doping density. The next set of equations will define the physics that relates the capacitance with the applied voltage in a p-n junction. In first place, the following definition of depletion width (w_D) is used[3]:

$$w_D = \sqrt{\frac{2\varepsilon}{q}\left(\frac{N_A+N_D}{N_A N_D}\right)\left(V_{bi} - V - \frac{2kT}{q}\right)} \tag{35}$$

being ε the electric permittivity of the material, q the electron charge, N_A the acceptor concentration on the p-type side, N_D the donor concentration on the n-type side, V_{bi} the built-in voltage of the space-charge region, V the applied voltage, k the Boltzmann constant and T the temperature. Due to the accumulation of charges in the depletion region, a capacitance is generated (Equation 36)

$$C = \frac{\varepsilon A}{w_D} \tag{36}$$

this capacitance is related with the depletion width through the electric permittivity (ε) and the area of the device (A). Thus, combining Equation 35 and 36:

$$\frac{1}{C^2} = \frac{2}{q\varepsilon A^2}\left[\left(\frac{N_A+N_D}{N_A N_D}\right)\left(V_{bi} - V - \frac{2kT}{q}\right)\right] \tag{37}$$

Equation 37 shows the foundation of the Mott-Schottky technique. This technique has been applied previously on silicon [18], perovskite [19] and even quantum dots solar cells [20]. As an example, I will give a Mott-Schottky test done in a GaAs solar cell during this work. This GaAs solar cell was obtained from a collaboration project with Universidad Politécnica de Madrid (UPM) [21], due to their expertise in the fabrication of III-V semiconductor devices. The initial data for this example comes from a previous impedance spectroscopy analysis (see section 3.1.3), so impedance vs frequency (1Hz to 1MHz) data at several bias voltage is already available.

First step is to convert the impedance into capacitance. This is done using Equation 38:

$$C^*(\omega) = \frac{1}{i\omega Z^*(\omega)} \tag{38}$$

being ω the angular frequency, $i = \sqrt{-1}$, $Z^*(\omega)$ the complex impedance as a function of angular frequency and $C^*(\omega)$ the complex capacitance as a function of angular frequency too. This value is analyzed under dark at 0V (i.e., no bias voltage). The real part of the complex capacitance against frequency is plotted in Figure 3-6.

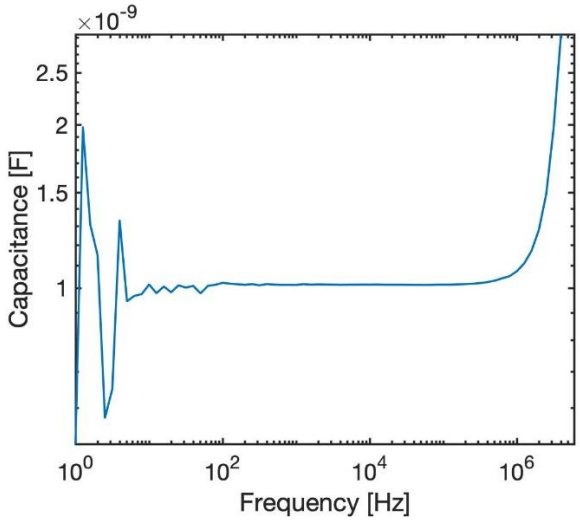

Figure 3-6 Real part of the complex capacitance as a function of frequency in GaAs solar cell.

In order to make the Mott-Schottky plot, we should select an operation frequency, in this case 10kHz. This selection is not arbitrary, 10kHz is the middle point of the "plateau" of almost constant capacitance (see Figure 3-6). Over 500kHz the exponential growth starts and under 100Hz the signal is too noisy. The next step is to analyze the capacitance vs applied voltage curve, at the previously selected frequency (10kHz). In the same graph, also the inverse of the capacitance squared is plotted (Figure 3-7).

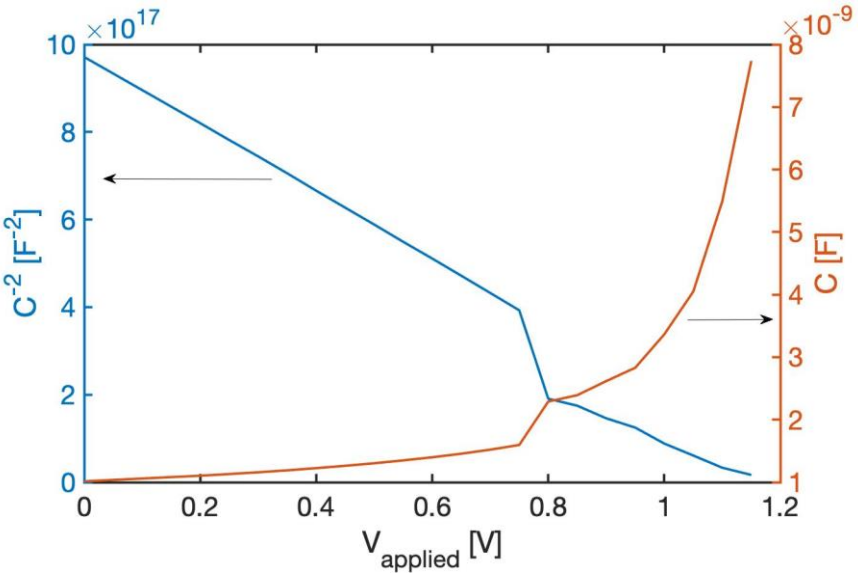

Figure 3-7 Mott-Schottky graph, showing the relationship between capacitance (right) and inverse of capacitance squared (left) vs applied voltage at 10kHz.

A strange point is observed at 0.8V, related to the start of the exponential growth (due to the high non-linearity of the device at that bias voltage), also matching the forward voltage characteristic of the equivalent diode. Therefore, we applied a linear fit to the zone between 0V and 0.6V, to obtain a linear relationship between C^{-2} and V. Then, relating this fit with Equation 37, the built-in voltage (V_{bi}) is obtained as the crossing with x-axis, i.e. 1.2654V. Furthermore, an estimation of the doping density can be obtained considering Equation 39 and combining it with Equation 37.

$$V_{bi} = \frac{kT}{q} \ln\left(\frac{N_D N_A}{n_i^2}\right) \tag{39}$$

where n_i is the intrinsic carrier density of the material and the rest of parameters were previously defined. Donor an acceptor density result in $1.2668 \cdot 10^{17}$ carriers per cubic centimeter, supposing an equal doping on both sides of the junction. These measurements are part of a study that is currently being developed.

3.2. Why a solar simulator?

All the methods explained in the previous section are very useful to extract several key properties of photodevices, but all of them have a common fact. They need a light excitation source, mainly a solar simulator. Unfortunately, at the beginning of this thesis, the research laboratory of Displays and Photonic Applications Group (GDAF-UC3M) did not have one, so a brand new one was developed from scratch. Along this section the main characteristics of a standard solar simulator are explained. After that, the concept of SUNBOX is introduced.

3.2.1. Solar simulators: Definition and state of the art

A solar simulator is a device capable of illuminating a well-defined area with the same power and spectral content that the Sun has. Naturally, due to the constant changes that sunlight suffers (translation and rotation of Earth, angle of incidence, climate conditions, etc.) this spectrum is determined by an international standard. To

recreate the conditions at the surface of the Earth, the AM1.5G standard, defined by the American Society for Testing and Materials (ASTM) and available at National Renewable Energy Laboratory (NREL) web page [22] is used. In AM1.5G the AM stands for Air Mass, which equals the number of atmospheres that the light passes to arrive at the surface of Earth. This value is related with the angle of incidence of the light, being at normal incidence ($\theta = 0°$) equivalent to Air Mass 1. Air Mass value is calculated using Equation 40.

$$Air\ Mass = \frac{1}{cos\theta} \tag{40}$$

being θ the angle of incidence (solar zenith angle). So, the standard AM1.5 means that the solar zenith angle equals to 48.19°. Furthermore, the atmosphere produces scattering and reflection phenomena that lead an amount of around 20% of light incident on a solar cell coming from indirect (diffuse) radiation [3]. Thus, AM1.5G stands for global radiation (direct + diffuse) while AM1.5D stands only for direct radiation. There is also another common standard, AM0, that stands for no air, so, it means extraterrestrial radiation, the one reaching to the top of the atmosphere. AM0 is usually used as a reference in space aircraft or satellite solar panels. Figure 3-8 shows the three mentioned spectra: AM0 (Etr), AM1.5G (Global) and AM1.5D (Direct + Circumsolar).

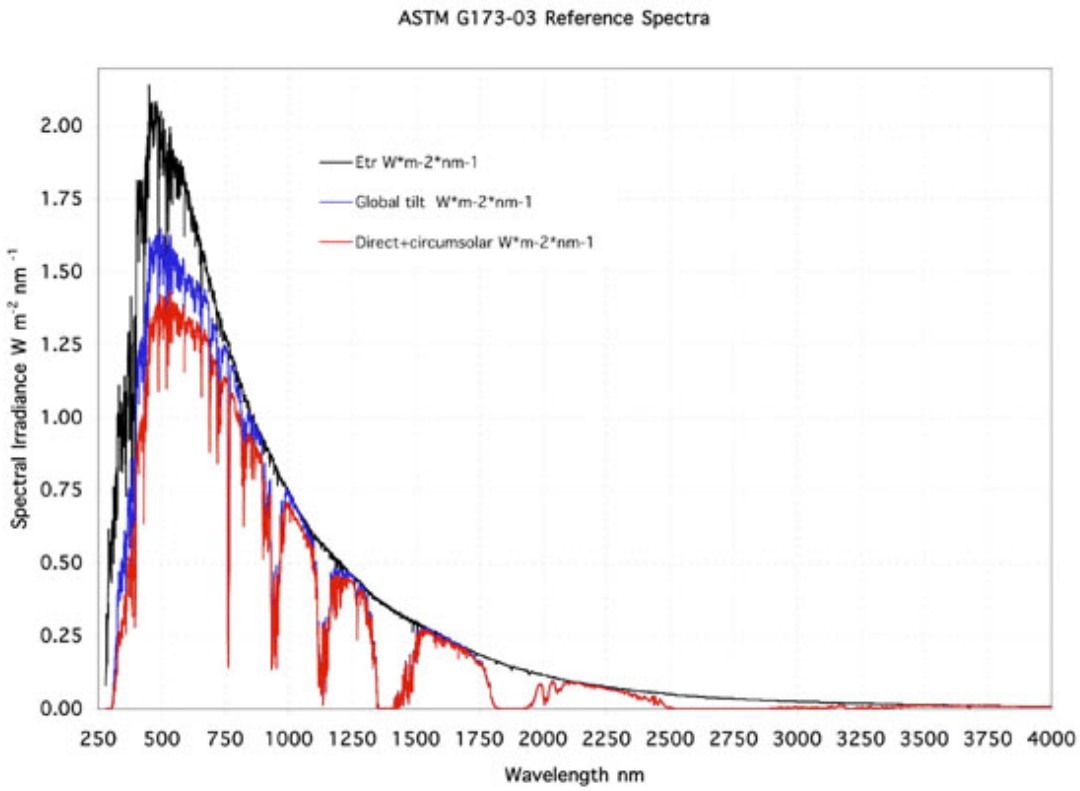

Figure 3-8 Standard spectra of AM0 (Black), AM1.5G (Blue) and AM1.5D (Red). Obtained from [22].

The applications of a solar simulator are almost countless, such as solar panels characterization under special conditions [23], testing of thermal collectors [24], testing

the effect of dew formation over solar panels [25] or calibration of other equipment, such as a spectroradiometer [26].

All the characteristics and requirements that a solar simulator must have are collected in the international standard IEC 60904-9:2007, which has both an European (EN 60904-9:2007) and Spanish equivalents (UNE-EN 60904-9:2008). One remarkable point of these standards is that they do not determine the light source technology that should be used [27]. Therefore, several technologies have been used, such as xenon short-arc and metal halide discharge lamps [28]–[30], fluorescent or Light Emitting Diodes (LED) lamps [31]. Notwithstanding, this last technology is gaining weight in the market versus the traditional xenon or discharge lamps, due to the advantages that LED technology has [32]:

- Optical power emitted by an LED can be easily tuned by the control of the electrical current crossing it with the right conditioning circuit, due to the almost linear relationship between these two parameters. On the contrary, xenon and discharge lamp optical power cannot be easily controlled.
- The temporal stability and lifetime of LED lamps is much higher than in xenon and discharge lamps, also they are more efficient and produce less heat, thus leading to less degradation of the electronic components. Therefore, their thermal management is not as exigent as in their counterparts.
- Finally, they can achieve a precise control of spectral selectivity if the selection of LEDs is wide enough. Instead of giving a continuous spectrum over the visible range, certain wavelengths can be selected to weight the spectral power in certain ways.

Due to all these factors, most current new illumination systems are driven through LEDs. There are a lot of studies that use LED-based solar simulators to characterize organic [33], [34] and inorganic [35] solar cells. Exploiting the spectral control that can be achieved on LED solar simulators the external quantum efficiency (EQE) can be determined [36] as well as some recombination processes [37].

Regarding the state of the art, there have been several approaches to build solar simulators at research level but there are a lot available in the market now also, each one with their own advantages and disadvantages. Some of them are briefly presented at Table 3-1:

Reference	Technology	LED types	Spectral interval	Illumination area	Optics
Krebs et al. [38]	LED	18	390-940nm	5 x 2.5 cm^2	Yes
Grandi et al. [39]	Halogen + LED	6	400->1100nm (Halogen)	10 x 10 cm^2	Yes
Stuckelberger et al. [40]	LED	11	400-750nm	18 x 18 cm^2	Yes
Plyta et al. [41]	LED	24	350-1300nm	32 x 32 cm^2	Yes
Novičkovas et al. [42]	LED	6	400-1000nm	6 x 6 cm^2	Yes
VeraSol-2 Newport	LED	19	400-1100nm	5.1 x 5.1 cm^2	Yes
LumiSun Innovation Optics	LED	-	400-1100nm	5 x 5 cm^2	Yes
Hyperion Greatcellsolar	LED	18	400-1100nm	12 x 12 cm^2	Yes

Table 3-1 Existing Solar Simulators Review.

It can be seen that each simulator can have its own application, depending on the illumination area, the spectral range, and the spectral intensity tunability (only some simulators are tunable). A common fact is that all of them need some kind of optics to manage the light in some way.

So, nowadays, commercial solar simulators are offered by several companies: xenon-based, discharge and fluorescent lamps, and LED-based. Some of them even mix technologies, using them for covering certain parts of the spectrum. Reviewing the scientific literature, several studies based on LED technology can be also found [43]–[46].

3.2.2. Need of a simulator like SUNBOX

Even though nowadays several LED-based solar simulators are available in the market (as seen at Table 3-1), they have several disadvantages that do not fit in our requirements:

- Most of the commercial simulators are made to set them statically in a place, so usually they are big and heavy. Notwithstanding, our design should be small and portable, to made experiments at different labs with different configurations.

- The price of the commercial simulators was prohibitive for our laboratory at that moment. That is why we also implemented the low-cost philosophy in our design, having in mind that any low-budget laboratory could acquire the resulting testing system.
- Regarding the mobility of the system, the optics that they need to work properly are a big disadvantage due to the necessity of calibration and fine tuning. Thus, we intend to develop a solar simulator without any kind of optics in its structure.

Summarizing all these facts we designed the idea of SUNBOX, a low-cost LED-based solar simulator, lightweight, portable, optics-free and classified with the highest performance ratings. Following sections will show in detail the methodology followed to get a commercial device from scratch.

This idea was published in Transaction and Instrumentation Measurement journal of IEEE [47]. Both software and hardware design of the system were also protected using an Utility model (Pub. Number ES1249534) and a software registry (Ref. Number M-005247/2019).

3.3. Design and modelling of SUNBOX

In this section the design of SUNBOX will be explained from scratch. First, initial calculations and optical design is exposed. Then, all the electronic conditioning is developed. These two parts are the foundation of SUNBOX and have the goal to achieve this main design requirements:

- Optics-free device: the selection, distribution and biasing of the LEDs will be crucial.
- AAA Class device under standard conditions: fulfilling all the conditions stated at IEC 60904-9:2007 and irradiating the surface with 1000 W/m^2.
- UV-extended range: due to the interest of analyzing some samples from 300nm-400nm, a spectral interval not included in the standard.
- Customizable emission: the system should not be limited to the solar spectrum, furthermore it should allow to customize the spectral content of the radiation.
- Low-cost, lightweight and portable.

3.3.1. Calculations and optical simulations

The optical design is the most complex part of SUNBOX, and it will be explained through all this section, starting from the theoretical basis, and then using MATLAB to do the optical simulations. All the equations shown in this section comes from the literature, mainly from the book *Light Measurement Handbook* of Alex Ryer [48].

One of the main calculations that should be done is, starting from the datasheet of a commercial LED, calculate the irradiance in W/m^2 that it will emit. Depending on the emission wavelength of the LED the data on the datasheet will be given in photometric (for visible spectrum LEDs) or radiometric units (IR and UV leds). The main difference between radiometric and photometric units is that the radiometric units are based in pure power units (watts) while the photometric units are weighted with the responsivity of the human eye (lumens). Figure 3-9 shows the weights that the photopic vision apply as a function of wavelength.

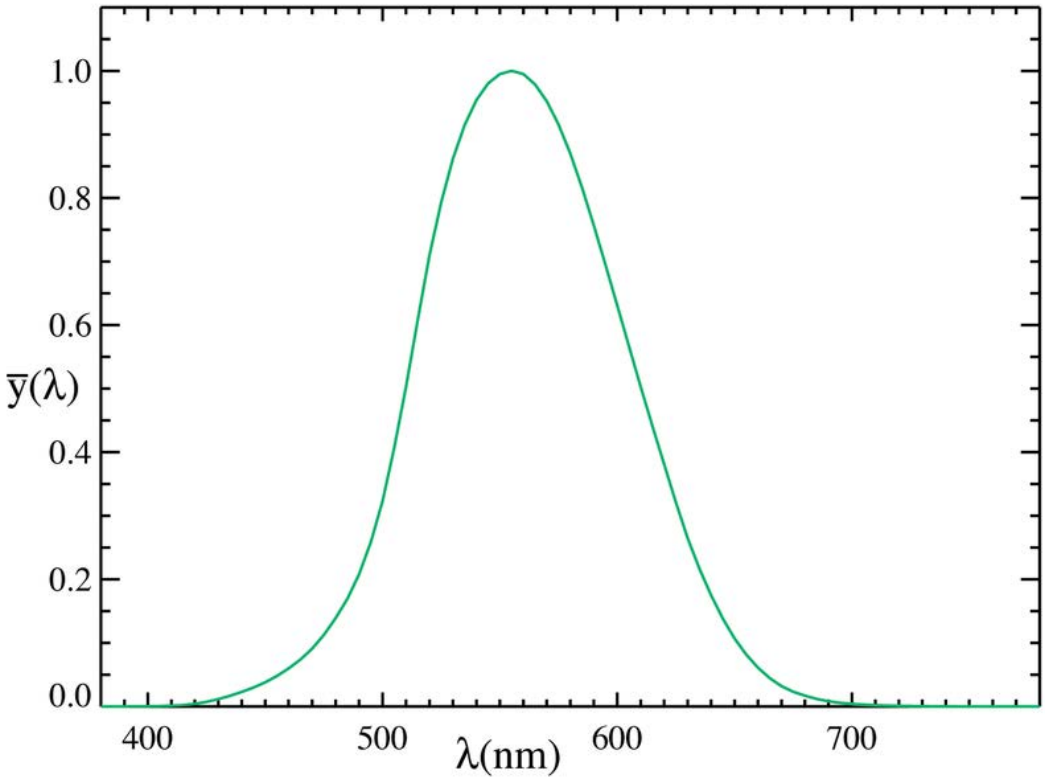

Figure 3-9 Relative photopic curve. Shows the weights that are assigned to each wavelength following the human eye responsivity. Obtained from [49]

The target value is the irradiance in W/m^2 (radiometric unit) so, in first place, photometric units should be converted to radiometric units in the visible LEDs. The maximum point of the photopic curve (and thus, the best responsivity of the human eye) is found at around 555 nm. At this wavelength, the conversion between radiometric and photometric is established as 683 lm/W. Due to the wavelength dependence, this curve is usually defined as $C(\lambda) = K \cdot V(\lambda)$ where K is the conversion constant of 683 lm/W, $V(\lambda)$ is the relative photopic curve (shown at Figure 3-9) and $C(\lambda)$ is the absolute photopic curve.

Working with a monochromatic source, like a laser, the conversion is very simple. The lumen value should be divided by the right conversion factor taken from the photopic curve at that wavelength. With that, the value is obtained in watts. However, in a non-monochromatic source it is not so simple, due to the power distribution in a broad spectral range. In those cases, Equation 41 should be applied:

$$\phi_{lm} = \int C(\lambda) \cdot \phi_W(\lambda) d\lambda \tag{41}$$

where ϕ_{lm} is the luminous flux (lm), $\phi_W(\lambda)$ is the spectral radiant flux (W/nm) and $C(\lambda)$ is the photopic curve (lm/W). This equation needs some expansion and new definitions to compute any radiometric unit from a photometric unit.

First, both radiant and luminous flux (ϕ) can be decomposed on a constant peak value (P) applied to the relative spectrum of the LED, $Rel(\lambda)$ (Equation 42).

$$\phi = \int \phi(\lambda) d\lambda = \int P \cdot Rel(\lambda) d\lambda = P \int Rel(\lambda) d\lambda \tag{42}$$

Using Equation 41 a relationship between both peak values can be established:

$$P_{lm} \int Rel(\lambda)\, d\lambda = P_W \cdot K \int V(\lambda) \cdot Rel(\lambda) d\lambda \quad (43)$$

Now, mixing Equations 42 and 43:

$$\phi_{lm} = \frac{\phi_W}{\int Rel(\lambda) d\lambda} \cdot K \int V(\lambda) \cdot Rel(\lambda) d\lambda \quad (44)$$

Finally, rearranging Equation 44:

$$\phi_W = \frac{\int Rel(\lambda) d\lambda}{K \int V(\lambda) \cdot Rel(\lambda) d\lambda} \cdot \phi_{lm} \quad (45)$$

Equation 45 allows the conversion between radiometric and photometric units from non-monochromatic sources. In this case, from luminous (lm) to radiant (W) flux and also from luminous (lm/sr) to radiant (W/sr) intensity.

At this point we can merge the calculations for both visible and invisible LEDs, because all the units will be radiometric from here. The datasheet usually gives one of these two values: radiant flux or radiant intensity. The calculations in each case will be the following:

- Radiant flux: Represents the amount of optical power emitted by the source in Watts. To get the irradiance value from here, first it is needed to convert it to radiant intensity, using Equation 46:

$$I_{rad} = \frac{\phi_{rad}}{\Omega} \quad (46)$$

  where I_{rad} is the radiant intensity in W/sr, ϕ_{rad} is the radiant flux in W and Ω the solid angle illuminated by the source in stereoradian (sr). An isotropic source emits the same amount of power over all directions, this means a solid angle of 4π stereoradians or a full sphere. In this case, all the LEDs used emit with a maximum angle of 90° from the normal so they emit over half of sphere, 2π stereoradians. From now on, radiant intensity will be used.
- Radiant intensity: Represents the optical power per solid angle emitted by the source in Watts per stereoradian. This value has a straightforward conversion to irradiance (the target value) using the Equation 47:

$$E = \frac{I_{rad}}{d^2} \quad (47)$$

  being E the irradiance in W/m^2, I_{rad} the radiant intensity in W/sr and d the distance from the source to the irradiated plane. This equation is known as the inverse square law and represents the quadratic dependence of the irradiance versus the distance.

So, at this moment, it is possible to take the optical data from the LEDs datasheets and convert the values into irradiance. The problem is that the sources are

not isotropic, so the emitted power depends on the output angle. I will refer to this dependence as $S(\alpha)$. That is why the output (α) and incident (β) angles should be considered (in this case both will be the same, because the irradiated surface will be normal to the emission of the source). For the sake of clarity, Figure 3-10 shows a schematic drawing of these parameters.

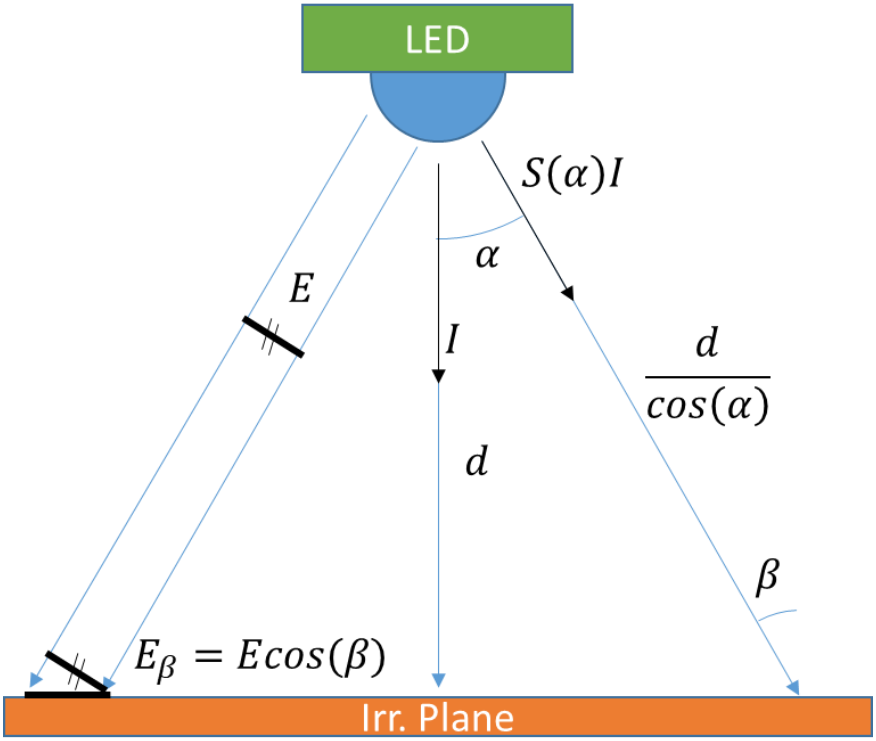

Figure 3-10 Schematic drawing of optical calculations.

This figure shows that several corrections should be done to previous equations. On one hand, the distance and radiant intensity mentioned in Equation 47 are both dependent on the output angle (right side of the figure), so it should be corrected as:

$$E = \frac{I_{rad} S(\alpha) \cos^2(\alpha)}{d^2} \tag{48}$$

On the other hand, the Lambert's cosine law should be applied in the irradiated plane (left side of the figure). This law is shown in Equation 49:

$$E_\beta = Ecos(\beta) \tag{49}$$

So, merging the Equations 48 and 49, and assuming that alpha equals to beta (emission plane and irradiated plane are parallel), the Equation 50 is obtained.

$$E_\beta = \frac{I_{rad} S(\alpha) \cos^2(\alpha) \cos(\beta)}{d^2} = \frac{I_{rad} S(\alpha) \cos^3(\alpha)}{d^2} \tag{50}$$

This equation is the main calculation that the MATLAB script will execute to determine the irradiance distribution over a plane depending on the LED parameters, the amount and distribution of LEDs and the distance to the irradiated plane.

Figure 3-11 left shows the $S(\alpha)$ parameter obtained from the datasheet while right shows the simulation of the same LED that MATLAB generated. This LED was placed at 5cm of the surface in this simulation and analyzed from 0 to 85 degrees of output angle, in steps of 5 degrees (this cause the effect of several concentric circles).

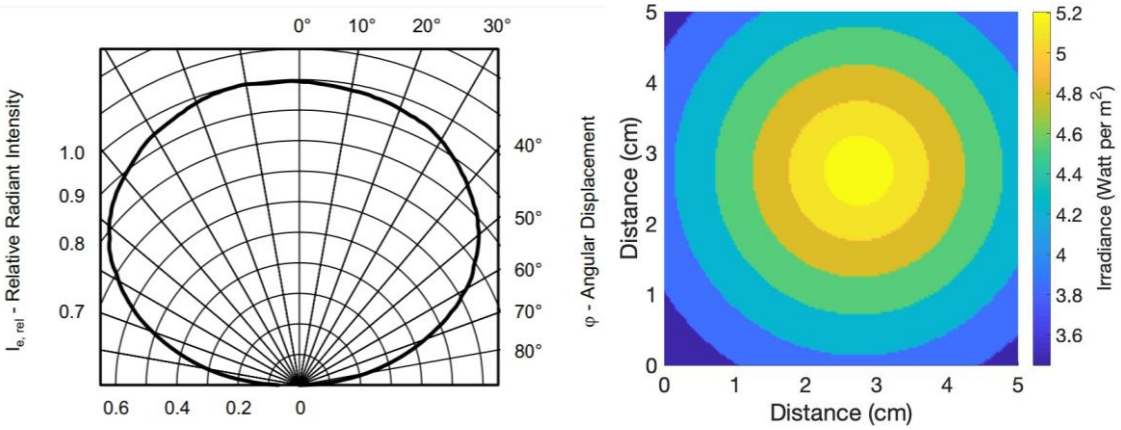

Figure 3-11 Relative Radiant Intensity vs Angle (left). Irradiance simulation of a single LED at 5cm of distance from the irradiated plane (right).

The simulation of multiple LEDs is done by adding the irradiance values, using a superposition principle. To be a realistic simulation, the LEDs could be distributed only at fixed positions. To do so, a 5 cm x 5 cm plane was divided into 100 points (10 by 10 grid) in such a way that each LED could be placed 5mm away from any other surrounding LED. Fixing a distance and leaving space between LEDs is crucial to make a realistic simulation, because the LEDs are not point sources, each one has its own packaging with its own size that must be considered.

After an iterative process, an LED distribution to achieve the fixed goal was found. Due to the intellectual property, the exact distribution of the LEDs cannot be revealed, but 34 LEDs of 14 different wavelengths were selected. The simulated results of this configuration are shown in Figure 3-12.

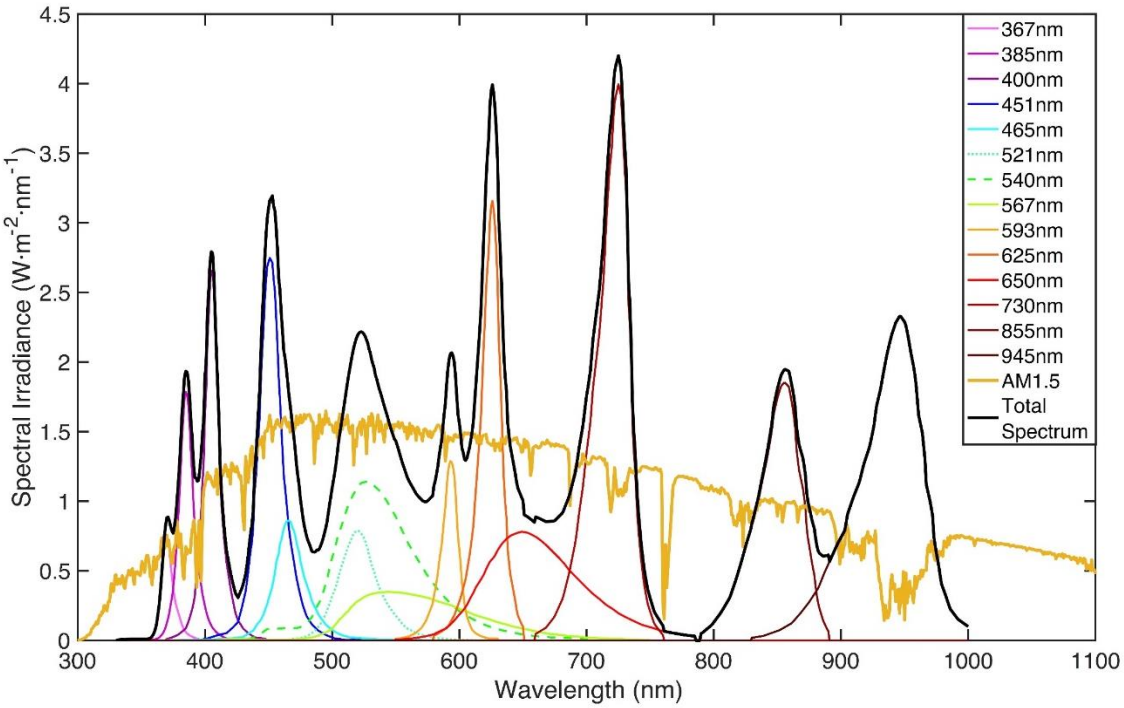

Figure 3-12 Spectral Irradiance of the selected LED distribution compared with AM1.5G spectrum.

Following sections will confirm that this LED distribution will match the standard with the best category possible (i.e., AAA Class).

3.3.2. Electronics and control design

Due to issues related to intellectual property protection, electronic design details cannot be given, but I will expose the general idea behind this design. The main goal is to control as precisely as possible, the optical power that LEDs will be giving. Furthermore, an individual control of each wavelength is required. That is why this design is based on a Voltage Controlled Current Source (VCCS) with an enable functionality in each wavelength that will allow to turn on and off the selected wavelenghts.

The core of this VCCS is a CC/CC Buck converter with an output current sense resistor, that is included into a feedback loop to make the output current equal to the control reference, that will be fixed and tuned in real time using the PC software.

The current control is selected because the optical power of a LED is linearly related with the current that is flowing through it, but not with the voltage (that has exponential dependence). This characteristic can be appreciated at Figure 3-13 (extracted from datasheet [50]).

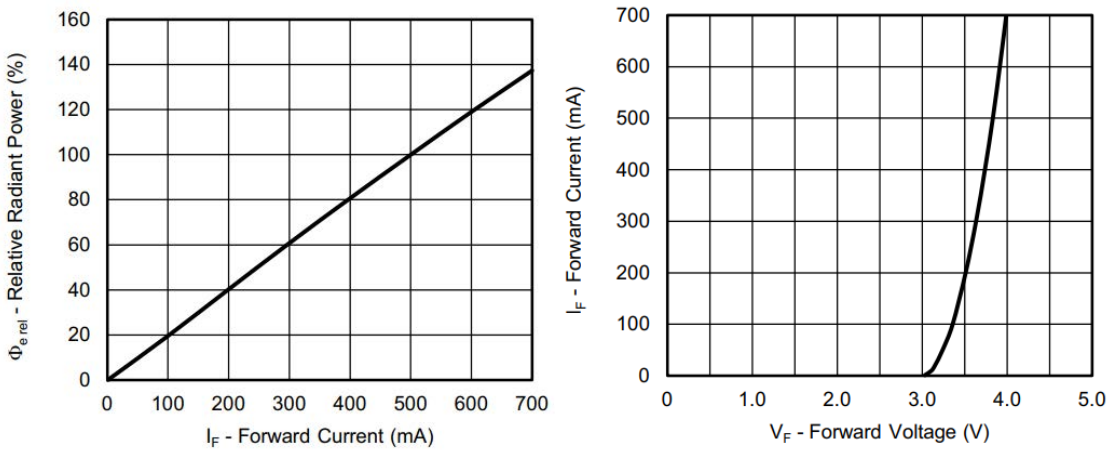

Figure 3-13 Optical power vs current through LED (left) and I-V curve of LED (right) [50].

It can be seen that the optical power can be adjusted in an accurate way controlling the current trough the LED. A voltage control will change the current in an exponential way, thus the optical emitted power. So, a current control must be applied. The enable feature is mandatory because a wavelength selection is needed too.

All the signals will be sent by a computer and will interface with the system through an Arduino MEGA [51] programmed with LabVIEW using its LINX extension [52]. This is a proprietary software that is also protected. A schematic is shown in Figure 3-14.

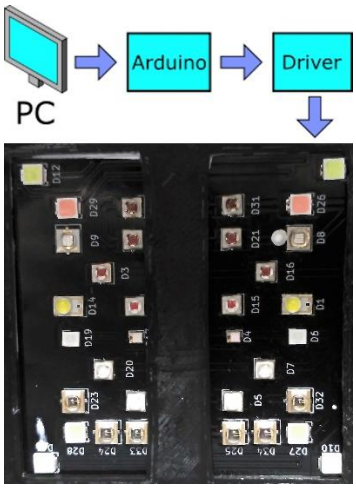

Figure 3-14 Connection schematic between computer and current control of LEDs. The LEDs PCB is also shown.

All the signals are configured in the computer using an intuitive interface programmed in LabVIEW and sent to Arduino (see Figure 3-15). Then Arduino manages the drivers using voltage signals to control the current through each group of LEDs.

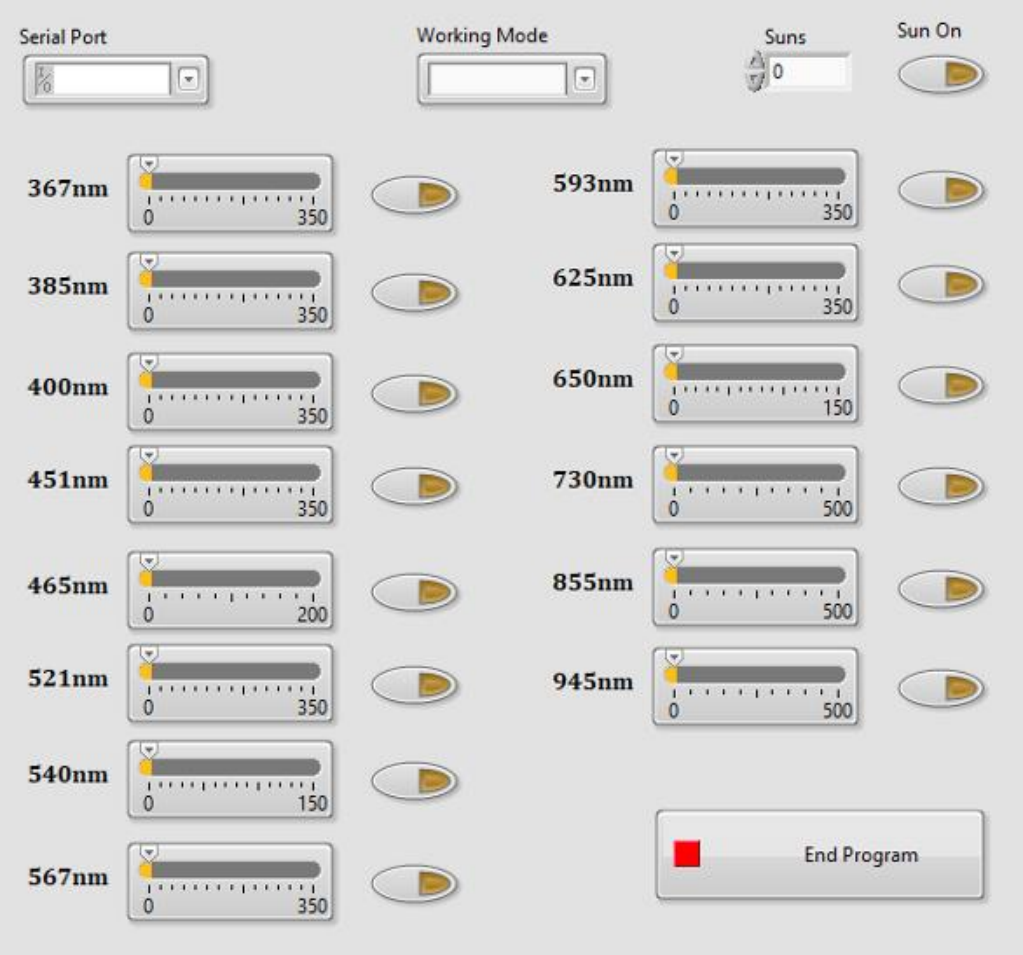

Figure 3-15 Graphical User Interface (GUI) to control SUNBOX.

Each slider controls the current that will flow through each group of LEDs (wavelength) and the button will activate the same group. This is how the custom mode works, but the software also has a calibrated “sun” mode, in which the desired number of suns can be selected (e.g., 0.65 suns). “Sun” mode is achieved after the calibration process explained in the calibration section.

3.4. Construction and testing

After the simulations that distributed the LEDs and the electronic conditioning, 3 main parts exist on SUNBOX: Control/PC Interface (Arduino), Power electronics (Drivers) and Optics board (LEDs). In order to achieve a compact design, a stackable arrangement was selected. This stackable rack is shown at Figure 3-16. This shape was selected due to the portability that it provides. It is also easy splitable in sections, making it ideal for 3D printing fabrication and modularity. The three “floors” of the design can be easily connected with special cables that allow the communication between boards. Moreover, an USB connector is used to join the system with the control PC.

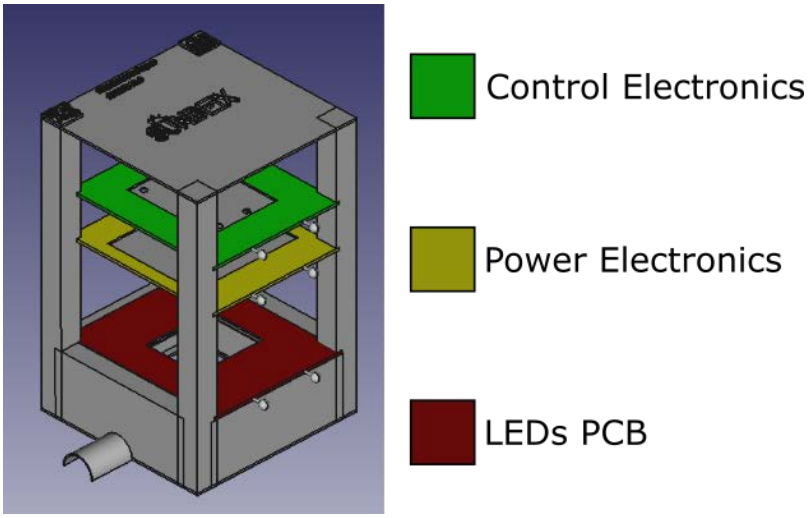

Figure 3-16 CAD model of SUNBOX. Three layers are differentiated: Control (Arduino), Power (Drivers) and LED PCB.

The sample chamber is also 3D printed, and its goal is to avoid that any kind of stray light can imping in the sample under test, disturbing the measurements (see Figure 3-17 left). However, the walls of the chamber can reflect the light also causing a distortion. To check this, the reflectance of the chamber was measured at several points. The results of the reflectance measurement are shown at Figure 3-17 (right). It can be stated that the PLA 3D printed sample chamber can perform successfully with a reflectance below 3% in the visible range. Moreover, these measurements are made perpendicular to the surface. As more than one reflection are needed to reach the sample, the real value of the possible reflected light reaching the sample is under 1%.

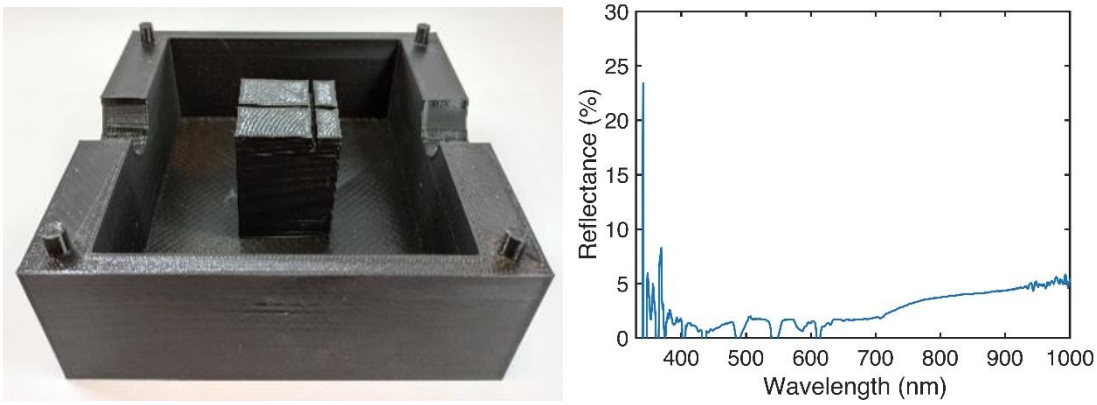

Figure 3-17 Sample chamber of SUNBOX (left) and reflectance measurement of black PLA plastic used for 3D printing the rack (right).

The last phenomena that should be considered is the thermal management of the system. Drivers were designed with an efficiency over 90%, so they will produce almost no heat. Notwithstanding, the efficiency of the LEDs is around 70% in the best case, so the LED PCB will produce heat that should be dissipated to avoid further damage in the system. The thermal management system implemented consist of a metallic heat sink contacted with a thermal sheet over the LED PCB and a 12V fan to make a forced ventilation system, allowing the LEDs to stay at low temperatures and avoiding any kind of thermal drift or damage. With this system, under full sun (1000W/m^2) irradiation, the LED PCB stabilizes around 40°C. A picture of the final system can be seen at Figure 3-18.

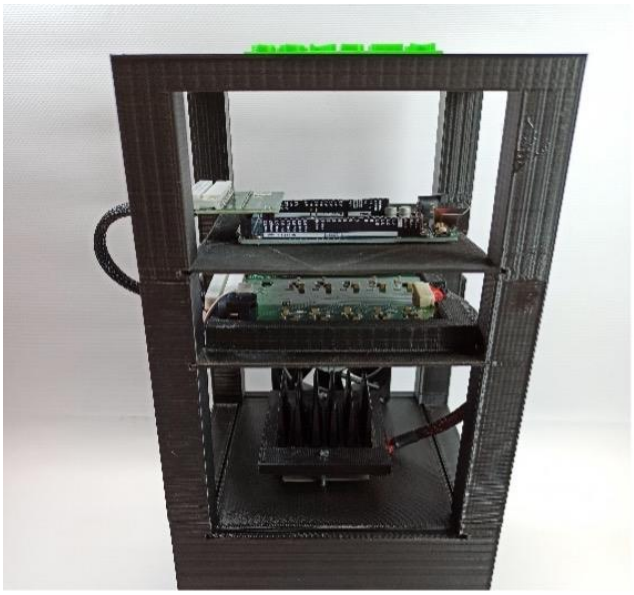

Figure 3-18 Picture of a built SUNBOX.

3.5. Calibration following a standard

Once the full device is mounted, a careful calibration following the standard (IEC 60904-9:2007) should be done. To fulfill the standard, mainly three parameters should be checked: Spectral Match, Homogeneity and Temporal Stability. All these measurements were acquired using the following setup:

- Ocean Optics' Cosine Corrector CC-3-UV-S [53], coupled to an optical fiber to collect light from 180° field of view (FOV). This is a cheap and useful way to have great light collection at a certain point. This will act as a light probe.
- Optical fiber QP400-1-VIS-NIR [54], used to transmit the light from the cosine corrector to the spectrometer.
- Spectrometer USB2000+ [55] from OceanOptics (nowadays OceanInsight). It will spectrally split and detect the light and analyze it, plotting it through the computer using SpectraSuite software.

This setup gives only relative values, but using a calibration lamp (HL-3P-CAL [56]) an absolute spectral irradiance measurement can be done (this measurement is used through all the calibration process).

Moreover, the total irradiance was measured also using a calibrated testing solar cell (Oriel 91150V [57]), and tuning the spectral power distribution of the SUNBOX system until 1 sun was achieved. Figure 3-19 shows one of the first measurements during the calibration process (little lower than a sun).

Figure 3-19 SUNBOX Irradiance measurement (0.995 suns) using Oriel 91150V.

3.5.1. Spectral Match

The spectral match measurement consists of determining the amount of light emitted by SUNBOX in each one of the following six spectral intervals: 400-500nm, 500-600nm, 600-700nm, 700-800nm, 800-900nm and 900-1100nm. In order to do so, first the total irradiance between 400-1100nm should be determined. The measurements were taken at the center of the irradiated plane with the setup previously exposed, and the ratios were calculated using Equation 51.

$$SMR = \frac{\int_{\lambda_1}^{\lambda_2} F(\lambda)d\lambda}{\int_{400nm}^{1100nm} F(\lambda)d\lambda} \cdot 100\ [\%] \tag{51}$$

being SMR the Spectral Match Ratio, λ_1 and λ_2 the beginning and end wavelengths of the interval of interest and $F(\lambda)$ the spectral irradiance in W/m^{2}nm units. *Table 3-2* shows the calibrated values of the first SUNBOX.

Spectral Interval	Irradiance (W/m^2)	SMR	Target Value (SMR)	Deviation	Class
400-500nm	172	20%	18.4%	+8.7%	**A**
500-600nm	155	18%	19.9%	-9.5%	**A**
600-700nm	153	18%	18.4%	-2.2%	**A**
700-800nm	130	15%	14.9%	+0.6%	**A**
800-900nm	107	13%	12.5%	+4%	**A**
900-1100nm	137	16%	15.9%	+0.6%	**A**

Table 3-2 Spectral Match calibration test. Highest class is achieved.

This adjustment is done weighting the currents that flow through each group of LEDs. It can be seen that all the deviations are far below 25%, thus giving SUNBOX the maximum quality class A regarding the spectral match category.

3.5.2. Homogeneity

The homogeneity rating gives how even is the distribution of light over the irradiated plane, being a Class A below 2%, Class B below 5% and Class C below 10%. Using LEDs as light sources and without any kind of optics that allow evenly distributed light, this is the most difficult rating to achieve.

Several points around the irradiated plane were measured and then the minimum and maximum irradiance values were extracted and introduced in Equation 52.

$$Non - uniformity = \frac{I_{MAX} - I_{MIN}}{I_{MAX} + I_{MIN}} \cdot 100\ [\%] \quad (52)$$

Furthermore, an experimental irradiance plot, built by interpolation over the above mentioned measured points, was also traced to show the uniformity and homogeneity of light using SUNBOX. This plot is shown in Figure 3-20. With the measurements taken it can be confirmed that SUNBOX has a Class A in terms of homogeneity taking an area of 1cm^2 around the center point.

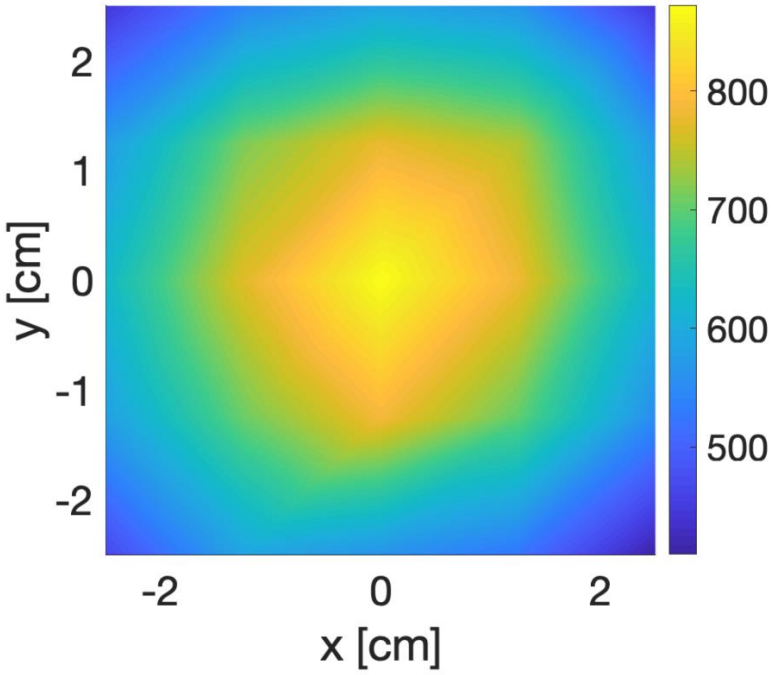

Figure 3-20 Homogeneity map of SUNBOX in W/m^2, showing the uniformity of light distribution.

3.5.3. Temporal Stability

This parameter defines how stable is the light source both in short- and long-term measurements. This is a crucial parameter, specially in studies that run for a day, because the irradiation level must be maintained as constant as possible for 24 hours. Fortunately, LED light is intrinsically stable, specially compared to the typical technologies in solar simulators such as halogen or arc discharge lamps. To check this parameter, the irradiance at center point of the irradiated plane is monitored for a fixed period of time. For Short Term Instability, a measurement is taken every 100ms for 1s. In Long Term Instability the sample was taken every 10s during 300s. Those time intervals are determined following the standard. The maximum and minimum values are taken and introduced in Equation 53.

$$STI\ or\ LTI = \frac{I_{MAX} - I_{MIN}}{I_{MAX} + I_{MIN}} \cdot 100\ [\%] \quad (53)$$

Table 3-3 shows the results obtained for both STI and LTI measurements. It is worth mentioning that with a very small warm-up time (around one minute), SUNBOX achieves the maximum quality rating, compared with the typical 30 minutes in classical solar simulators [58].

	No warm-up	Class	60s Warm-up	Class
STI (%)	1.5218	**B**	0.1586	**A**
LTI (%)	3.5768	**B**	0.8979	**A**

Table 3-3 Short- and Long-Term Instability values measurements of SUNBOX. After one minute of warm-up, it achieves the highest quality (Class A).

3.6. SUNBOX Application note: solar cells characterization exploiting spectral selectivity

Throughout this section an analysis of a solar cell using SUNBOX is exposed. This is an interesting example, due to the use of several functionalities of the solar simulator. The information exposed along this section is based on the article published at ACS Applied Energy Materials [13], but the procedure can be followed working with any kind of technology. In this study, several samples of organic solar cells were analyzed. These cells were based on PBDB-T:ITIC blend as an active layer, using PEDOT:PSS and ZnO as extraction layers. As a summary, I will give a series of steps that can be followed to fully exploit the properties and capabilities of SUNBOX:

1. Taking an I-V or J-V curve: Here, SUNBOX is set to "Sun mode" with 1 sun of value. After that the I-V curve is measured on dark and under light. Both measurements can be taken quickly, the second one just after clicking only one button, due to the almost no-warm up time required to stabilize SUNBOX. From here the fundamental parameters of the solar cell are obtained (check Section 3.1.1.)
2. Doing an impedance analysis: Using the same configuration but changing the measurement equipment (an impedance analyzer instead of an I-V tracer), an impedance spectroscopy measurement (see Section 3.1.3.) can be done in dark and under 1 sun conditions. Moreover, the "dimming sun" functionality can be used, making the analysis using fractions of suns, such as 0.1, 0.25 or 0.6 suns. This can create a different response and help us to analyze and understand the dynamics of the physical process of these cells. The Mott-Schottky plot can also be traced taking the impedance measurements as the starting point (see Section 3.1.4.)
3. Tracing a spectral analysis: Here, using "custom mode", individual wavelengths can be controlled and dimmed with the objective of checking the spectral behavior of the device. In the mentioned study, the cell was analyzed using red (630nm), blue (450nm), and white light. Making these spectral selective measurements, parameters like the External Quantum Efficiency (EQE, see Section 3.1.2.) can be estimated. Checking the variation of the open circuit voltage versus the illumination intensity, the ideality factors of the cells could be obtained too. Moreover, the absorption depth inside the device was analyzed. Indeed, blue photons were absorbed in the bulk material (active layer) while red ones were absorbed near the anode

contact. Due to the degradation of the cells, the ideality factor suffered a change under red light, but was constant under blue light. So, combining the obtained ideality factors and the different penetration depths of each wavelength in pristine and aged samples, we concluded that the degradation affected mainly to the zone near the anode.

4. Making a thermal analysis: Due to the SUNBOX modularity, a hot/cold stage TS102GXY [59] by Instec could be placed at the sample area, introducing the capability of fixing the temperature of the sample in dark and under a custom illumination spectrum. From this thermal analysis the V_{OC} drift due to temperature change can be obtained, and, in this case, the activation energy of the recombination process.

It has been demonstrated that all the previous measurements can be obtained using SUNBOX and its modularity allows the implementation of complex system (e.g., using a thermal stage, a testing cell reference, or a spectrometer). Furthermore, as a future work we want to expand its capabilities, giving it the possibility to measure I-V curves standalone, exciting the samples with pulsed light or augmenting the spectral range in ultraviolet and infrared.

3.7. Bibliography

[1] H. Sharma, N. Pal, Y. Singh, and P. Sadhu, "Development and Simulation of Stand Alone Photovoltaic Model Using Matlab/Simulink," *International Journal of Power Electronics and Drive Systems (IJPEDS)*, vol. 6, pp. 703–711, Dec. 2015, doi: 10.11591/ijpeds.v6.i4.pp703-711.

[2] "Solar Cells: A Guide to Theory and Measurement," *Ossila*. https://www.ossila.com/pages/solar-cells-theory (accessed Feb. 08, 2021).

[3] "Handbook of Photovoltaic Science and Engineering, 2nd Edition | Wiley," *Wiley.com*. https://www.wiley.com/en-us/Handbook+of+Photovoltaic+Science+and+Engineering%2C+2nd+Edition-p-9780470721698 (accessed Feb. 05, 2021).

[4] S. png : Q. work : E. Bajart, *English: Internal Quantum Efficiency, External Quantum Efficiency and reflecatnce of a crystalline silicon solar cell with antireflective coating.* 2010.

[5] Sproul, M. A. Green, and J. Zhao, "Improved value for the silicon intrinsic carrier concentration at 300 K," *Applied Physics Letters*, vol. 57, p. 255, 1990, doi: 10.1063/1.103707.

[6] Sproul and M. A. Green, "Improved value for the silicon intrinsic carrier concentration from 275 to 375 K," *Journal of Applied Physics*, vol. 70, pp. 846–854, 1991, doi: 10.1063/1.349645.

[7] C. Vega-Colado *et al.*, "An All-Organic Flexible Visible Light Communication System," *Sensors*, vol. 18, no. 9, Art. no. 9, Sep. 2018, doi: 10.3390/s18093045.

[8] "Impedance Spectroscopy: Theory, Experiment, and Applications, 2nd Edition | Wiley," *Wiley.com*. https://www.wiley.com/en-us/Impedance+Spectroscopy%3A+Theory%2C+Experiment%2C+and+Applications%2C+2nd+Edition-p-9780471647492 (accessed Feb. 17, 2021).

[9] "Dye-sensitized Solar Cells | Taylor & Francis Group," *Taylor & Francis*. https://www.taylorfrancis.com/books/dye-sensitized-solar-cells-kuppuswamy-kalyanasundaram/e/10.1201/b16409 (accessed Feb. 17, 2021).

[10] P. Yadav, K. Pandey, V. Bhatt, M. Kumar, and J. Kim, “Critical aspects of impedance spectroscopy in silicon solar cell characterization: A review,” *Renewable and Sustainable Energy Reviews*, vol. 76, pp. 1562–1578, Sep. 2017, doi: 10.1016/j.rser.2016.11.205.

[11] M. Knipper, J. Parisi, K. Coakley, C. Waldauf, C. J. Brabec, and V. Dyakonov, “Impedance Spectroscopy on Polymer-Fullerene Solar Cells,” *Zeitschrift für Naturforschung A*, vol. 62, no. 9, pp. 490–494, Sep. 2007, doi: 10.1515/zna-2007-0904.

[12] “Organic tandem solar cells: How impedance analyses can improve the quality of external quantum efficiency measurements - Bahro - 2018 - Progress in Photovoltaics: Research and Applications - Wiley Online Library.” https://onlinelibrary.wiley.com/doi/abs/10.1002/pip.3015 (accessed Feb. 17, 2021).

[13] B. Arredondo *et al.*, “Identification of Degradation Mechanisms in Slot-Die-Coated Nonfullerene ITO-Free Organic Solar Cells Using Different Illumination Spectra,” *ACS Appl. Energy Mater.*, vol. 3, no. 7, pp. 6476–6485, Jul. 2020, doi: 10.1021/acsaem.0c00711.

[14] R. A. Kumar, M. S. Suresh, and J. Nagaraju, “Measurement of AC parameters of gallium arsenide (GaAs/Ge) solar cell by impedance spectroscopy,” *IEEE Transactions on Electron Devices*, vol. 48, no. 9, pp. 2177–2179, Sep. 2001, doi: 10.1109/16.944213.

[15] L. Contreras-Bernal *et al.*, “Impedance analysis of perovskite solar cells: a case study,” *J. Mater. Chem. A*, vol. 7, no. 19, pp. 12191–12200, May 2019, doi: 10.1039/C9TA02808K.

[16] E. Ghahremanirad, A. Bou, S. Olyaee, and J. Bisquert, “Inductive Loop in the Impedance Response of Perovskite Solar Cells Explained by Surface Polarization Model,” *J. Phys. Chem. Lett.*, vol. 8, no. 7, pp. 1402–1406, Apr. 2017, doi: 10.1021/acs.jpclett.7b00415.

[17] E. von Hauff, “Impedance Spectroscopy for Emerging Photovoltaics,” *J. Phys. Chem. C*, vol. 123, no. 18, pp. 11329–11346, May 2019, doi: 10.1021/acs.jpcc.9b00892.

[18] I. Mora-Seró, G. Garcia-Belmonte, P. P. Boix, M. A. Vázquez, and J. Bisquert, “Impedance spectroscopy characterisation of highly efficient silicon solar cells under different light illumination intensities,” *Energy Environ. Sci.*, vol. 2, no. 6, pp. 678–686, Jun. 2009, doi: 10.1039/B812468J.

[19] O. Almora, C. Aranda, E. Mas-Marzá, and G. Garcia-Belmonte, “On Mott-Schottky analysis interpretation of capacitance measurements in organometal perovskite solar cells,” *Appl. Phys. Lett.*, vol. 109, no. 17, p. 173903, Oct. 2016, doi: 10.1063/1.4966127.

[20] S. M. Willis, C. Cheng, H. E. Assender, and A. A. R. Watt, “Modified Mott-Schottky Analysis of Nanocrystal Solar Cells,” *arXiv:1112.1623 [cond-mat]*, Dec. 2011, Accessed: Feb. 12, 2021. [Online]. Available: http://arxiv.org/abs/1112.1623.

[21] “Universidad Politécnica de Madrid.” https://www.upm.es/UPM/SalaPrensa/Noticias_de_investigacion?id=fa92fe66e8679610VgnVCM10000009c7648a____&fmt=detail&prefmt=articulo (accessed Apr. 27, 2021).

[22] “Reference Air Mass 1.5 Spectra.” https://www.nrel.gov/grid/solar-resource/spectra-am1.5.html (accessed Feb. 05, 2021).
[23] N. Thomas *et al.*, “A wide-beam continuous solar simulator for simulating the solar flux at the orbit of Mercury,” *Meas. Sci. Technol.*, vol. 22, no. 6, p. 065903, May 2011, doi: 10.1088/0957-0233/22/6/065903.
[24] R. W. Moss, G. S. F. Shire, P. C. Eames, P. Henshall, T. Hyde, and F. Arya, “Design and commissioning of a virtual image solar simulator for testing thermal collectors,” *Solar Energy*, vol. 159, pp. 234–242, Jan. 2018, doi: 10.1016/j.solener.2017.10.044.
[25] S. A. Hosseini, A. M. Kermani, and A. Arabhosseini, “Experimental study of the dew formation effect on the performance of photovoltaic modules,” *Renewable Energy*, vol. 130, pp. 352–359, Jan. 2019, doi: 10.1016/j.renene.2018.06.063.
[26] R. Galleano, I. Kröger, F. Plag, S. Winter, and H. Müllejans, “Traceable spectral irradiance measurements in photovoltaics: Results of the PTB and JRC spectroradiometer comparison using different light sources,” *Measurement*, vol. 124, pp. 549–559, Aug. 2018, doi: 10.1016/j.measurement.2017.09.007.
[27] V. Esen, Ş. Sağlam, and B. Oral, “Light sources of solar simulators for photovoltaic devices: A review,” *Renewable and Sustainable Energy Reviews*, vol. 77, pp. 1240–1250, Sep. 2017, doi: 10.1016/j.rser.2017.03.062.
[28] M. Pravettoni, R. Galleano, E. D. Dunlop, and R. P. Kenny, “Characterization of a pulsed solar simulator for concentrator photovoltaic cell calibration,” *Meas. Sci. Technol.*, vol. 21, no. 11, p. 115901, Sep. 2010, doi: 10.1088/0957-0233/21/11/115901.
[29] R. Gill, E. Bush, P. Haueter, and P. Loutzenhiser, “Characterization of a 6 kW high-flux solar simulator with an array of xenon arc lamps capable of concentrations of nearly 5000 suns,” *Review of Scientific Instruments*, vol. 86, no. 12, p. 125107, Dec. 2015, doi: 10.1063/1.4936976.
[30] C. Domínguez, I. Antón, and G. Sala, “Solar simulator for concentrator photovoltaic systems,” *Opt. Express, OE*, vol. 16, no. 19, pp. 14894–14901, Sep. 2008, doi: 10.1364/OE.16.014894.
[31] D. Kolberg, F. Schubert, N. Lontke, A. Zwigart, and D. M. Spinner, “Development of tunable close match LED solar simulator with extended spectral range to UV and IR,” *Energy Procedia*, vol. 8, pp. 100–105, Jan. 2011, doi: 10.1016/j.egypro.2011.06.109.
[32] G. Leary, G. Switzer, G. Kuntz, and T. Kaiser, “Comparison of xenon lamp-based and led-based solar simulators,” in *2016 IEEE 43rd Photovoltaic Specialists Conference (PVSC)*, Jun. 2016, pp. 3062–3067, doi: 10.1109/PVSC.2016.7750227.
[33] L. Cojocaru *et al.*, “Determination of unique power conversion efficiency of solar cell showing hysteresis in the I-V curve under various light intensities,” *Scientific Reports*, vol. 7, no. 1, Art. no. 1, Sep. 2017, doi: 10.1038/s41598-017-10953-3.
[34] L. N. Inasaridze *et al.*, “Light-induced generation of free radicals by fullerene derivatives: an important degradation pathway in organic photovoltaics?,” *J. Mater. Chem. A*, vol. 5, no. 17, pp. 8044–8050, May 2017, doi: 10.1039/C7TA00175D.
[35] J. Shao *et al.*, “The investigation on hydrogenation platform for silicon solar cells based on high intensity infrared LEDs,” *Journal of Renewable and Sustainable Energy*, vol. 10, no. 1, p. 013507, Jan. 2018, doi: 10.1063/1.5012781.

[36] T. Luka, S. Eiternick, and M. Turek, “Rapid Testing of External Quantum Efficiency using LED Solar Simulators,” *Energy Procedia*, vol. 77, pp. 113–118, Aug. 2015, doi: 10.1016/j.egypro.2015.07.018.
[37] M. D. Heinemann *et al.*, “Evaluation of recombination losses in thin film solar cells using an LED sun simulator − the effect of RbF post-deposition on CIGS solar cells,” *EPJ Photovolt.*, vol. 9, p. 9, 2018, doi: 10.1051/epjpv/2018006.
[38] F. C. Krebs, K. O. Sylvester-Hvid, and M. Jørgensen, “A self-calibrating led-based solar test platform,” *Progress in Photovoltaics: Research and Applications*, vol. 19, no. 1, pp. 97–112, 2011, doi: https://doi.org/10.1002/pip.963.
[39] G. Grandi, A. Ienina, and M. Bardhi, “Effective Low-Cost Hybrid LED-Halogen Solar Simulator,” *IEEE Transactions on Industry Applications*, vol. 50, no. 5, pp. 3055–3064, Sep. 2014, doi: 10.1109/TIA.2014.2330003.
[40] M. Stuckelberger *et al.*, “Class AAA LED-Based Solar Simulator for Steady-State Measurements and Light Soaking,” *IEEE Journal of Photovoltaics*, vol. 4, no. 5, pp. 1282–1287, Sep. 2014, doi: 10.1109/JPHOTOV.2014.2335738.
[41] “Optical design of a fully LED-based solar simulator.” https://repository.lboro.ac.uk/articles/thesis/Optical_design_of_a_fully_LED-based_solar_simulator/9539816/1 (accessed Feb. 05, 2021).
[42] A. Novičkovas, A. Baguckis, A. Mekys, and V. Tamošiūnas, “Compact Light-Emitting Diode-Based AAA Class Solar Simulator: Design and Application Peculiarities,” *IEEE Journal of Photovoltaics*, vol. 5, no. 4, pp. 1137–1142, Jul. 2015, doi: 10.1109/JPHOTOV.2015.2430013.
[43] K. A. Kim, N. Dostart, J. Huynh, and P. T. Krein, “Low-cost solar simulator design for multi-junction solar cells in space applications,” in *2014 Power and Energy Conference at Illinois (PECI)*, Feb. 2014, pp. 1–6, doi: 10.1109/PECI.2014.6804544.
[44] T. Nakajima, K. Shinoda, and T. Tsuchiya, “Single-LED solar simulator for amorphous Si and dye-sensitized solar cells,” *RSC Adv.*, vol. 4, no. 37, pp. 19165–19171, Apr. 2014, doi: 10.1039/C4RA01841A.
[45] J. Wang, S. Su, G. Zhang, and J. Zhang, “A synthetic method of solar spectrum based on LED,” in *AOPC 2017: Optical Spectroscopy and Imaging*, Oct. 2017, vol. 10461, p. 104610I, doi: 10.1117/12.2283120.
[46] C. A. U. Caballero, R. R. Ponce, and F. G. M. Muñoz, “Design of a LED-based solar simulator for energy harvesting applications,” in *2017 IEEE International Autumn Meeting on Power, Electronics and Computing (ROPEC)*, Nov. 2017, pp. 1–6, doi: 10.1109/ROPEC.2017.8261661.
[47] E. López-Fraguas, J. M. Sánchez-Pena, and R. Vergaz, “A Low-Cost LED-Based Solar Simulator,” *IEEE Transactions on Instrumentation and Measurement*, vol. 68, no. 12, pp. 4913–4923, Dec. 2019, doi: 10.1109/TIM.2019.2899513.
[48] A. Ryer, *Light measurement handbook*. Newburyport, MA: International Light, 1997.
[49] “File:CIE 1931 Luminosity.png - Wikimedia Commons.” https://commons.wikimedia.org/wiki/File:CIE_1931_Luminosity.png (accessed Apr. 16, 2021).
[50] “VLMU3510-365-130 UV SMD LED With Silicone Lens | Vishay.” https://www.vishay.com/leds/list/product-84363/ (accessed Feb. 22, 2021).
[51] “Arduino Mega 2560 Rev3 | Arduino Official Store.” https://store.arduino.cc/arduino-mega-2560-rev3 (accessed Feb. 22, 2021).

[52] “NI LabVIEW LINX Toolkit - National Instruments.” https://sine.ni.com/nips/cds/view/p/lang/es/nid/218410 (accessed Feb. 22, 2021).
[53] “CC-3-UV-S Cosine Correctors.” https://www.oceaninsight.com/products/sampling-accessories/free-space-optics/cosine-correctors/cc-3-uv-s/?qty=1 (accessed Feb. 23, 2021).
[54] “QP400-1-VIS-NIR.” https://www.oceaninsight.com/products/fibers-and-probes/fibers/patch-cords/qp400-1-vis-nir/?qty=1 (accessed Feb. 23, 2021).
[55] “USB Spectrometer for UV, VIS, NIR | Ocean Insight.” https://www.oceaninsight.com/products/spectrometers/usb-series/usb-uv-nir/ (accessed Feb. 23, 2021).
[56] “HL-3P-CAL.” https://www.oceaninsight.com/products/light-sources/calibration-sources/hl-3p-cal/?qty=1 (accessed Feb. 23, 2021).
[57] “Calibrated Reference Solar Cell and Meter.” https://www.newport.com/f/calibrated-reference-cell (accessed Feb. 25, 2021).
[58] “Sol3A Class AAA Solar Simulators.” https://www.newport.com/f/class-aaa-solar-simulators (accessed Apr. 27, 2021).
[59] “TS102GXY / TS102VXY THERMOELECTRIC STAGES Instec Inc: Precision Temperature Control & Liquid Crystal Test Instrument.” http://instec.com/portal/article/index/id/180/cid/48.html (accessed Feb. 25, 2021).

Chapter 4:Improving efficiency of photodevices: Nanostructures.

"What is essential is invisible to the eye" – Antoine de Saint-Exupéry.

In previous chapters, the most common fabrication processes for thin-film solar cells and the development of a characterization system to measure them have been explained. This chapter is the last step of this travel around the solar cells' world, and it will explain how to push the efficiency of this last generation photodevices even further, going through several approaches that had been applied during the last years.

4.1. The biggest drawback: Optical losses

The optimization and improvement process of this whole chapter is based in one simple but strong statement: "All the incident light that does not get absorbed by the active layer, and thus, does not generate an electron-hole pair, is lost energy". Of course, this statement shows the importance of the optical losses, without taking into account the electrical losses. The electrical losses are mainly related with the efficient extraction of the generated electron-hole pair out of the solar cell. Along this section I will focus mainly on the optical losses of the devices. The easiest way to understand this is thinking in a classical silicon solar cell. For illustrative purposes, a schematic view is shown at Figure 4-1.

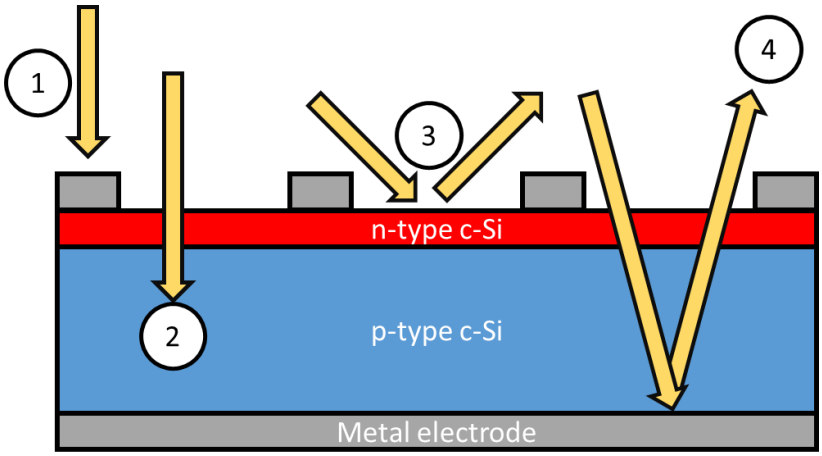

Figure 4-1 Sources of optical losses in Si solar cell. Shadowing of the grid (1), light reflection at the front part (3), light reflection at the rear part (4). One part is effectively absorbed (2).

Several optical losses can be found in this picture, and several solutions have been assigned to them:

- Grid Shadowing (1 in Figure 4-1): This loss is created by the metallic top contact of the cell. This contact is mandatory for the current extraction and flow, so it cannot be removed. Area reduction of this contact is crucial to avoid these losses, but the more reduction it suffers, the higher the associated series resistance will be. Thus, here we encounter a common trade-off, improving the optical response sometime decreases the electrical response, so a "sweet-point"

should be found, where the losses are minimum. Grid analysis were developed a long time ago, actually in 1979 [1], Flat and Milnes studied this resistance increase and how to balance the grid to have the smallest shadowing and resistance possible. 40 years later (2019), Xu et al. published a study where they reduce this shadowing using nanostructures [2]. This kind of approach is of crucial interest in the field and will be explained along the chapter. Furthermore, the so called effectively transparent front contact has been studied, trying to structure the metallic grid in such a way that its transmittance reaches almost 99.9% [3], [4]. Moreover, in new generation solar cells, such as organic, perovskite or even amorphous silicon, this problem is also solved using a transparent electrode for the front contact, e.g., Indium Tin Oxide (ITO), or Fluorine-doped Tin Oxide (FTO)[5]. Of course, the drawback here is that these electrodes are not as good conductors as the metallic ones and therefore their series resistance is higher (which mean higher electric losses).

- Light reflection (3 in Figure 4-1): Not all the incident light in the solar cell is absorbed. In fact, one of the big losses is the initial reflection that the light suffers. This can be well estimated using the Fresnel equation (Equation 54) for normal incidence of light [6]:

$$R = \left(\frac{n_i - n_o}{n_i + n_o}\right)^2 \tag{54}$$

where n_i is the refractive index of the incident medium and n_o is the refractive index of the transmission medium. In this example, the incident medium will be air ($n_i = 1$) and the transmission medium will be silicon ($n_o = 4$ at 550nm incident wavelength). This gives as a result a reflectance of 36%, meaning that only 64% of the incident light is available to generate an electron-hole pair (see Figure 4-2 left). This is a huge loss, because even if everything else is ideal and no other loss is produced (neither optical nor electrical), the maximum efficiency of the solar cell will be only 64%. One of the easiest solutions to this problem is avoiding big refractive indices contrast between interfaces.

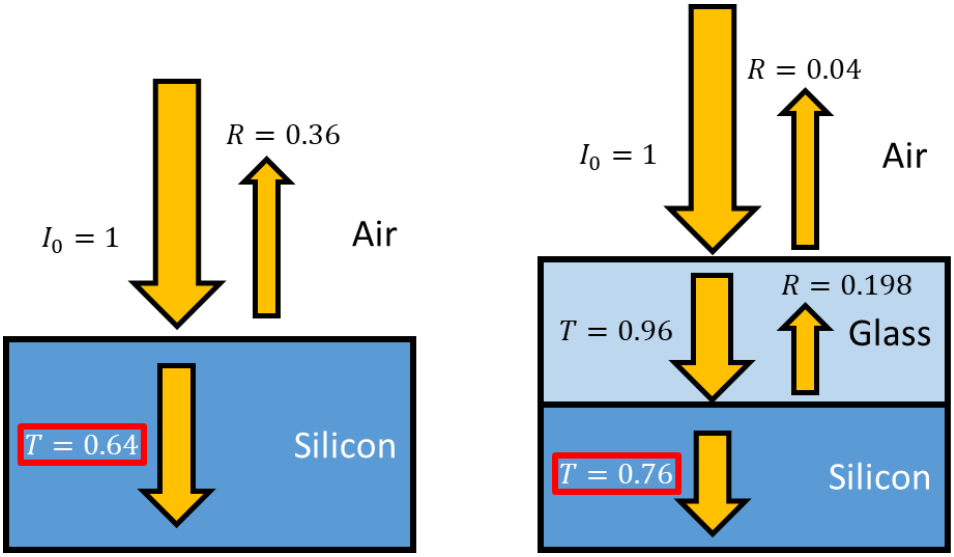

Figure 4-2 Refractive index gradient design to avoid reflection losses. At left, direct transition between air and silicon, producing huge reflection. At right, the inclusion of a glass slab lowers the reflection.

Thus, a refractive index gradient may be generated. For example, in the previous case, by only introducing a glass slab (n=1.5) between air and silicon, the reflectance could be approximated to 4% at air-glass interface and 20.6% at glass-silicon interface (see Figure 4-2 right). This gives an overall reflectance of 23.78% (instead of the previous 36%). Furthermore, several layers of different refractive indices could be introduced to reduce this phenomenon even further (1.5, 2, 2.5,3 and 3.5) but care should be taken, otherwise these new layers will affect both the optical (through parasitic absorption) and electrical (increasing resistance) behavior of the device. More elegant solutions will be given in the next section to solve this problem.

- Backside reflected light (4 in Figure 4-1): Similar to the previous loss, this is also a reflection loss. However, in this case the light goes through all the device, is reflected at the backside, goes through the device again and escapes to the outside. So, the responsible of this loss is not the same one as in the previous case. This loss is mainly related with the bad absorption of light of the active layer, and can be analyzed using the Beer-Lambert Law (Equation 55)

$$I(L) = I_0 e^{-\alpha L} \tag{55}$$

being I_0 the light intensity incoming in the upper part of the device (only the transmitted part, not the reflected), α the absorption coefficient of the material, L the distance travelled through the material and I the light intensity at a certain point. This equation follows an exponential trend in which, if the absorption coefficient is high enough, the light will be absorbed probably in a few nanometers. But, if the absorption coefficient is very low, the light can go through all the device and back again without being absorbed at all (supposing that the back metal electrode has a reflectance of 100%). Just as an example, the absorption coefficient of silicon at several wavelengths is shown at Figure 4-3.

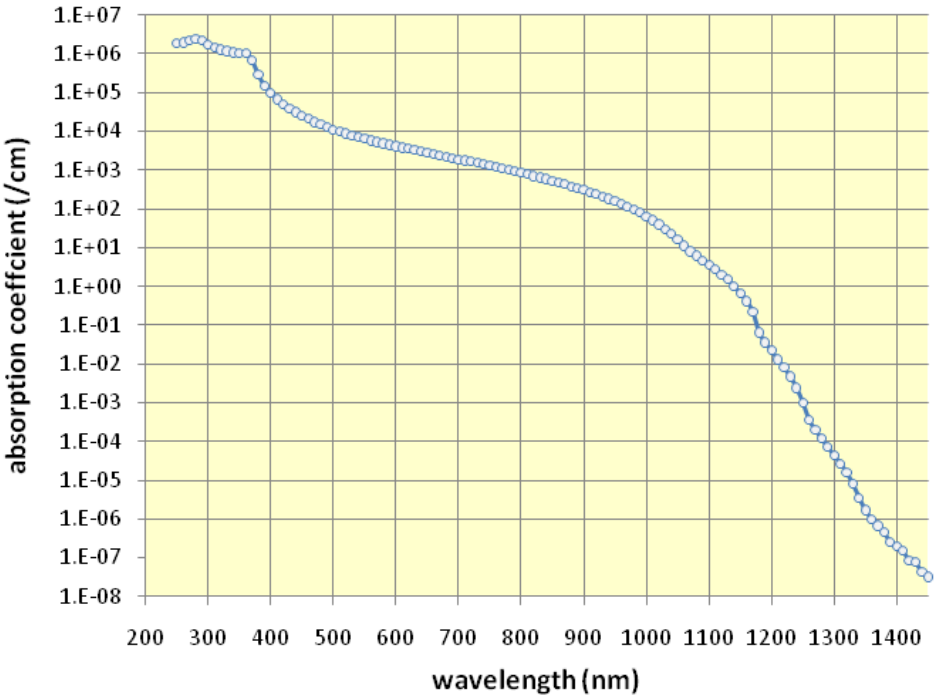

Figure 4-3 Absorption coefficient (cm^{-1}) of Silicon. Image extracted from [7].

The intuitive solution to this problem is to increase the thickness of the active layer, thus increasing *L* in the equation above. Of course, the higher the distance travelled by light, the higher the probabilities that it will be absorbed. But this solution has a big drawback from an electrical point of view: The generated carriers (electrons and holes) should be extracted out of the active layer before they recombine back, and this is determined by the carrier diffusion length. This value represents the average length that a carrier can travel before a recombination happens, so the thickness cannot be higher than the carrier diffusion length, otherwise, not a single carrier would be extracted.

More convenient solution is using an active material that has an acceptable absorption coefficient at all the wavelengths of interest. Notwithstanding, this will lead to a lot of electrical losses due to thermalization, because a material cannot absorb efficiently both low and high energy photons. This reasoning is the motivation to use various active materials in the same device, leading to the tandem solar cell concept (further explained).

Summarizing, these are the "big-three" in the optical losses produced at any kind of solar cell. In the next sections, more advanced solutions to these problems (light management, constructive/destructive interference, tandem solar cells, etc.) will be given and applied in works that generated scientific publications during this thesis.

4.2. Theoretical foundation: Resonances and light trapping

In this section more advanced light management techniques to alleviate the optical problems exposed in the previous section will be explained.

One of the basic solutions to mitigate the optical losses is based on the light interference phenomenon, and it is called "Anti-Reflection Coating" (ARC).

This technique is based on introducing a layer of transparent material between the top layers (e.g., between air and silicon), in such a way that both produced reflections generate a destructive interference phenomenon that blocks all the reflection. In first place, to produce destructive interference, a 180° (π rad) phase-shift between two waves should be generated. Figure 4-2 (right) will be used again to explain this phenomenon. Here, one wave is produced at the air-glass interface that will be reflected, and another one will be produced deeper, at glass-silicon interface, that will be also reflected and hit the air-glass interface. The air-glass reflected wave will be the reference (phase = 0), so the phase-shift between both is calculated in the following way:

$$\delta = \frac{2t_1}{\lambda_1} \cdot 2\pi = \frac{4\pi t_1 n_1}{\lambda_0} \tag{56}$$

being δ the phase-shift between both waves, $2t_1$ equals the light path (twice the thickness of the ARC layer), λ_1 is the effective wavelength inside the material and 2π is the phase-shift per wavelength in radians. Thus, to have a destructive interference, the result of Equation 56 should be equal to π:

$$\delta = \pi = \frac{4\pi t_1 n_1}{\lambda_0} \rightarrow t_1 = \frac{\lambda_0}{4n_1} \tag{57}$$

Therefore, the optimal thickness of the ARC can be computed to achieve a perfect destructive interference. Checking the Equation 57 the so called "quarter-wavelength slab" is found. This is a rule of thumb to say that the destructive interference, and thus, the minimum reflection, will be produced with a thickness equal to a quarter of the wavelength of interest in that material (i.e., the vacuum wavelength over the material refractive index).

Now, to achieve full wave cancellation, both amplitudes should be equal too. At the end, applying the Fresnel coefficients for a normal incidence case (having a quarter wavelength slab), the Reflection of the whole stack equals to:

$$R = \frac{\left(n_0 n_S - n_1^2\right)^2}{\left(n_0 n_S + n_1^2\right)^2} \tag{58}$$

Which, looking for $R = 0$, results in the Equation 59:

$$n_1 = \sqrt{n_0 n_S} \tag{59}$$

So, to avoid any kind of reflection at a certain wavelength, a material with a refractive index equal to the geometric average of the surrounding indices should be used, and with a thickness equal to a quarter of wavelength. Indeed, this can only efficiently nullify the reflection at one wavelength, and that is why more complex approaches that use several ARC layers have been developed [8]–[10].

Regarding the low absorption of the active layer, a lot of research has been developed to increase this absorption without damaging the electric performance. That

is done using light management techniques, such as the light trapping. As previously explained, the only way to increase the absorption of photons in a material having a bad absorption coefficient is to increase the thickness of the active layer, to make a longer path to travel for light. However, a similar effect can be achieved if the light goes through the device several times in a row. This means that, maintaining the film thickness we can multiply the travelled optical path several times, trapping the light inside the device. Actually, there is a physical phenomenon that has this exact effect, and it is called Total Internal Reflection (TIR). This phenomenon occurs when light pass from a high refractive index medium to a lower one, at an incident angle higher than the so called "critical angle". When this happens, all the light is totally reflected. This is demonstrated by the Snell's law (Equation 60).

$$n_i sin\theta_i = n_o sin\theta_o \tag{60}$$

being n_i and n_o the refractive indices of the incident and the output media, θ_i and θ_o the incident and output angle. The critical angle is determined fixing the output angle at 90° (Equation 61)

$$\theta_{crit} = \sin^{-1}\left(\frac{n_o}{n_i}\right) \tag{61}$$

Of course, this angle will exist only when the incident medium has a higher refractive index than the output medium $\left(\frac{n_o}{n_i} < 1\right)$. This is an advantage, because usually the layer with the higher refractive index is the active layer.

To produce this effect, usually a texturization is applied on the layers of the device, either on the front, on the back or on both sides. Very common types of texturing in silicon solar cells are the pyramid and inverted pyramid nanostructures, although randomly texturized surfaces can also improve the properties of the cell [11], [12] (see Figure 4-4).

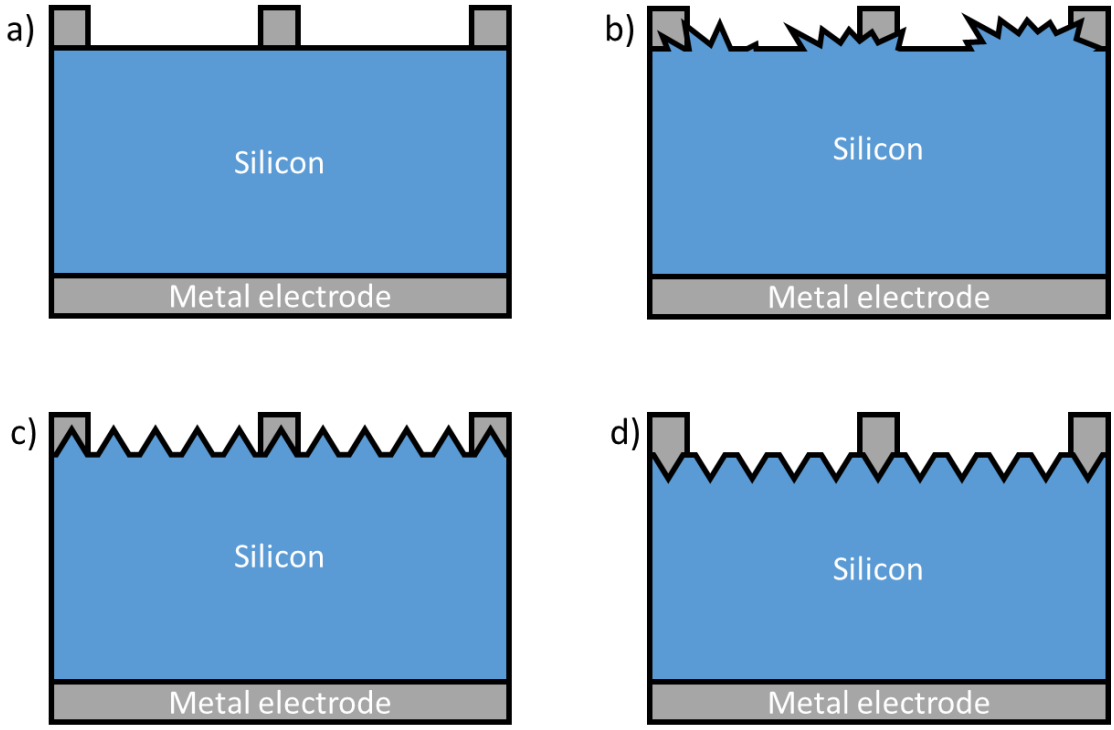

Figure 4-4 Examples of front texturing. a) Planar structure. b) Random texturing. c) Pyramid structure. d) Inverted pyramid structure. Same structures can be replicated at the back electrode.

With these structures the light takes very different paths inside the cell, improving the absorption of the device and thus, the efficiency. These structures can be replicated also on the back electrode to achieve a double texturing effect. Another useful technique is to achieve a Lambertian reflector in the backside of the cell, to enhance the Total Internal Reflection phenomena [13]–[15].

Furthermore, when these structures are periodic along the cell, they can produce diffractive effects, similar to a diffraction grating, generating several diffraction modes at a wide variety of angles, which can produce light confinement too. Actually, a clear example of this is one nanostructure that I have developed and presented at the META conference in Lisbon, 2019 [16]. The nanostructure can be seen at Figure 4-5. This work is still in progress, but the main goal is to fabricate the device and check the improvement in the absorption at certain wavelengths that interfere with the diffraction grating.

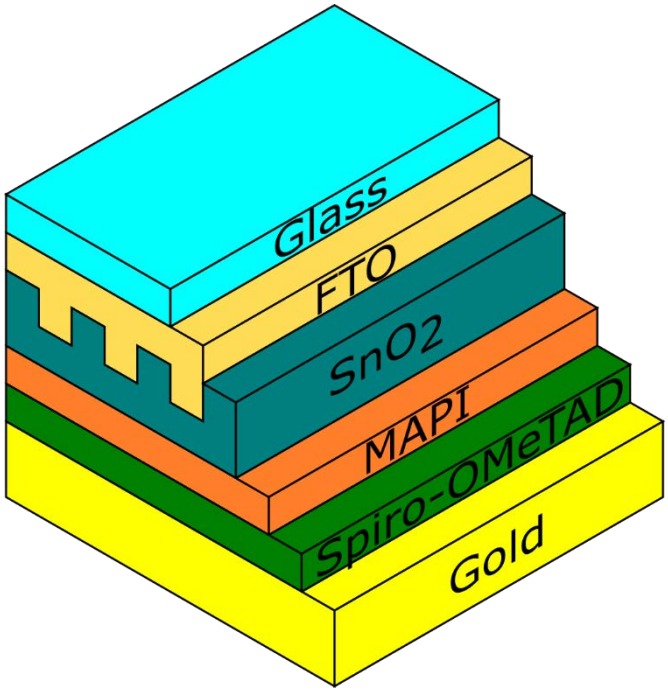

Figure 4-5 Nanostructured Diffraction Grating on a perovskite solar cell.

Following sections explain in detail how all of these approaches were used and how they were implemented using Finite Element Method based software (COMSOL® and JCMSuite®).

4.3. Contribution in silicon solar cells

Here, we tried to improve the efficiency and behavior of amorphous silicon solar cells. Silicon solar cells are nontoxic, and their basic material is very abundant. Amorphous silicon was selected because is less expensive than the perfect monocrystalline silicon. Of course, the drawback is that it has a poor electric behavior, with very short carrier lifetimes and low mobility carriers compared to its crystalline analogous. This fact will limit the thickness of hydrogenated amorphous solar cells to a maximum of around 350nm [17]. That is why this technology is a clear candidate to apply light trapping techniques on it, trying to keep the active layer as thin as possible.

One of the main effects that are used to achieve light resonances (and thus, light management) are the plasmonic resonances, which are collective oscillations of electrons in the conduction band that resonates with an electromagnetic field of incident light. This resonance can appear localized or in a whole surface. This effect can be achieved using very small metallic particles, that will interact with the light in several ways, depending on their size and shape [18]. The disadvantages of using these plasmonic particles are mainly the absorption losses with the consequent heating of the device. These problems were solved using semiconductor nanoparticles that also interact with light, not through plasmonic resonances but through Mie resonances [19]. These nanoparticles can also be designed in size and shape to interact with specific wavelengths, achieving a zero backward scattering or a minimum forward scattering conditions [20]. In the literature a lot of examples of different nanoparticles can be found, such as parallelepiped [21] or spherical [22]. In this last case, the TiO_2 nanoparticles were semi-buried inside the silicon layer, which improved its absorption

around three times. It has been demonstrated that the deposition of spherical nanoparticles can improve the efficiency of a thin-film gallium arsenide solar cell (by 11%) [23], or a silicon solar cell (by 26.5%) [24], projecting more light to its active layer.

But the light behavior can also be altered tailoring some layers of the device, for example patterning them with grooves, crosses, hexagons, or any kind of shape, giving birth to the whole topic of metasurfaces. The cross-shaped approach has been studied previously, in order to make band filters (e.g., UV, IR filters) [25], spectrally tunable perfect absorbers [26] or light emitters [27].

So, taking all these successful ideas into account, we tried to mix them, generating a surface with a cross pattern filled with resonant nanospheres. A drawing of the proposed idea is shown at Figure 4-6. This work generated a publication at Solar Energy journal [28].

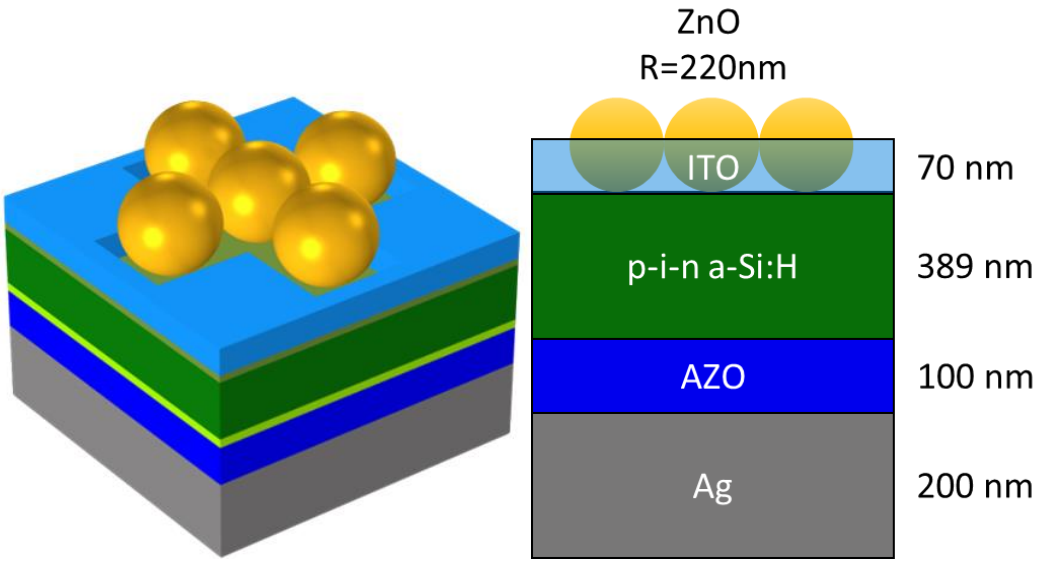

Figure 4-6 (Left) Picture of the cross-packed nanospheres over a hydrogenated a-Si solar cell. (Right) Cross-section of the design with the thickness of each layer.

Any time a new idea is proposed, the feasibility of fabrication should be studied, otherwise the theoretical efficiency improvement is lost, due to the impossibility of fabrication. The proposed structure has two fundamental fabrication process: the etching of the crosses and the placement of the nanospheres inside the crosses. In first place, the etching of patterns is not something new, there are several techniques that can be applied to achieve this goal. In liquid processing, such as spin-coated layers (Chapter 2 explains this process in depth), the nanoimprint technique can be used, pressing the liquid layer with a PDMS stamp to form a determined pattern, such as grooves [29]. Moreover, complex structures such as 3D flowers can be obtained using a combination of nanoimprinting and ion-assisted aerosol lithography to create the stamp [30]. This technique has been applied also in silicon [31].

Regarding the deposition of the nanoparticles inside the crosses, it can be found on previous literature too. There are examples of deposition of particles with a diameter smaller than 100nm inside grooves and holes [32], [33] following a spin-coating process.

So, now that the possibility of fabrication is confirmed, an optical analysis of the structure is needed to see the effects of the metasurfaces in the device. In this work, a

software based on Finite Element Method (FEM), COMSOL Multiphysics®, was used to compute the optical behavior of the system.

The starting point is a planar solar cell with the next configuration, from bottom to top (see Figure 4-6): a metallic electrode (200 nm), an Aluminum-doped Zinc Oxide (AZO) contact layer (100 nm), n-doped hydrogenated amorphous silicon (a:Si-H, 22 nm), intrinsic a-Si:H (150nm), p-doped a-Si:H (17 nm) and an indium-doped tin oxide (ITO) contact layer (70 nm). Usually, the active layer is thicker [34], [35] with a limit of around 350 nm, due to the poor carrier mobility of amorphous silicon. Thus, the thinner the active layer, the better electric behavior will have, and that is why we set a thickness of 150 nm in our initial design. Of course, the thinner the active layer the worst the absorption will be, and there is where nanostructures come into play.

In order to compute how well a cell behaves, the short-circuit current density (J_{SC}) is used, but to limit the results to those due to the optical effects, it is under the assumption that every absorbed photon generates an electron-hole pair, and every carrier is extracted successfully (i.e., the EQE equals 1 at every wavelength of interest). This parameter is calculated using Equation 62.

$$J_{SC} = \int q \cdot \frac{\lambda}{hc} \cdot A(\lambda) \cdot \phi_{\mathrm{AM1.5G}}(\lambda) \cdot d\lambda \tag{62}$$

being q the elemental charge in Coulombs, λ the wavelength of interest in nanometers, h the Planck's constant, c the speed of light in vacuum (meters per second), $A(\lambda)$ the absorption of the device (unitless, wavelength dependent) and $\phi_{\mathrm{AM1.5G}}(\lambda)$ the spectral power of the AM1.5G spectrum (in watts per square meter per nanometer). The integration should be done over the spectral range of interest, in this case from 300 to 800 nm.

This spectral range is selected due to the characteristics of our device: On one hand, below 300nm, all the light will be absorbed by the ITO, in the first layer, so no current can be generated, because the light cannot reach the active layer of the device. On the other hand, over 800nm, the light will pass through the active material without being absorbed due to its bandgap. 800 nm equals to an energy of around 1.55eV, while the bandgap of a-Si:H is in the range of 1.5-2.0 eV, depending on growth conditions and hydrogen content [36]. So, in the best case, the a-Si:H would not absorb wavelengths longer than 800nm.

Every term is known here, except the absorption of the device, that is calculated by the simulation software using the spectral absorbed power in each material. This power is internally calculated using Equation 63 [37]:

$$P(\omega) = \frac{1}{2}\omega\varepsilon''(\omega)|E(\omega)|^2 \tag{63}$$

where ω is the angular frequency of incoming radiation, $|E(\omega)|^2$ is the intensity of the electric field inside that material and $\varepsilon''(\omega)$ is the complex part of the permittivity of the material (wavelength dependent). So, the absorption will be equal to this power over the input power (at each wavelength of interest).

Thus, applying the previous equations and using the optical constants for each material extracted from [38], the reference result is obtained as a J_{SC} of 9.14 mA/cm^2.

Now, using the sphere-filled cross pattern, and sweeping across the refractive index of the spheres (i.e., the material used to fabricate them) and their radius (size), the J_{SC} of each configuration was computed (Figure 4-7).

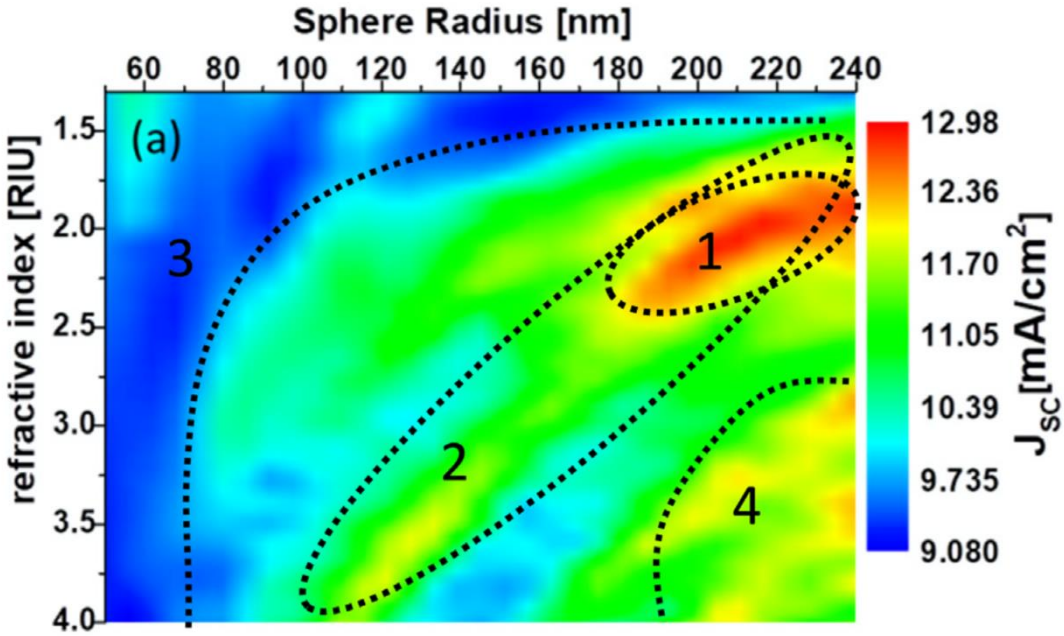

Figure 4-7 Parameter sweep of the size of the nanospheres (radius) and their material (refractive index), searching for the highest short circuit current density.

Checking the figure, a maximum J_{SC} of 12.87 mA/cm^2 can be achieved, which implies an enhancement from the reference level of a 40.8%. This value is produced when the radius of the nanospheres is 210 nm and their refractive index equals 2. Both conditions can be fulfilled in real life using silicon nitride or zinc oxide, for example. This improvement can also be checked at Figure 4-8, where it can be seen the absorption improvement and reflection reduction of the nanostructured vs the planar cell.

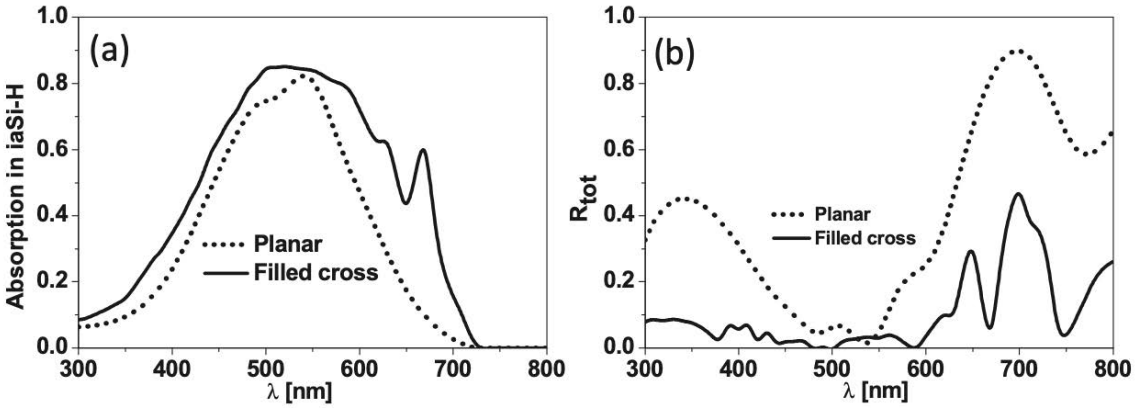

Figure 4-8 Absorption (a) and reflection (b) of planar vs structured device.

These improvements are generated by the resonances produced at the nanospheres and the crosses, that project and focus the light into the active layer of the device. The field confinement is shown at Figure 4-9.

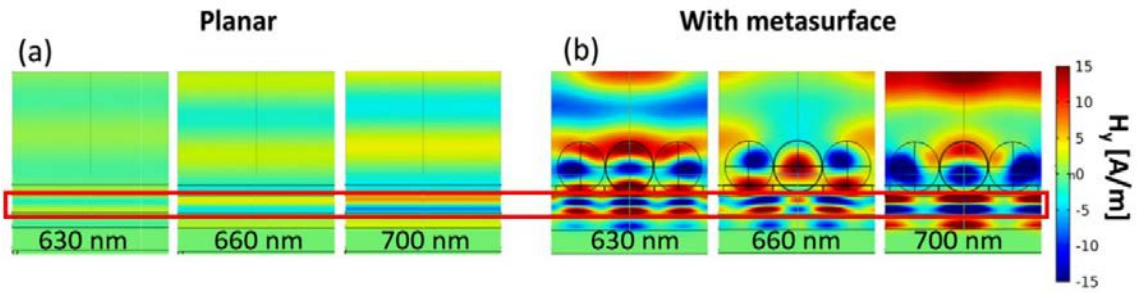

Figure 4-9 Magnetic field distribution inside planar (a) and nanostructured (b) solar cell. Red rectangle highlights the active layer.

It can be seen that in the planar configuration there is no focus at all, but in the nanostructured one the field is highly focused into the silicon active layer, increasing the absorption of the device, thus the efficiency.

As a final check, a thickness sweep was done, having three different configurations: planar, cross-etched pattern, and nanospheres into each cross. The comparison between them can be found at Figure 4-10.

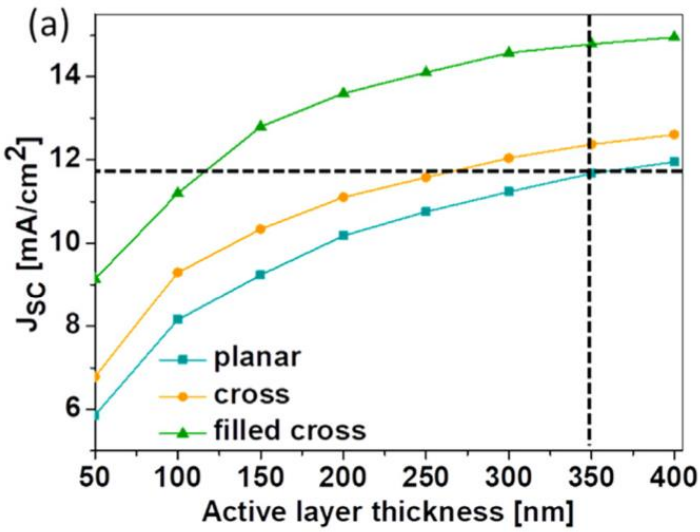

Figure 4-10 Short circuit current density vs active layer thickness for three different configurations.

Vertical black line represents the output current improvement that can be achieved using the nanostructure with the highest possible thickness. Horizontal black line shows the fact that, with this nanostructure and 150 nm thickness, the same current than a 350 nm thick planar cell can be achieved, but with an improved electric behavior.

4.4. Contribution in perovskite and tandem solar cells

The approaches followed in the previous work can be used to improve the absorption of the active layer, but even increasing the absorption to 100%, a perfect efficiency cannot be obtained. This is due to the absorption capability of the active layer, related with the bandgap of the semiconductor (it cannot absorb photons with less energy than its bandgap). Moreover, photons with higher energy than the bandgap can generate also thermalization losses, losing a lot of energy in form of heat.

All these absorption problems related with the material bandgap are summarized inside the commonly known as Shockley-Queisser limit [39], that stablishes a theoretical efficiency limit for a single junction solar cell of 30% at a bandgap of 1.1 eV. So, even in the best case, for all the power that is received from the Sun (1000W/m^2), only 300W/m^2 could be extracted. One of the solutions to this problem is to use active layers of different materials, with different bandgaps, giving birth to the concept of tandem solar cells. Conceptually, with an infinite number of layers, they could reach an efficiency value of 86.8%, with concentrated sunlight. Of course using an infinite number of layers is not realistic, but using only two, the cell could reach an efficiency of 55% under concentrated light and 42.3% under non-concentrated light [40].

So, in the last years, tandem technology has been explored, especially using perovskite in combination with silicon, due to the tunable bandgap of the perovskite depending on its composition, their high efficiency and low prices [41]. One of the first monolithic tandem silicon-perovskite solar cell was developed in 2016 by Prof. Steve Albrecht and its team at Helmholtz Zentrum Berlin (HZB) together with École Polytechnique Fédérale de Lausanne (EPFL) [42]. During the last year 2020 two world records were achieved in tandem Si/PVSK solar cells, the first one by HZB (29.15% efficiency) and the second one in December 2020 by Oxford PV (29.5% efficiency) [43].

Regarding the construction of the tandem solar cells, mainly two approaches can be taken, the so-called 2-terminal and 4-terminal configurations. On one side, the 4-terminal configuration is the most intuitive one, because it consists of stacking one subcell over the other, being each one electrically independent, thus, needing 4 wires to contact the cell. The main advantage lays on this independence because both subcells can be manufactured independently and stacked together using a layer between them for the optical coupling. This leads to the main disadvantage too, because the optical coupling between both subcells can generate high losses, reducing the efficiency.

On the other side, the 2-terminal configuration is based on an electrical connection between both subcells (they are connected in series). This connection avoids the optical coupling problems, because both cells are manufactured at the same time, in the same fabrication process (monolithic construction), resulting in only two connection terminals. Thus, a reduction in optical losses is achieved. However, due to the electrical series connection, both subcells should be optimized to match their generated photocurrents, because the limiting factor will be the subcell with the lowest photogenerated current.

In this work we used some nanostructuring techniques inside the perovskite active layer to check the light trapping phenomena and the consequent efficiency increase. This work generated a publication in MDPI Nanomaterials journal during 2019 [44]. The idea here is similar to the one in the amorphous silicon solar cell (Section 4.3.), but here it is the whole perovskite active layer what is nanostructured. The structure proposed is a monolithic construction (2-terminal configuration) shown at Figure 4-11. This kind of structure requires a current matching between both cells, due to their internal series connection, as previously explained. This means that the voltage generated by the whole cell will be the addition of the independently generated sub-cell voltages, but the current flowing through both should be constant. That is a special

difficulty, because now not only an increase of absorption is needed, but also a photocurrent balance between both sub-cells.

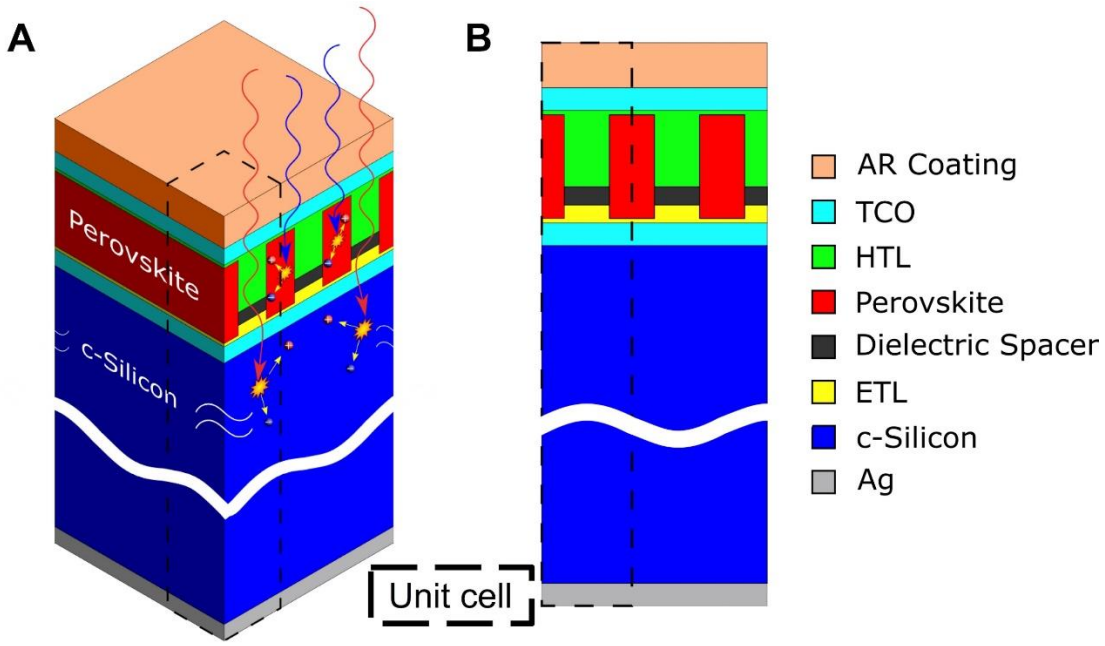

Figure 4-11 Schematic drawing of the nanostructured tandem solar cell in 3D (a) and 2D (b) view. Obtained from [44]

One possible configuration of this layers, going from bottom to top, can be the next one: Silver electrode / n-type hydrogenated amorphous Silicon (na-Si:H) / intrinsic hydrogenated amorphous Silicon (ia-Si:H) / n-type crystalline Silicon (n-c-Si) / ia-Si:H / p-type hydrogenated amorphous Silicon (pa-Si:H) / Indium Tin Oxide (ITO) / Titanium Oxide (TiO_2) as Electron Transport Layer (ETL) / Perovskite ($MAPbI_3$) layer / Spiro-OMeTAD as Hole Transport Layer (HTL) / Indium Zinc Oxide (IZO) / Antireflection coating (MgF_2). The optical simulations and calculations were done in the same way as in the previous section, but in this case p-i-n a-Si:H layers were ignored, due to their thickness. Very thin layers do not affect the optical behavior of the device, because they are almost "invisible" to the light [45]. In the nanostructure, also a dielectric spacer layer between ETL and HTL is needed (in this study, Si_3N_4 was used).

The planar structure was taken from [45] and used as a reference in this study to check the enhancement produced by the nanostructure. The main goals that should be achieved with the nanostructure are:

- Low-energy photons should be guided to the silicon sub-cell, to improve its absorption.
- High energy photons should be scattered and trapped inside the perovskite layer to absorb them efficiently.
- The current matching between both cells should be achieved by tuning the geometrical properties of the grating.

To determine the optimum geometry parameters that the nanostructure should have, a parametric sweep was done, checking the short-circuit current density of each sub-cell for each case. The results can be seen at Figure 4-12.

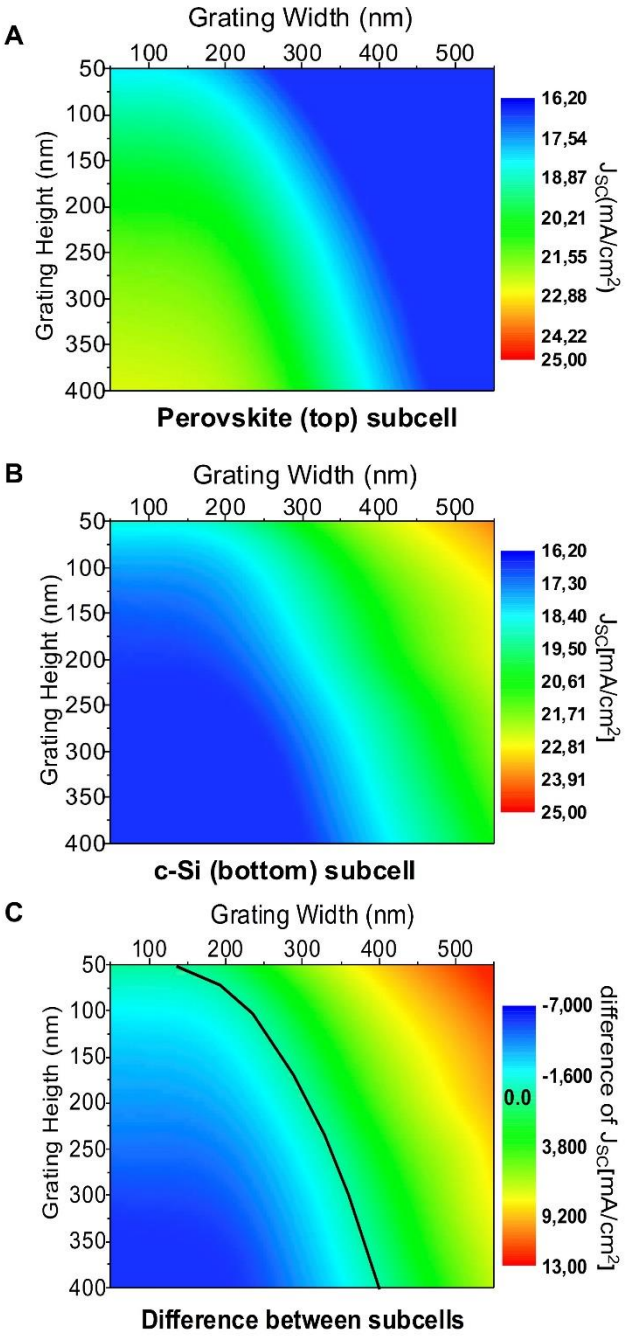

Figure 4-12 Parametric sweep of width and height of nanostructure and its resulting short-circuit current density for top (a) and bottom (b) subcells. (c) shows the difference between both currents, i.e., the current matching when nulling. Obtained from [44]

Here, we should search not only for the highest J_{SC} value, but also for the one that maintains the current matching in both subcells. This point is found in a grating width of 300 nm and a height of 225 nm, giving a result of 18.8mA/cm^2, which means an improvement of a 16% against the reference value (16.22mA/cm^2).

Furthermore, in this work the angular incidence was also studied, to determine the realistic case of the sun moving, and impinging to the cell at different angles. Thus, Figure 4-13a shows the increase of absorption of silicon and perovskite sub-cells under

normal incidence and Figure 4-13b shows the short-circuit current density under different angles of incidence.

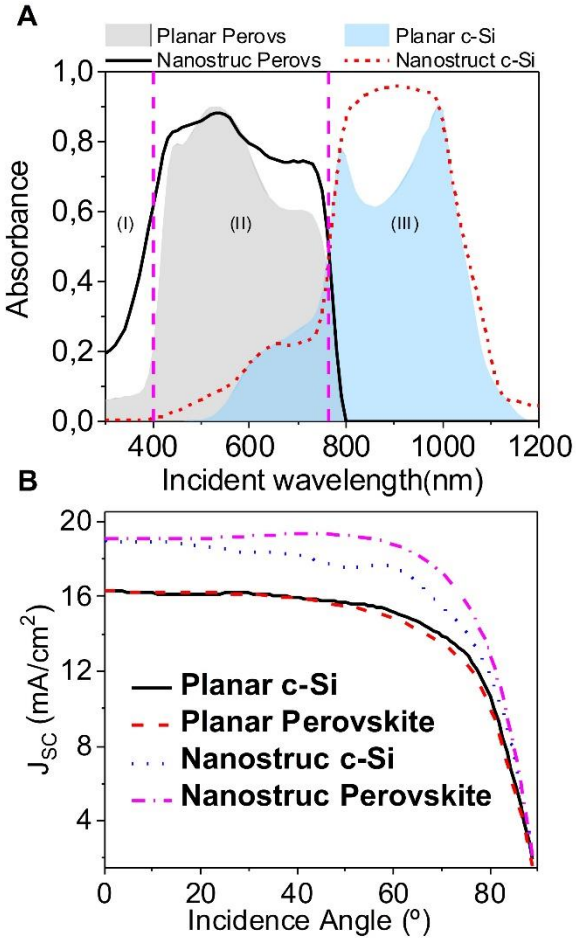

Figure 4-13 a) Absorption improvement of the subcells with the nanostructure. b) Angular response of the cell w/ and w/o nanostructure. Obtained from [44].

It can be seen that the absorption improves in the low (III), medium (II) and high (I) energy photons zones in both perovskite and silicon subcells. Regarding the angular dependance, the current matching is lost at 20° of incidence, even though the limiting short-circuit current density (silicon subcell) is still higher than without a nanostructure for incident angles higher than 20° (around 15% of improvement). Furthermore, following this optimization process, the device can be optimized for a specific angle of incidence instead of normal incidence.

So, with this study the possibility of increasing the efficiency of a tandem solar cell was confirmed, also checking its behavior against tilted incidence of light.

As an extension for this work, we developed another study in which we explored further possibilities in the appropriate material selection to make the nanostructure. In this case a sweep over several refractive indices and thicknesses was done to find the optimum combinations to build the ETL, HTL and dielectric spacer layers (see Figure 4-11) with minimal optical losses. With this parametrical sweep, we found several options that the manufacturers can use to adapt their fabrication processes and their materials to obtain the best tandem solar cell according to their facilities.

For example, Figure 4-14 shows the parametric sweep done over the HTL. It can be seen that there is a minimum losses zone that goes from 100 nm to 300 nm thickness with a refractive index that goes from 1 to 2.2. This means that there is a lot of room for the fabrication tolerances and also that the manufacturer can choose among a wide selection of materials. No matter what combination is chosen, as long as it belongs to the blue zone, the losses will be minimal. The complete study was published in Scientific Reports journal [46].

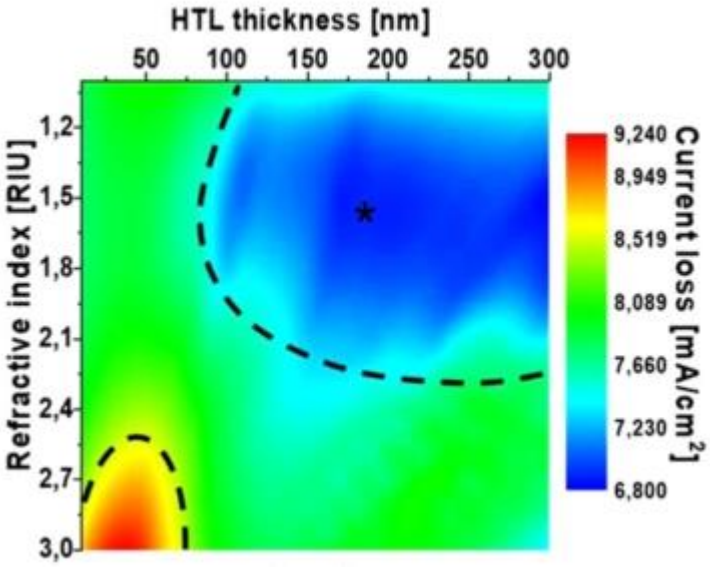

Figure 4-14 Material and geometry selection to check the optical losses in hole transport layer.

So, both tandem solar cell studies intend, not only to find and develop a nanostructure that improves the efficiency of the solar cell, but also to transfer this knowledge to the manufacturers, easing the selection of appropriate materials and geometrical parameters to adapt their facilities to build this design successfully.

4.5. Contribution in emitters: Deep UV-LEDs

During my international research stay at Helmholtz Zentrum Berlin (Berlin, Germany), I took another different approach. This time I tried to apply all the knowledge in nanostructures that I had obtained to improve the output of LEDs, instead of improving the absorption of solar cells as I did before. My work was mainly focused on Deep UltraViolet Light Emmiting Diodes (DUV-LED), because they are used in a wide range of applications, such as water purification [47] and sterilization [48], 3D printing [49], curing resins [50], skin cures [51] or optical storage [52] and they have still a big drawback: a very small efficiency [53], [54] below 4% (the visible LEDs usually have efficiencies higher than 70%). This small efficiency is provoked by the fabrication material itself, since UV photons are high energy photons that should be generated by a high bandgap semiconductor (typically AlGaN). This material has a very high refractive index, higher than its surrounding layers. This implies that a lot of TIR will occur; in other words, most of the generated light will be trapped in this layer until it is absorbed, reducing the emitted light dramatically. A simplified schematic showing the layers of a

DUV-LED is shown at Figure 4-15 (this color scheme will be maintained over all the section). This configuration was obtained from Dr. Martin Guttmann thesis [55].

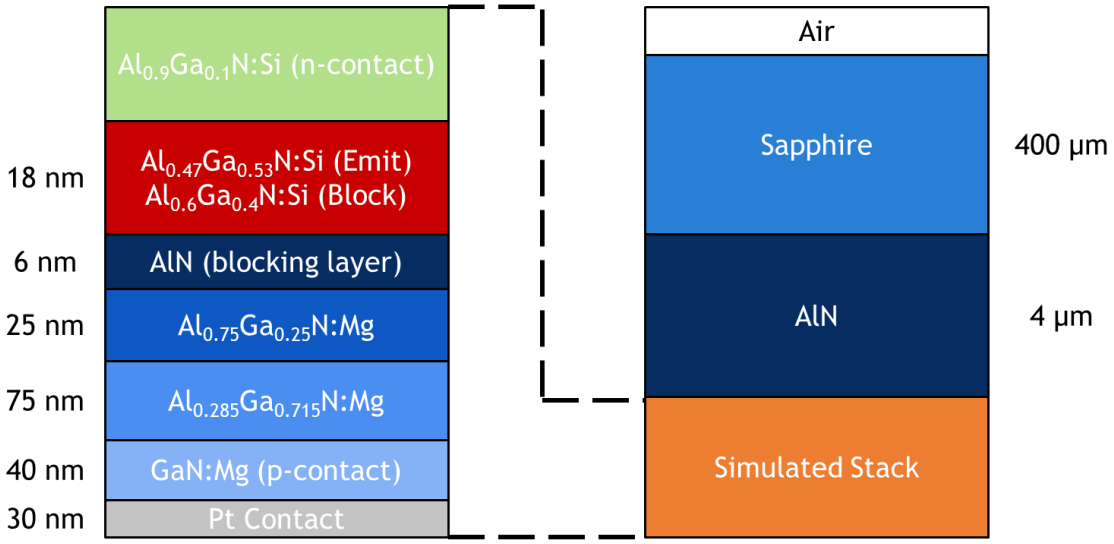

Figure 4-15 Left: Simulated layer stack that represents the DUV-LED. Right: The full structure of the device, consisting of the simulated stack over a Sapphire and AlN substrate.

Several methods have been proposed in order to solve the light extraction efficiency (LEE) problem: from optical management, using micro-lenses [56] or rough surfaces [57], to transparent contact layers and highly reflective electrodes [58], [59].

Notwithstanding, in a previous study of HZB [60], they demonstrated that the limiting factor of LED light extraction efficiency is the highly absorptive p-layer (in this example, the GaN:Mg contact).

So, during my research stay, I designed the insertion of a nanostructure to increase the back reflection, avoiding that light can go into the GaN:Mg and get absorbed. To do so, I used JCMSuite®, a FEM software that allows the simulation and analysis of optical structures in a highly customizable way. But the first step, before the inclusion of the nanostructure, was to simulate the reference device, to check its LEE and the losses. While in solar cells an incoming plane wave was used for excitation, here the source of light is inside the device, so a whole different approach is needed. Actually, due to the small size of the layers (the active layer has a thickness of 18nm), a dipole source was modelled, because the plane wave approximation is not valid.

The first calculations were done on the planar stack with a dipole source placed in the middle of the active layer and x-polarized (i.e., with the preferred emission on z-axis). The real and imaginary parts of the refractive indices of the materials were obtained from references [61]. Resulting absorption and TIR values are shown on Figure 4-16.

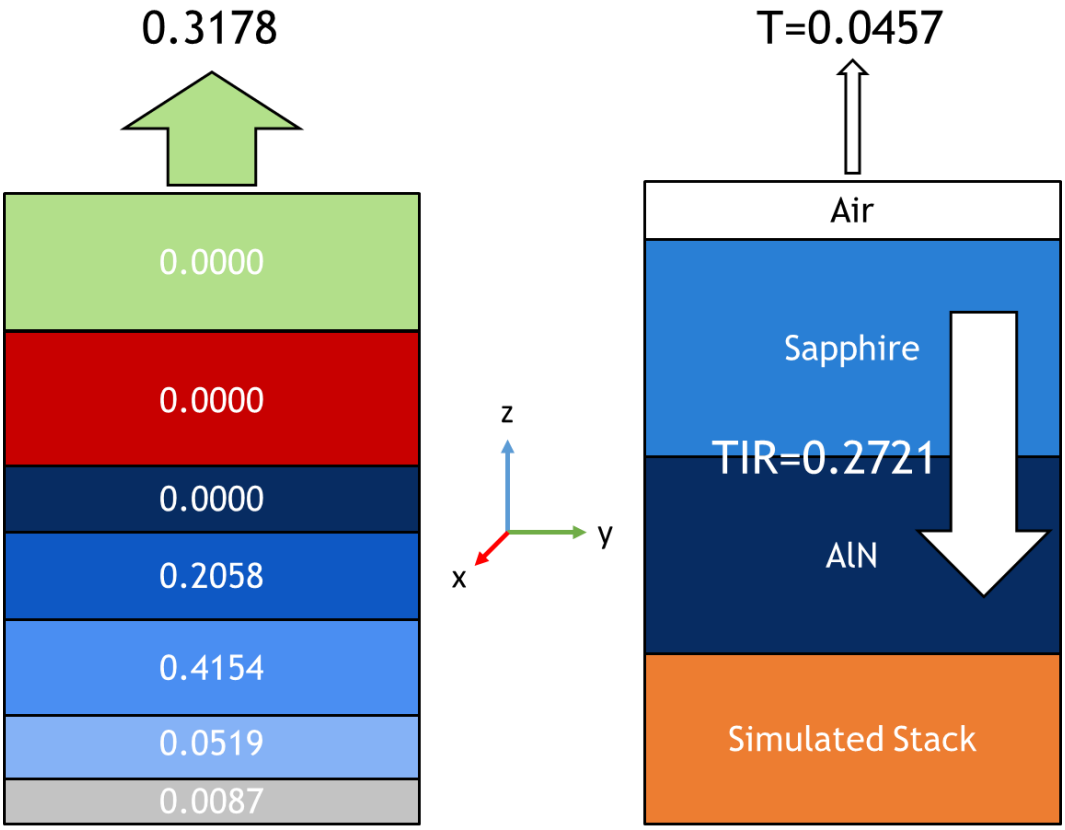

Figure 4-16 Planar device analysis. Left: Absorption on each layer and amount of light launched to the substrate. Right: Part of the light will be projected to the outside, but most will suffer TIR.

It can be seen that the full block of p-contact (AlGaN:Mg and GaN:Mg) absorbs 67.31% of the emitted light, which is a huge loss (in contrast, 0.87% will be absorbed by Pt electrode). After that, the remaining 31.78% should be projected out, but due to the dipolar emission some light will be totally reflected, due to the refractive index contrast of the subsequent layers. At the end, of all the generated light, 68.22% will be absorbed and 27.21% will be reflected back and absorbed too, giving a light extraction efficiency of only 4.57%, which matches to the actual state of the art.

Looking at these results, mainly two problems should be solved: first one, the absorption at the p-side must be dramatically reduced; and second, the light should be redirected to avoid the total internal reflection phenomena.

The proposed nanostructure intends to solve both problems, reducing the amount of the absorbing p-contact material and creating a reflective surface that projects the light inside the so called “escape cone”, in which the light can escape from the device. This is done making holes through all the p-contact and filling them with platinum, creating a nanostructured electrode (Figure 4-17).

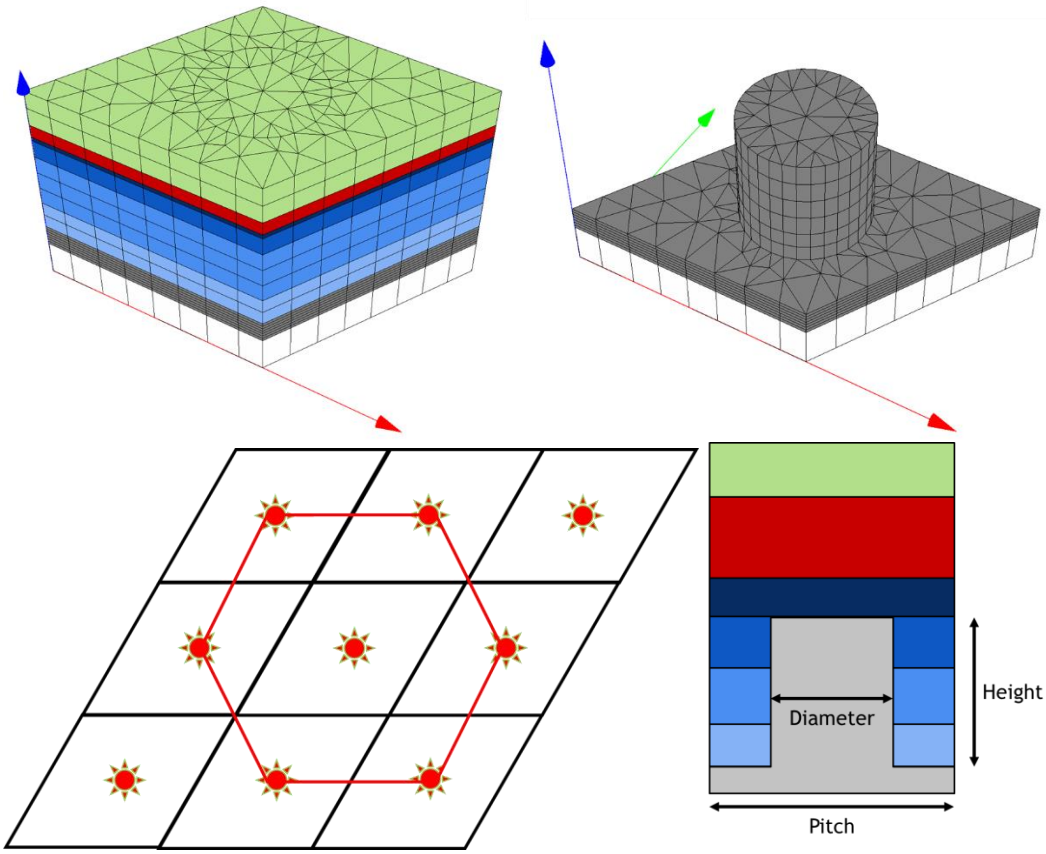

Figure 4-17 Schematic of the proposed nanostructure. Top: 3D model showing the Pt pillars in hexagonal arrangement (unit cell). Bottom: Top view of the hexagonal arrangement and 2D drawing of the nanostructure.

Based on previous studies, arbitrary values were given to the nanostructure: pitch equals to 300nm, diameter equals to 150nm and height equals to 140nm (distance between Pt layer and AlN layer, going through all the p-contact). With these parameters, 64 dipoles were homogeneously distributed in the middle of the active layer to analyze the effect of the dipole position in the nanostructure behavior. The results of the simulation (averaged over the 64 dipoles) are shown in the same way that the planar device simulation.

The improvement can be seen at Figure 4-18. The light extraction efficiency is raised up from 4.57% to 11.1% whereas the total absorption of the p-contact goes from 68.22% to 33.66%. Therefore, the absorption in the p-contact is reduced to half, achieving one of the proposed goals successfully. Notwithstanding, the absorbed light at Pt is increased from 0.87% to 14.16%, and the light that suffers from TIR is 42.07%.

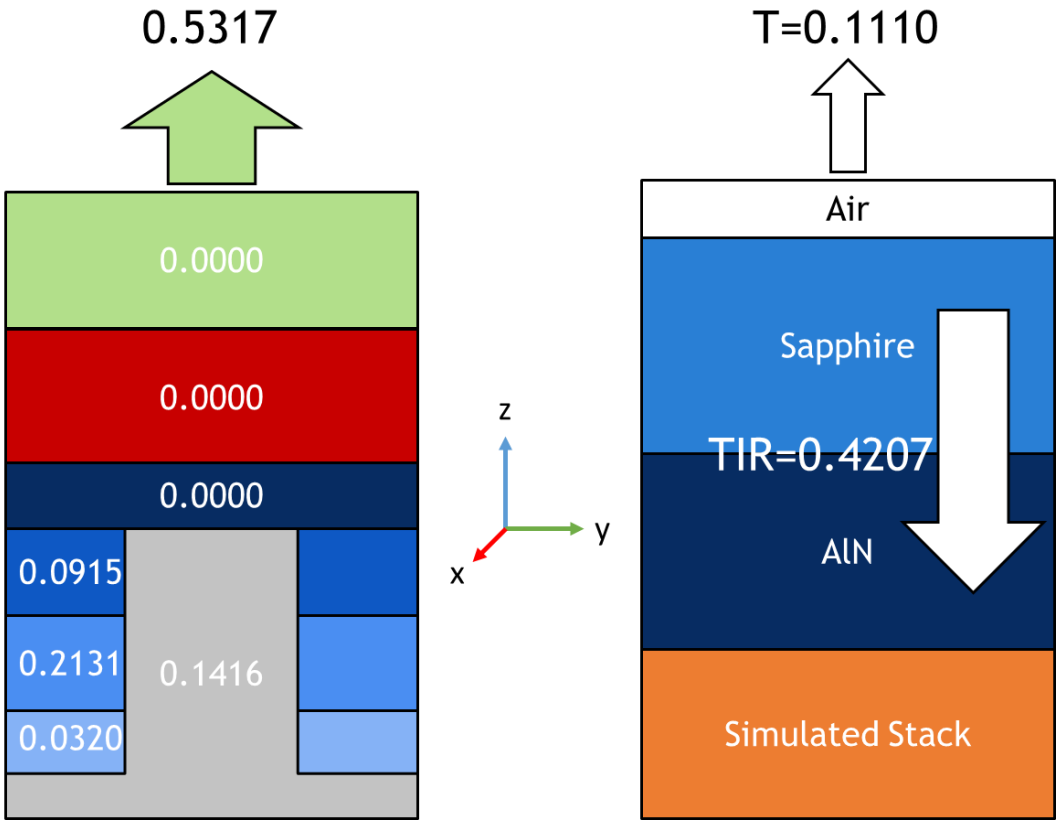

Figure 4-18 Nanostructured device analysis. Left: Absorption on each layer and amount of light launched to the substrate. Right: Part of the light will be projected to the outside, but most will suffer TIR.

Thus, even reducing the light absorption at the p-contact, the TIR phenomena is still a big drawback, that can only be changed if the angle of incident light between interfaces is changed. To analyze this, a Fourier decomposition of the electromagnetic field was done to see the diffraction orders generated by the nanostructure [62].

In plain words, the Fourier Transformation divides the whole electric field into individual plain waves, each one with its own direction, and its own *k* vector, making the subsequent analysis much affordable. Each one of these plain waves is called a mode and is unique and self-defined with its own *k* vector.

The *k* vector is a representation of the plain wave in the reciprocal space and gives information about the wavelength and the direction of the plain wave. The following set of equations define what the *k* vector is:

$$k = \frac{2\pi}{\lambda} \tag{64}$$

Here, k is the wavenumber (in m^{-1}) and λ is the wavelength (in m). This wavenumber will be the modulus of the *k* vector:

$$\left|\vec{k}\right| = k = \sqrt{k_{\parallel}^2 + k_{\perp}^2} \tag{65}$$

being k the wavenumber (in m^{-1}), $k_{\parallel}$ the component parallel to the interface between layers and $k_{\perp}$ the component perpendicular to the interface. In this case, the perpendicular component will be the same as the z-component (k_z), while the parallel component will be a combination of both x and y components (k_x and k_y), see Figure 4-18 for the reference axis. Working in the reciprocal space with the *k* vectors will allow a much easier visualization of all the modes and the spatial distribution, very useful to find out how the TIR phenomena is affecting this device.

As an example of this process, Figure 4-19 shows the normalized power of the output modes that a dipole in the active layer generates and are projected to the substrate (with the setup defined at Figure 4-18). Each point in this figure represents a mode, with its k_x and k_y values and the normalized power that is deposited in it. With these values, the parallel component can be calculated using Equation 66.

$$k_{\parallel} = \sqrt{k_x^2 + k_y^2} \tag{66}$$

Knowing the parallel component and the wavelength (265nm), the output angle can be computed, being 0° the normal emission (when $k_{\parallel} = 0$).

$$\theta = \operatorname{asin}\left(\frac{k_{\parallel}}{|\vec{k}|}\right) \tag{67}$$

From Snell's law, the critical angle can be computed as:

$$\theta_c = \operatorname{asin}\left(\frac{n_o}{n_i}\right) \tag{68}$$

being n_i and n_o the refractive indices of the input and output media. In the case of study, this critical angle equals to 25°. This means that any plane wave with and output angle higher than this value will suffer TIR. In other words, we can compute the $k_{\parallel}$ value that represents 25° using Equation 67 and plot it in the reciprocal space. This is represented as the inner red ring in Figure 4-19, and means that any mode that lays in the outside of this ring will be reflected totally.

The outer red ring represents the case of $k_{\parallel} = |\vec{k}|$, i.e., the output angle is 90°. If a mode is placed out of this ring, that would mean that $k_{\parallel} > |\vec{k}|$, and that is only possible if $k_{\perp}$ is imaginary (check Equation 65). These modes are called "evanescent modes" and cannot transmit power. That is why they do not appear in the following normalized power graphs.

Now, with all the bases explained, the Figure 4-19 can be easily understood. The graph plots the normalized power of each mode, so if we simply add the power of each one of the modes, we will obtain a value of 0.5317. This value equals the amount of light projected into the substrate (see Figure 4-18, left). However, as it was previously explained, all the modes that are not inside the inner ring will suffer TIR. So, if we add only the modes that are placed inside the inner ring, we obtain 0.1110. Indeed, this is

the amount of light that is successfully extracted from the device, i.e., the Light Extraction Efficiency (LEE).

Of course, if we add the remaining modes (the ones between the two rings, suffering TIR), we will obtain 0.4207, which is the exact same value that we obtained at Figure 4-18, right.

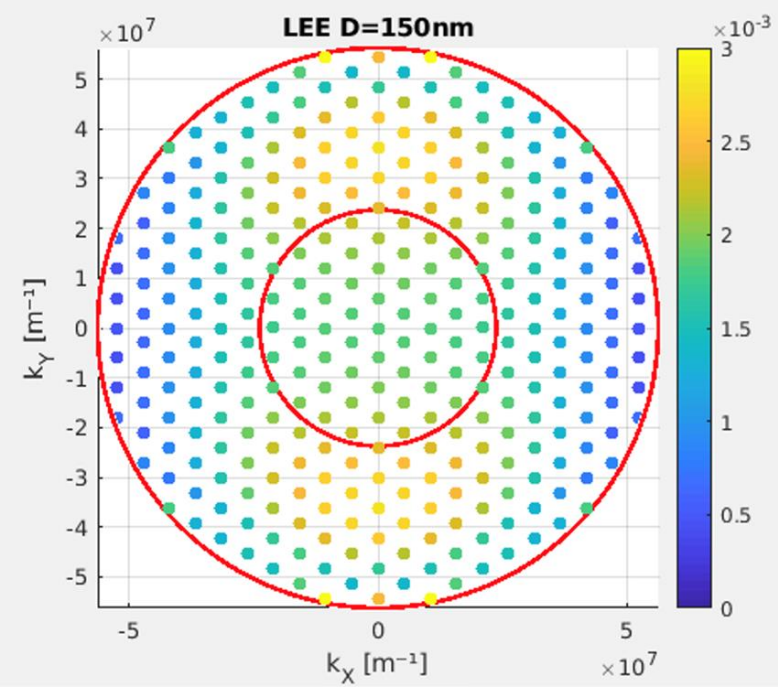

Figure 4-19 Normalized power of light modes going through the substrate. The modes inside the inner red ring will go out of the device. The modes laying between both red rings will suffer TIR. The modes out of the ring cannot carry power and are known as "evanescent" modes.

This type of analysis is very interesting to check how the nanostructure distributes the power and it can be used to select between several nanostructure shapes or geometrical parameters. For example, a preliminary study of the effect of the diameter size of the structure is shown in Figure 4-20 where the diameter is changed from 150nm to 250nm.

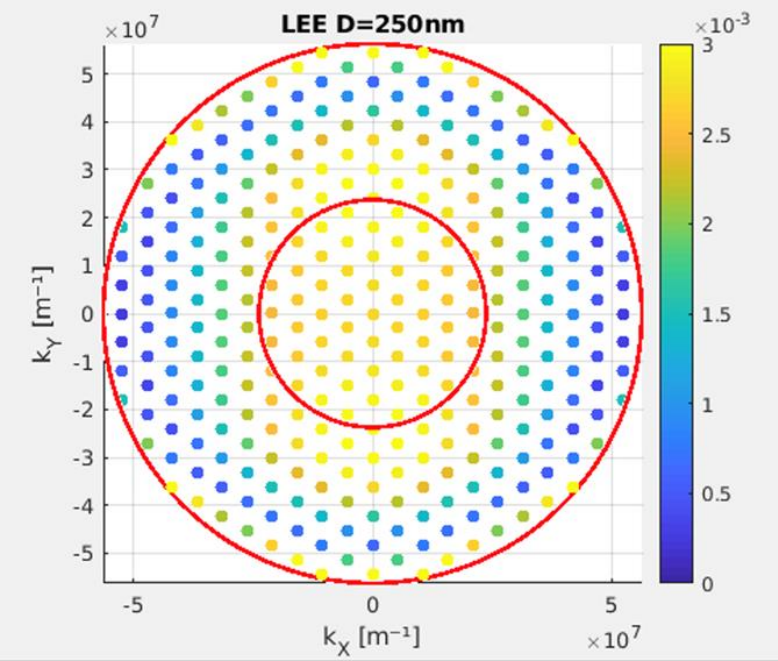

Figure 4-20 Light modes distribution with a nanostructure diameter of 250 nm.

It can be seen that more light is focused inside the inner red ring (which represents the escape cone). In fact, this focusing leads to an improvement, giving a light extraction efficiency of around 15% (three times higher than the planar reference).

So, even though this is not the fully optimized structure, the light extraction efficiency is multiplied by three. Starting from this proof of concept I intend to develop a full analysis of this structure to check if the total internal reflection phenomena could be further suppressed, changing the geometrical parameters of the structure. Also, I have traced further computations that consider multiple reflections, trying to extract as much light as possible of the device.

In summary, during this chapter the nanostructures have been applied to thin film, hydrogenated amorphous silicon solar cells, crystalline silicon / perovskite tandem solar cell and even a light emitting diode. These studies implied a 40.8% and a 20.5% increase in the photocurrent generation (respectively on a-Si:H and c-Si/PVSK tandem) and a generation of three journal publications. Preliminary results of the nanostructure inclusion on a DUV-LED have multiplied by three the light extraction efficiency and will be also submitted to journal publication.

4.6. Bibliography

[1] A. Flat and A. G. Milnes, “Optimization of multi-layer front-contact grid patterns for solar cells,” *Solar Energy*, vol. 23, no. 4, pp. 289–299, Jan. 1979, doi: 10.1016/0038-092X(79)90122-1.

[2] Q. Xu, L. Meng, and X. Wang, “Reducing shadowing losses in silicon solar cells using cellulose nanocrystal: polymer hybrid diffusers,” *Appl. Opt., AO*, vol. 58, no. 10, pp. 2505–2511, Apr. 2019, doi: 10.1364/AO.58.002505.

[3] R. Saive *et al.*, “Effectively Transparent Front Contacts for Optoelectronic Devices,” *Advanced Optical Materials*, vol. 4, no. 10, pp. 1470–1474, 2016, doi: https://doi.org/10.1002/adom.201600252.

[4] R. Saive *et al.*, “Silicon heterojunction solar cells with effectively transparent front contacts,” *Sustainable Energy Fuels*, vol. 1, no. 3, pp. 593–598, May 2017, doi: 10.1039/C7SE00096K.
[5] S. Calnan *et al.*, “Detailed comparison of transparent front contacts for thin film silicon solar cells,” in *2011 37th IEEE Photovoltaic Specialists Conference*, Jun. 2011, pp. 000579–000584, doi: 10.1109/PVSC.2011.6186021.
[6] “Optics, 5th Edition.” /content/one-dot-com/one-dot-com/us/en/higher-education/program.html (accessed Feb. 01, 2021).
[7] “Optical Properties of Silicon | PVEducation.” https://www.pveducation.org/pvcdrom/materials/optical-properties-of-silicon (accessed Mar. 05, 2021).
[8] D. Bouhafs, A. Moussi, A. Chikouche, and J. M. Ruiz, “Design and simulation of antireflection coating systems for optoelectronic devices: Application to silicon solar cells,” *Solar Energy Materials and Solar Cells*, vol. 52, no. 1, pp. 79–93, Mar. 1998, doi: 10.1016/S0927-0248(97)00273-0.
[9] A. Uzum *et al.*, “Sprayed and Spin-Coated Multilayer Antireflection Coating Films for Nonvacuum Processed Crystalline Silicon Solar Cells,” *International Journal of Photoenergy*, vol. 2017, p. e3436271, Jan. 2017, doi: 10.1155/2017/3436271.
[10] U. Gangopadhyay, S. Jana, S. Das, P. Ghosh, and A. Mondal, “Anti-reflective nanocomposite based coating for crystalline silicon solar cells with noticeable significance,” *Journal of Renewable and Sustainable Energy*, vol. 5, no. 3, p. 031607, Jun. 2013, doi: 10.1063/1.4808154.
[11] J. Kim, D. Inns, K. Fogel, and D. K. Sadana, “Surface texturing of single-crystalline silicon solar cells using low density SiO2 films as an anisotropic etch mask,” *Solar Energy Materials and Solar Cells*, vol. 94, no. 12, pp. 2091–2093, Dec. 2010, doi: 10.1016/j.solmat.2010.06.026.
[12] D. H. Macdonald *et al.*, “Texturing industrial multicrystalline silicon solar cells,” *Solar Energy*, vol. 76, no. 1, pp. 277–283, Jan. 2004, doi: 10.1016/j.solener.2003.08.019.
[13] R. Santbergen, J. Blanker, A. Dhathathreyan, H. Tan, A. H. M. Smets, and M. Zeman, “Towards Lambertian internal light scattering in solar cells using coupled plasmonic and dielectric nanoparticles as back reflector,” in *2013 IEEE 39th Photovoltaic Specialists Conference (PVSC)*, Jun. 2013, pp. 0029–0033, doi: 10.1109/PVSC.2013.6744092.
[14] H. Cui, P. R. Campbell, and M. A. Green, “Optimisation of the Back Surface Reflector for Textured Polycrystalline Si Thin Film Solar Cells,” *Energy Procedia*, vol. 33, pp. 118–128, Jan. 2013, doi: 10.1016/j.egypro.2013.05.048.
[15] M. A. Green, “Lambertian light trapping in textured solar cells and light-emitting diodes: analytical solutions,” *Progress in Photovoltaics: Research and Applications*, vol. 10, no. 4, pp. 235–241, 2002, doi: https://doi.org/10.1002/pip.404.
[16] “Past Conferences and Proceedings.” https://metaconferences.org/ocs/index.php/META19/index/pages/view/proceedings#.YIlA-LUzaUm (accessed Apr. 28, 2021).
[17] R. Könenkamp, S. Muramatsu, H. Itoh, S. Matsubara, and T. Shimada, “Mobility-Lifetime Product in Hydrogenated Amorphous Silicon,” *Jpn. J. Appl. Phys.*, vol. 29, no. 12A, p. L2155, Dec. 1990, doi: 10.1143/JJAP.29.L2155.

[18] H. A. Atwater and A. Polman, “Plasmonics for improved photovoltaic devices,” *Nature Materials*, vol. 9, no. 3, Art. no. 3, Mar. 2010, doi: 10.1038/nmat2629.

[19] P. Spinelli, M. A. Verschuuren, and A. Polman, “Broadband omnidirectional antireflection coating based on subwavelength surface Mie resonators,” *Nature Communications*, vol. 3, no. 1, Art. no. 1, Feb. 2012, doi: 10.1038/ncomms1691.

[20] J. F. Algorri, B. García-Cámara, A. Cuadrado, J. M. Sánchez-Pena, and R. Vergaz, “Selective Dielectric Metasurfaces Based on Directional Conditions of Silicon Nanopillars,” *Nanomaterials*, vol. 7, no. 7, Art. no. 7, Jul. 2017, doi: 10.3390/nano7070177.

[21] A. I. Barreda, Y. Gutiérrez, R. Alcaraz de la Osa, F. Moreno, and F. González, “Optimizing shape characteristics of high refractive index particles to improve forward scattering,” *Journal of Quantitative Spectroscopy and Radiative Transfer*, vol. 236, p. 106573, Oct. 2019, doi: 10.1016/j.jqsrt.2019.106573.

[22] R. Li, B. Q. Li, and W. Wang, “Forward scattering nanoparticles based nanostructure for light trapping over solar spectrum,” *AIP Advances*, vol. 9, no. 8, p. 085119, Aug. 2019, doi: 10.1063/1.5116364.

[23] J. Grandidier, D. M. Callahan, J. N. Munday, and H. A. Atwater, “Gallium Arsenide Solar Cell Absorption Enhancement Using Whispering Gallery Modes of Dielectric Nanospheres,” *IEEE Journal of Photovoltaics*, vol. 2, no. 2, pp. 123–128, Apr. 2012, doi: 10.1109/JPHOTOV.2011.2180512.

[24] B. Wang, T. Gao, and P. W Leu, “Broadband light absorption enhancement in ultrathin film crystalline silicon solar cells with high index of refraction nanosphere arrays,” *Nano Energy*, vol. 19, pp. 471–475, Jan. 2016, doi: 10.1016/j.nanoen.2015.10.039.

[25] V. Khoshdel, M. Joodaki, and M. Shokooh-Saremi, “UV and IR cut-off filters based on plasmonic crossed-shaped nano-antennas for solar cell applications,” *Optics Communications*, vol. 433, pp. 275–282, Feb. 2019, doi: 10.1016/j.optcom.2018.10.005.

[26] J. Cao *et al.*, “Perfect light absorption of monolayer MoS2 with cross-shaped groove air resonator,” *Mater. Res. Express*, vol. 6, no. 1, p. 015050, Oct. 2018, doi: 10.1088/2053-1591/aae99f.

[27] A. Vaskin, R. Kolkowski, A. F. Koenderink, and I. Staude, “Light-emitting metasurfaces,” *Nanophotonics*, vol. 8, no. 7, pp. 1151–1198, Jul. 2019, doi: 10.1515/nanoph-2019-0110.

[28] M. H. Elshorbagy, E. López-Fraguas, J. M. Sánchez-Pena, B. García-Cámara, and R. Vergaz, “Boosting ultrathin aSi-H solar cells absorption through a nanoparticle cross-packed metasurface,” *Solar Energy*, vol. 202, pp. 10–16, May 2020, doi: 10.1016/j.solener.2020.03.075.

[29] S. H. Lee and N. Y. Ha, “Nanostructured indium-tin-oxide films fabricated by all-solution processing for functional transparent electrodes,” *Opt. Express, OE*, vol. 19, no. 22, pp. 21803–21808, Oct. 2011, doi: 10.1364/OE.19.021803.

[30] S. Jang *et al.*, “Facile fabrication of three-dimensional TiO2 structures for highly efficient perovskite solar cells,” *Nano Energy*, vol. 22, pp. 499–506, Apr. 2016, doi: 10.1016/j.nanoen.2016.02.050.

[31] K. Ha *et al.*, “A light-trapping strategy for nanocrystalline silicon thin-film solar cells using three-dimensionally assembled nanoparticle structures,”

Nanotechnology, vol. 27, no. 5, p. 055403, Jan. 2016, doi: 10.1088/0957-4484/27/5/055403.

[32] D. Xia and S. R. J. Brueck, "Lithographically directed deposition of silica nanoparticles using spin coating," *Journal of Vacuum Science & Technology B: Microelectronics and Nanometer Structures Processing, Measurement, and Phenomena*, vol. 22, no. 6, pp. 3415–3420, Nov. 2004, doi: 10.1116/1.1821582.

[33] J. G. Son, W. K. Bae, H. Kang, P. F. Nealey, and K. Char, "Placement Control of Nanomaterial Arrays on the Surface-Reconstructed Block Copolymer Thin Films," *ACS Nano*, vol. 3, no. 12, pp. 3927–3934, Dec. 2009, doi: 10.1021/nn900914q.

[34] A. Peter Amalathas and M. M. Alkaisi, "Nanostructures for Light Trapping in Thin Film Solar Cells," *Micromachines*, vol. 10, no. 9, Art. no. 9, Sep. 2019, doi: 10.3390/mi10090619.

[35] S. Morawiec, M. J. Mendes, F. Priolo, and I. Crupi, "Plasmonic nanostructures for light trapping in thin-film solar cells," *Materials Science in Semiconductor Processing*, vol. 92, pp. 10–18, Mar. 2019, doi: 10.1016/j.mssp.2018.04.035.

[36] F. Gaspari and S. Quaranta, "2.5 PV Materials," in *Comprehensive Energy Systems*, I. Dincer, Ed. Oxford: Elsevier, 2018, pp. 117–149.

[37] J. Boroumand, S. Das, A. Vázquez-Guardado, D. Franklin, and D. Chanda, "Unified Electromagnetic-Electronic Design of Light Trapping Silicon Solar Cells," *Scientific Reports*, vol. 6, no. 1, Art. no. 1, Aug. 2016, doi: 10.1038/srep31013.

[38] A. Vora, J. Gwamuri, J. M. Pearce, P. L. Bergstrom, and D. Ö. Güney, "Multi-resonant silver nano-disk patterned thin film hydrogenated amorphous silicon solar cells for Staebler-Wronski effect compensation," *Journal of Applied Physics*, vol. 116, no. 9, p. 093103, Sep. 2014, doi: 10.1063/1.4895099.

[39] W. Shockley and H. J. Queisser, "Detailed Balance Limit of Efficiency of p-n Junction Solar Cells," *Journal of Applied Physics*, vol. 32, no. 3, pp. 510–519, Mar. 1961, doi: 10.1063/1.1736034.

[40] A. D. Vos, "Detailed balance limit of the efficiency of tandem solar cells," *J. Phys. D: Appl. Phys.*, vol. 13, no. 5, pp. 839–846, May 1980, doi: 10.1088/0022-3727/13/5/018.

[41] G. E. Eperon, M. T. Hörantner, and H. J. Snaith, "Metal halide perovskite tandem and multiple-junction photovoltaics," *Nature Reviews Chemistry*, vol. 1, no. 12, Art. no. 12, Nov. 2017, doi: 10.1038/s41570-017-0095.

[42] S. Albrecht *et al.*, "Monolithic perovskite/silicon-heterojunction tandem solar cells processed at low temperature," *Energy Environ. Sci.*, vol. 9, no. 1, pp. 81–88, Jan. 2016, doi: 10.1039/C5EE02965A.

[43] "Best Research-Cell Efficiency Chart." https://www.nrel.gov/pv/cell-efficiency.html (accessed Dec. 22, 2020).

[44] M. H. Elshorbagy, B. García-Cámara, E. López-Fraguas, and R. Vergaz, "Efficient Light Management in a Monolithic Tandem Perovskite/Silicon Solar Cell by Using a Hybrid Metasurface," *Nanomaterials*, vol. 9, no. 5, Art. no. 5, May 2019, doi: 10.3390/nano9050791.

[45] D. T. Grant, K. R. Catchpole, K. J. Weber, and T. P. White, "Design guidelines for perovskite/silicon 2-terminal tandem solar cells: an optical study," *Opt. Express, OE*, vol. 24, no. 22, pp. A1454–A1470, Oct. 2016, doi: 10.1364/OE.24.0A1454.

[46] M. H. Elshorbagy, E. López-Fraguas, F. A. Chaudhry, J. M. Sánchez-Pena, R. Vergaz, and B. García-Cámara, "A monolithic nanostructured-perovskite/silicon

tandem solar cell: feasibility of light management through geometry and materials selection," *Scientific Reports*, vol. 10, no. 1, Art. no. 1, Feb. 2020, doi: 10.1038/s41598-020-58978-5.

[47] L. A. Jones, R. W. Worobo, and C. D. Smart, "UV Light Inactivation of Human and Plant Pathogens in Unfiltered Surface Irrigation Water," *Appl. Environ. Microbiol.*, vol. 80, no. 3, pp. 849–854, Feb. 2014, doi: 10.1128/AEM.02964-13.

[48] R. Yin *et al.*, "Light based anti-infectives: ultraviolet C irradiation, photodynamic therapy, blue light, and beyond," *Current Opinion in Pharmacology*, vol. 13, no. 5, pp. 731–762, Oct. 2013, doi: 10.1016/j.coph.2013.08.009.

[49] J. Holländer, R. Hakala, J. Suominen, N. Moritz, J. Yliruusi, and N. Sandler, "3D printed UV light cured polydimethylsiloxane devices for drug delivery," *International Journal of Pharmaceutics*, vol. 544, no. 2, pp. 433–442, Jun. 2018, doi: 10.1016/j.ijpharm.2017.11.016.

[50] C. Noè, M. Hakkarainen, and M. Sangermano, "Cationic UV-Curing of Epoxidized Biobased Resins," *Polymers*, vol. 13, no. 1, Art. no. 1, Jan. 2021, doi: 10.3390/polym13010089.

[51] X. Chen, M. Yang, Y. Cheng, G. J. Liu, and M. Zhang, "Narrow-band ultraviolet B phototherapy versus broad-band ultraviolet B or psoralen-ultraviolet A photochemotherapy for psoriasis," *Cochrane Database of Systematic Reviews*, no. 10, 2013, doi: 10.1002/14651858.CD009481.pub2.

[52] N. Riesen *et al.*, "Towards rewritable multilevel optical data storage in single nanocrystals," *Opt. Express, OE*, vol. 26, no. 9, pp. 12266–12276, Apr. 2018, doi: 10.1364/OE.26.012266.

[53] A. Fujioka *et al.*, "High-output-power 255/280/310 nm deep ultraviolet light-emitting diodes and their lifetime characteristics," *Semicond. Sci. Technol.*, vol. 29, no. 8, p. 084005, Jun. 2014, doi: 10.1088/0268-1242/29/8/084005.

[54] A. Fujioka *et al.*, "Progress of high-power deep-ultraviolet LEDs," in *Gallium Nitride Materials and Devices X*, Mar. 2015, vol. 9363, p. 93631L, doi: 10.1117/12.2078620.

[55] M. Guttmann, "Einfluss der Lichtextraktion auf die Effizienz AlGaN-basierter Leuchtdioden im tiefen ultravioletten Spektralbereich," 2020, doi: 10.14279/depositonce-10590.

[56] C. F. Madigan, M.-H. Lu, and J. C. Sturm, "Improvement of output coupling efficiency of organic light-emitting diodes by backside substrate modification," *Appl. Phys. Lett.*, vol. 76, no. 13, pp. 1650–1652, Mar. 2000, doi: 10.1063/1.126124.

[57] T. Fujii, Y. Gao, R. Sharma, E. L. Hu, S. P. DenBaars, and S. Nakamura, "Increase in the extraction efficiency of GaN-based light-emitting diodes via surface roughening," *Appl. Phys. Lett.*, vol. 84, no. 6, pp. 855–857, Feb. 2004, doi: 10.1063/1.1645992.

[58] M. Jo, N. Maeda, and H. Hirayama, "Enhanced light extraction in 260 nm light-emitting diode with a highly transparent p-AlGaN layer," *Appl. Phys. Express*, vol. 9, no. 1, p. 012102, Dec. 2015, doi: 10.7567/APEX.9.012102.

[59] M. Shatalov *et al.*, "High power AlGaN ultraviolet light emitters," *Semicond. Sci. Technol.*, vol. 29, no. 8, p. 084007, Jun. 2014, doi: 10.1088/0268-1242/29/8/084007.

[60] P. Manley *et al.*, "Nanopatterned sapphire substrates in deep-UV LEDs: is there an optical benefit?," *Opt. Express, OE*, vol. 28, no. 3, pp. 3619–3635, Feb. 2020, doi: 10.1364/OE.379438.

[61] M. G. R. Martens, “Optical gain and modal loss in AlGaN based deep UV lasers,” 2018, doi: 10.14279/depositonce-7512.
[62] “FourierTransform — ParameterReference.” https://jcmwave.com/docs/ParameterReference/bb20ed1f5c57805fb797f991a544818e.html?version=4.2.0 (accessed Apr. 29, 2021).

Chapter 5:Conclusions and future works

"There's a million things I haven't done, but just you wait" – Hamilton.

All along this last chapter I will expose the conclusions and final results of every section of this work. It has been a travel of years but there are still things to do. There are pending challenges and unsolved questions that will surely be addressed by the scientific community involved in photovoltaic issues. I will try to explain them at the end of each section.

5.1. Last generation solar cells fabrication.

Starting from almost no-knowledge related to the fabrication, I went through a full learning process of fabrication procedures to achieve the right solar cells samples. During my three-month research stay at Jaume I University of Castellón I learned how the perovskite solar cells are fabricated step by step. Using the standard architecture, I made MAPI solar cells of my own with a PCE of 16.9% (it is worth mentioning that the record from the lab at that time was around 19%).

Furthermore, I had the opportunity to work with a novel material, the Cesium Tin Iodide, trying to reduce the toxicity and environmental impact of the classical lead-based MAPI solar cells. This allowed me to explore the co-evaporation technique, synthesizing the perovskite using a "dry" method, building the layer in one process without the need of post-annealing to form the crystal.

Also, I worked on optical characterizations and high-detail tests, such as the scanning electron microscopy. With this characterization I have demonstrated that, optically speaking, the Cs_2SnI_6 could be a great material for certain devices, due to its absorption, equally distributed across the visible wavelengths. This material could be applied to solar windows or semi-transparent applications, due to its average visible transmittance value of 42.1% and with a thickness enough to avoid the problems related with the internal short-circuits of the device. However, it is needed to overcome the electrical drawbacks of this material. My work at UJI led to a paper publication and a congress communication with these results.

Perovskite and organic solar cells were also included in a visible light communication system as a proof of concept of their performance beyond their usual application, analyzing their respective behavior against light and transmission frequency. These studies demonstrate that both devices can be used in a visible light communication system as an audio link. Both studies led to two papers at MDPI Sensors and Organic Electronics.

As a future work, the research in lead-free perovskites should continue, taking my study of Cs_2SnI_6 developed at UJI as a starting point. It has been shown that it has potential to be a substitute of their lead counterparts, but the electrical properties should be studied deeper and eventually improved.

The techniques that I have learned during my stay can also be used to make other type of solar cells and to explore different types of substrates too. So, this knowledge will pave the way for me or for other researchers in the group to study and build solar cells, electrochromic devices or flexible devices integrated in cloths, to give just a few examples.

5.2. Solar cell characterization: SUNBOX

One of the main goals achieved during this PhD thesis has been the design, development, fabrication, and distribution of a solar simulator like no other in the market, SUNBOX. It is lightweight (less than 1kg), with a 3D printed PLA chassis, portable, small and with the best quality (AAA Class) according to the standard without having any kind of optics. This device has been my partner during all this work, evolving from a primigenial idea in my Master's thesis to its actual state. A device that has risen the attention of the industry not only in the solar cell sector, but also in the textile, biology, and healthcare sectors as well as in the scientific community.

Nowadays, SUNBOX is a AAA-Class simulator, according to the International Standard IEC 60904-9, so it can be used to test devices under standard testing conditions, but also special tests can be carried out. Some of the special tests that could be run are:

- Spectral responsivity test: In which any combination of its 14 wavelengths can be used to create custom spectra and check the behavior of the device under test under different illumination conditions.
- Sun scaling: SUNBOX has the ability of scaling the power of the sun, maintaining the spectral distribution. This means that several measurements using fractions of suns can be taken. This can help to analyze the behavior of the open circuit voltage of a solar cell, for example.
- UV analysis: Even though in the standard IEC 60904-9 the UV range is not mentioned, (actually, anything below 400nm is not considered), SUNBOX also matches the sun spectrum with A quality in the 300-400nm range. This spectral content is of high interest, specially working with devices that can suffer from degradation at these wavelengths. Moreover, high UV power can be projected using SUNBOX, to achieve extreme conditions of UV radiation (e.g., extraterrestrial applications).

All the research related with SUNBOX has been very successful, generating one publication at IEEE Transactions on Instrumentation and Measurement, three congress communications, a software registry and utility model (to protect the intellectual property of both software and hardware), as well as two contracts with a company linked to research centers to acquire SUNBOX for their own research.

As future works, SUNBOX possibilities are endless. I would like to further explore the functionalities that it can offer, such as pulsed light studies with adjustable commutation frequency, including a temperature control and make it an all-in-one device, adding also an I-V tracer in the system or even a simple Impedance analyzer, all of them following the low-cost premise. Also, the market is still open to include this system in biological systems, such as for analyzing the plants growth in different

conditions or even using this modular and portable technology for some phototherapy device or at small greenhouses.

5.3. Improving efficiency of nanodevices: nanostructures

As a conclusion for this section, it can be said that, after a long period of learning, I have achieved high skills in the use of several programs, starting from MATLAB modelling, going through Finite Element Method modelling using two programs: first COMSOL, and finally JCMSuite during my research stay at Helmholtz Zentrum Berlin.

After the learning and training process of these softwares and taking into account the state of the art regarding the fabrication of nanostructures, we proposed, modelled and computed several nanostructured designs for different solar cells and materials, going from hydrogenated amorphous silicon technology to a perovskite/crystalline-silicon tandem device.

On the one hand, in the hydrogenated amorphous silicon solar cell a nanostructure consisting of nanospheres-filled crosses was proposed. With this kind of nanostructure, our main goal was to increase the light projected to the active layer without altering the silicon in any manner. Thus, the proposed nanostructure can be done etching the electrode forming a periodic array of crosses or even stamping this array in the layer by several possible nanoimprinting methods. Then these crosses would be filled with nanospheres. Thinking about industrial production, maybe the etching is not so easily scalable as it can be the stamping (like in roll-to-roll or roll-to-plane techniques). Then the spheres filling could be done maybe using some approaches such as the blade coating (doctor blade). With this structure arrangement we have demonstrated that the short-circuit current density produced by the solar cell is increased by a 40% factor, assuming isolated photonic effects. Furthermore, this improvement allows a device with a thinner active layer, thus making an enhancement also in the carrier extraction, and therefore, in the electrical behavior of the solar cell. This work has generated a publication in Solar Energy Journal.

The natural continuation for this work is the creation of the device as a prototype, its characterization, and checking if the predicted improvements are achieved. Of course, other improvement goal could be making the nanostructure over a foil, in a kind of tape that could be glued over any kind of solar cell to improve its efficiency, without the need of including extra-steps in the fabrication process of the cell itself.

On the other hand, related to the perovskite/silicon tandem solar cell a new approach was considered. In this case the perovskite layer was nanostructured itself, in such a way that the short wavelengths are confined in this layer, but also longer wavelengths are efficiently projected into the crystalline silicon layer. The big drawback here is the complexity of the structure, that needs the inclusion of a dielectric spacer to split both electron and hole transport layers. However, this structure allows an enhancement of the photogenerated short-circuit current density (that must be matched between both subcells) of 20.5%. This study is complemented with an ulterior work that analyzes the material selection and optimization of the parameters of the nanostructure, to demonstrate the manufacturing feasibility of the proposed device.

Both studies have been published in MDPI Nanomaterials and Scientific Reports Journals.

Same as in the previous structure, the ideal continuation would be the construction of the device, which in this case is more difficult due to the nanostructuring of the whole perovskite layer. Notwithstanding it would be interesting to check the electrical behavior of the device to ensure that the electrical response is also improved by the use of the structure. So maybe a first approach can be to simulate the electrooptical behavior of the device, which is a much more difficult process that requires advanced computation.

Finally, during my research stay in Helmholtz Zentrum Berlin (Berlin, Germany) I developed a study in which I achieved an increase in light extraction efficiency of an DUV-LED, going from 4.57% to around 15%, using a cylinder-based nanostructure. These results demonstrate that the nanostructures can be applied to improve any kind of optical device and not only solar cells. A scientific publication is currently in preparation to publish the first preliminary results.